Austrian Journal of Technical and Natural Sciences

2023, No 9 – 10

PREMIER Publishing

Vienna
2023

Austrian Journal of Technical and Natural Sciences

Scientific journal

№ 9–10 2023

ISSN 2310-5607

Editorial office Premier Publishing s.r.o.
Praha 8 – Karlín, Lyčkovo nám. 508/7, PSČ 18600
E-mail: pub@ppublishing.org
Homepage: ppublishing.org

Austrian Journal of Technical and Natural Sciences is an international, English language, peer-reviewed journal. The journal is published in electronic form.

The decisive criterion for accepting a manuscript for publication is scientific quality. All research articles published in this journal have undergone a rigorous peer review. Based on initial screening by the editors, each paper is anonymized and reviewed by at least two anonymous referees. Recommending the articles for publishing, the reviewers confirm that in their opinion the submitted article contains important or new scientific results.

Premier Publishing is not responsible for the stylistic content of the article. The responsibility for the stylistic content lies on an author of an article.

Instructions for authors

Full instructions for manuscript preparation and submission can be found through the Premier Publishing home page at: http://ppublishing.org.

Material disclaimer

The opinions expressed in the conference proceedings do not necessarily reflect those of the Premier Publishing, the editor, the editorial board, or the organization to which the authors are affiliated.

Premier Publishing is not responsible for the stylistic content of the article. The responsibility for the stylistic content lies on an author of an article.

Included to the open access repositories:

SJIF 2023 = 5.859 (Scientific Journal Impact Factor Value for 2023).

Included to the Uzbekistan OAK journals bulletin.

Typeset in Berling by Ziegler Buchdruckerei, Linz, Austria.
Printed by Premier Publishing, Vienna, Austria on acid-free paper.Printed by Premier Publishing, Vienna, Austria on acid-free paper.

The Austrian Journal of Technical and Natural Sciences, No 9–10
ISSN 2310-5607

PREMIER Publishing
ppublishing.org

Section 1. Chemistry

DOI:10.29013/AJT-23-9.10-3-6

SYNTHESIS OF MODIFIED LUPININ DERIVATIVES

Tureniyazova Dametken Ayniyazovna [1],
Kushiev Khabibjon Khozhibabaevich [2]

[1] Karakalpak State University, Nukus, Uzbekistan
[2] Gulistan State University, Gulistan, Uzbekistan

Cite: *Tureniyazova D.A., Kushiev Kh.Kh., (2023). Synthesis of modified lupinin derivatives. Austrian Journal of Technical and Natural Sciences 2023, No 9–10. https://doi.org/10.29013/AJT-23-9.10-3-6*

Abstract

The article presents the results of research aimed at the synthesis and study of various modified benzoyl esters of the alkaloid lupinin in order to find among them effective biologically active substances that have a certain superiority over known drugs. The main objectives of the study were: to develop a synthesis method, to establish the structure and configuration of synthesized compounds.

Keywords: *alkaloid, synthesis, lupinin, structure, bond, spectrum*

Introduction

One of the priority areas of bioorganic chemistry is the modification of molecules of natural compounds, in particular alkaloids. In this regard, lupinin alkaloids by their chemical structure belong to the most interesting class of compounds, among which there are substances with various combinations, for example, carbonic and heterocycles, conformational and optical isomers. Modification of the alkaloid molecule opens up wide opportunities for the search for highly effective, selective, stereospecific biologically active substances (Sadykov, A.S., Aslanov, X.A., Kushmuradov, Yu.K., 1975).

Among such alkaloids, lupinin (7a-hydroxymethyl-trans-quinolizidine) occupies an important place and is contained in significant quantities and is extracted from the Central Asian plant Anabasis aphylla L., belonging to the Chenopodiaceae family (Nasirov, S.H., Hazbievich, I.S., 1982.

Among the known derivatives of lupinin, its esters, which have pronounced antiviral, antitumor and hepatoprotective activity, are the most studied (Sadykov, A.S., Aslanov, X.A., Kushmuradov, Yu.K., 1975; Nasirov, S.H., Hazbievich, I.S., 1982; Tlegenov, R.T., 1991). Series of lupinine esters showed local anesthetic effect, antituberculous and anticholinesterase activity

(Nasirov, S.H., Hazbievich, I.S., 1982; Tlegenov, R.T., 1991).

Results and their discussion

In order to find new highly effective biologically active compounds among lupinin derivatives, we synthesized new derivatives of lupinin – its aminoesters. Synthesis was carried out according to this scheme:

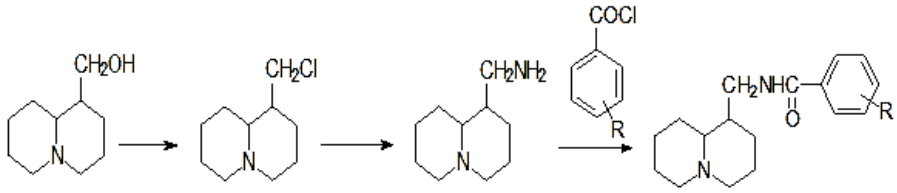

R = o-COC_6H_5; m-OCH_3; m-NO_2; p-NH_2; 2,4-Cl;

Of all the synthesized compounds, ortho-benzoyl-, 2,4-dichloro-p-amino substituted benzoylamidolupinins are crystalline substances with a yellowish tinge, and the rest are oily substances. The individuality of the synthesized compounds was controlled by thin-layer chromatography. Hydrochlorides were obtained by the action of dry hydrogen chloride. All hydrochlorides are obtained clean and do not require further cleaning. The characteristics of the synthesized compounds are given in Table 1.

The structure of the obtained substances is confirmed by the data of PMR, IR and mass spectra.

Table 1. *Physico-chemical characteristics of aminobenzoyl esters of aminolupinin (I) and their hydrochlorides (II)*

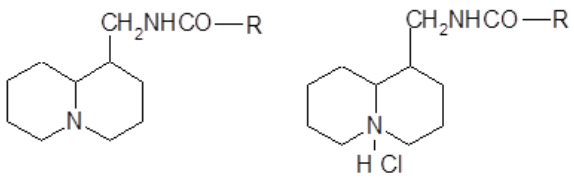

I II

№	R	Exit,%	Melting point, °C (I)	R_f	Melting point,°C (II)
1	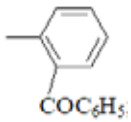	68.0	167–169	0.92	hygroscope
2	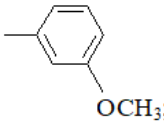	59.0	87–89	0.54	142–143
3	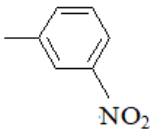	79.0	oil	0.68	hygroscope
4	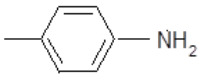	59.6	147–149	0.28	83–85
5	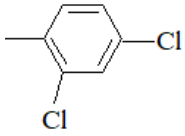	59.8	158–160	0.33	hygroscope

In the IR spectrum (1–5) there are intense absorption bands characteristic of functional groups (ϒ, cm^{-1}): 3350––3450 cm^{-1} (–NH-group); 1250–1190 cm^{-1} (– C - N -); 1590–1610 cm^{-1} (– C = C-aromatic core); 1610–1700 cm^{-1} (– N - C = 0) and 2800–2650 cm^{-1} (trans-quinolizidine system).

Figure 1. *IR spectrum of p-aminobenzoyl ether of aminolupinin*

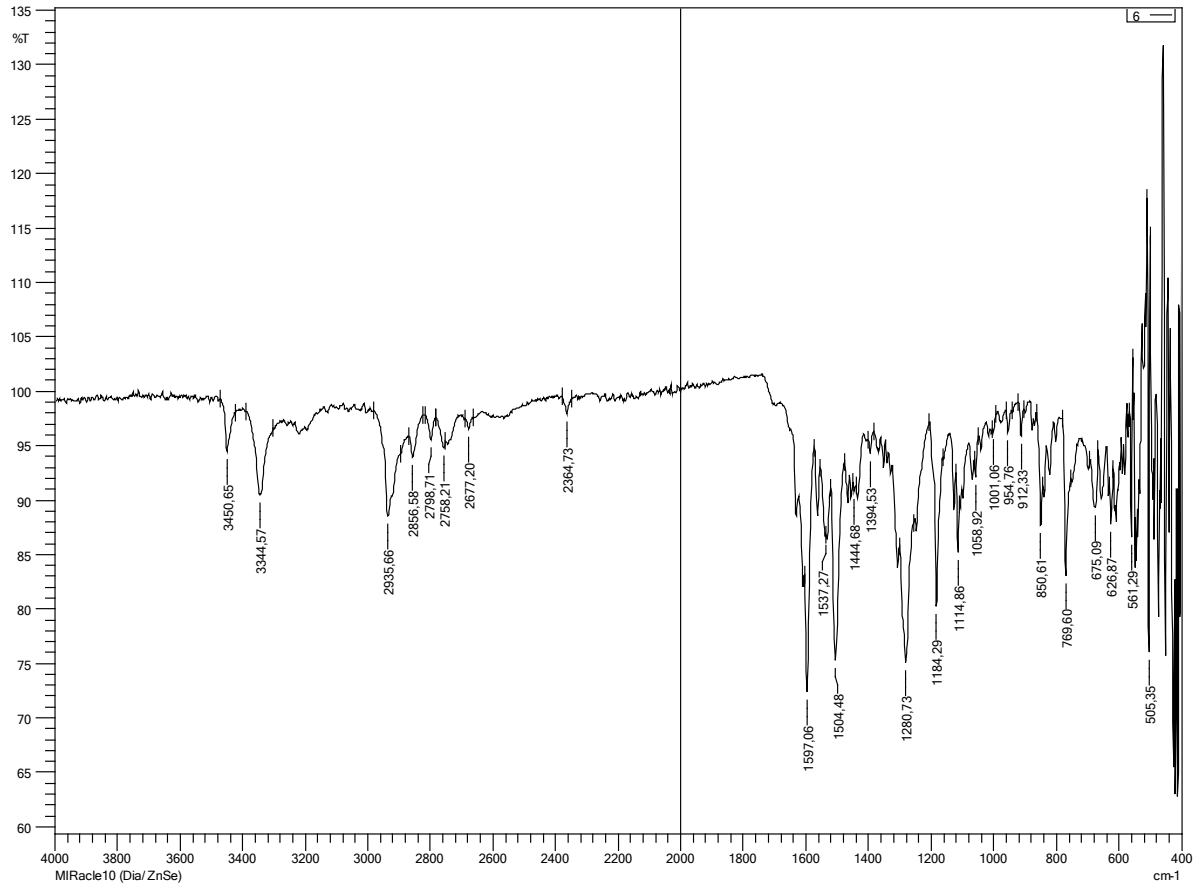

In the PMR spectra of aminobenzoyl esters of aminolupinin (1–5), there is a complex signal in the region of 3.7–3.9 p.p.m. (2H, m) of the CH_2-N fragment. Signals of aromatic protons are observed at 7.6––7.9 p.p.m. (4H, m). in the region of 1.1––2.2 p.p.m. (14H, m, CH_2), signals belonging to protons of the quinolizidine fragment are noted. The positions of the other signals depend on the specific type of substituent. All the obtained spectra confirm the structure of the synthesized derivatives of aminobenzoyl esters of aminolupinin.

In the mass spectra of these compounds there are peaks with m/e 167, 152, 136, 124, 98, and etc., characteristic of alkaloids with a trans-quinolizidine system.

Conclusions

Thus, some lupinin derivatives with substituted benzoic acids bound by an amide bond and their hydrochlorides were synthesized. Their physico-chemical constants are determined. Based on the study of the IR, PMR and mass spectra of the obtained compounds, their structure has been established.

Modified derivatives of the lupinin alkaloid may offer great prospects in the search for biologically active substances with high efficiency, selectivity and stereospecificity.

References

Sadykov, A. S., Aslanov, X. A., Kushmuradov, Yu. K. (1975). Alkaloidy hinolizidinovogo ryada. Himiya, stereohimiya, biogenez. M. Nauka.

Nasirov, S. H., Hazbievich, I. S. (1982). Farmakologiya alkaloidov Anabasis aphylla i klinicheskoe primenenie anabazina gidrohlorida. – Tashkent. FAN.
Tlegenov, R. T. (1991). Sintez i antiholinesteraznaya aktivnost' novyh proizvodnyh alkaloida lupinina. Avtoref. diss. kand. him. nauk. – Tashkent.
Tureniyazova, D. A. (2022). Spectral analysis of amide derivatives of the lupinine alkaloid. *IEJRD is an international interdisciplinary journal,*– Vol. 7. – No. 3. URL: https://doi.org/10.17605/OSF.IO/SD5V7
Tureniyazova D. A. [ect.]. (2023). Sintez i issledovanie lupininovogo efira yantarnoj kisloty. Universum: himiya i biologiya: elektron, nauchn. zhurn. – 6(108). URL: https://7universum.eom/ru/nature/archive/itern/l 5565
Tureniyazova, D. A., Nurieva, M. U. (2023). Investigation of the synthesis reaction of lupinin ether of succinic acid. *Scientific and practical conference Prospects for the development of science and education* – No. 10. URL: https://humoscience.com/index.php/pdce/issue/view/51
Tureniyazova, D. A. (2023). Razrabotka metodov sinteza aminolupinina. Universum: tekhnicheskie nauki: elektron. nauchn. zhurn. – 10(115). URL: https://7universum.com/ru/tech/archive/item/16075

submitted 22.08.2023;
accepted for publication 20.09.2023;
published 8.10.2023

Contact: damet.t@mail.ru; kushiev@mail.ru

The Austrian Journal of Technical and Natural Sciences, No 9–10
ISSN 2310-5607

PREMIER Publishing
ppublishing.org

DOI:10.29013/AJT-23-9.10-7-16

STUDY OF THE SYNTHESIS AND STRUCTURE OF POLYETHYLENE NAPHTHALENE CARBONIC ACID

F. Sh. Boboqulova [1], S.E. Nurmanov [2], O. Sh. Kodirov [2]

[1] Shakhrisabz branch of Tashkent chemical-technological institute

[2] National University of Uzbekistan

Cite: *Boboqulova F. Sh., Nurmanov S.E., Kodirov O. Sh. (2023). Study of the Synthesis and Structure of Polyethylene Naphthalene Carbonic Acid. Austrian Journal of Technical and Natural Sciences 2023, No 7-10. https://doi.org/10.29013/AJT-23-9.10-3-16*

Abstract

The article presents the research results of synthesizing weakly acidic polycondensation type catio-nites based on naphthalene homologs isolated from local raw materials and studying their structure using various physicochemical analysis methods. Pyrolysis oil, a secondary product of the pyrolysis process of JV "Uz-Kor Gas Chemical" LLC, was selected for the research, and naphthalene homologs were separated from its composition by fractionation and used as raw materials in further work. During the polycondensation of naphthalene carbonic acid with formalin, polymethylene naphthalene carbonic acid was obtained in the process of obtaining a weak cationic, and its composition was compared using SEM (scanning electron microscope), IR-spectrum, TG (thermogravimetry) and DTA (differential thermal analysis).

Keywords. *Naphthalene homologs, synthesis, SEM, IR, TG, DTA, naphthalene carbonic acid, formalin, catalyst, zinc chloride, polycondensation*

Introduction

Pyrolysis oil is a secondary product of pyrolysis, the composition of which depends on the raw material, and consists of a mixture of hydrocarbons with a boiling point above 180 °C. Currently, pyrolysis products do not have a specific field of use, but in most cases, they are used as a component of steam boiler fuel. Secondary products of pyrolysis reach 325.000 tons per year in Russia. The volume of production at the Naftan plant of Belarussian "Polymir" OJSC is 12.000–16.000 tons per year. As a result of the analysis of the results of chromatography of the composition of the liquid concentrate by Belarusian scientists, it was found that it contains more than 225 individual substances. They contain 67% by weight of aromatic hydrocarbons, particularly naphthalene, and their homologs up to 18% (Prech E., Byul'mann F., Affol'ter K., 2006; Turnbull L., Liggat J.J., Mac Donald W.A., 2013; Guoqiang Wang, Guitang Yang, Min. Jiang, Rui. Wang, Yin Liang, Guangyuan Zhou, 2021; Roupakias C.P., Bikiaris D.N., Karayannidis G.P., 2005; Jeong Y.G., Jo W.H., Lee S.C., 2002; Stier U., Schawaller D., Oppermann W., 2001; Lorenzetti C., Finelli L., Lotti N., Vannini M., Gazzano M., Berti C., Munari A., 2005.

Synthetic ion exchangers are produced in industry in two ways:

– polymerization or polycondensation of initial monomer compounds whose molecules have active groups;

– by introducing functional groups into macromolecules obtained from the copolymerization of vinyl aromatic compounds with dienes.

The first method is more practical because the production of ignites by chemical modification of polymers is associated with the following difficulties: multi-stage, labor intensive, the need to use toxic products, and partial decomposition of macromolecules (Bellami, L., 1971; Nakanisi, K., 1963; Chung, T.C., 2002; Hustad, P.D.; Coates, G.W., 2002; Charlesby, A., 1960; Chapiro, A., 1962; Coqueret, X., 2008.

Table 1. *Raw material composition and properties of some cations*

Brand	COE0.1 n. NaOH mg-eq/g	Comparison size ml/g	Active functional group	The main raw material
Carboxyl cations based on polymerization				
KM	7.4–7.6	–	‹COOH	Methacrylic acid, DVB
NMД	7.8–8.8	–	‹COOH	Methacrylic acid, DVB
KMT KMДA KMTБ	10.1 (0.4)	3.5	‹COOH	Methacrylic acid, acrylamide
KP	7.7	–	‹COOH	Methacrylic acid, DVB
KU-2–8	5.1	2.8	-SO_3H	Stirol, DVB
Sulcocations based on polycondensation				
KУ-1	4.2–4.7 (2.0–2.5)	2.7–3.0	‹OH	Phenolsulfoacid, formaldehyde
KУ-6	5.5 (3.4)	2.7	‹COOH	Anthracene, formaldehyde
CH	6.5 (3.9)	3.0	‹OH	Phenolformaldehyde resin, novalak
ССФ	3.9–4.0	3.7	‹OH	Sterol, formaldehyde
Polikondensatlash asosidagi fosfokationitlar				
РФ	5.0	–	‹PO_3H_2, ‹OH	Phenol, resorcinol, formaldehyde
ВФ	4.5	3.0–3.5	‹PO_4H_2	Polyvinyl alcohol
AP	3.0	1.5–1.6	‹AsO_3H_2, ‹OH	Oxyphenylcresol acid, formalin

Ionites contain active (ionogenic) groups (derived from the Greek word “geneticos,” meaning “to give birth”). Synthetic ion exchangers are divided into three main groups:

– Cation exchangers;

– Anion exchangers;

– Amphoteric ion exchangers (polyampholytes).

Cation exchangers are polymers that possess acidic properties and can absorb positively charged ions (cations) from electrolyte solutions.

Anion exchangers are polymers that exhibit the ability to absorb negatively charged ions (anions) from solutions and exchange them for other anions. They display basic properties.

Amphoteric ion exchangers are called polyampholytes, and they contain acidic and basic ionogenic groups. Depending on the conditions, both cation and anion exchangers can exhibit these properties.

The purpose of the work: synthesis of monomers (ethylene and propylene) for the polymer production process at “Uz-Kor Gas Chemical” LLC, a secondary product of pyrolysis device, deep processing of pyrolysis oil, separation of naphthalene homologs, the study of the synthesis process of polymeth-

ylenenaphthalene carboxylic acid mixture, based on them is to create technology for production of acidic cationic and special additives for concrete mixtures.

Table 2. *Active groups in ionites*

Cationite		Anionite	
Available ion	Counter ion	Available ion	Counter ion
SO_3^-	H^+	$-NH_3^+$	OH^-
COO^-	H^+	$=NH_2^+$	OH^-
PO_3^{-2}	H^+	$\equiv NH^+$	OH^-
SeO_3^-	H^+	$==N^+$	OH^-
AsO_3^{-2}	H^+		

Materials and methods

To extract naphthalene and its homologs from the composition of pyrolysis oil, the secondary product "pyrolysis oil" from the Ustyurt gas-chemical complex, which belongs to "Uz-Kor Gas Chemical" LLC, was used as a raw material.

Chromatomass-spectrum results showed that natalin and its homologs constitute the main part of pyrolysis oil. Among these products, naphthalene homologs make up 28.34% of the total.

Pyrolysis oil was divided into fractions using rectification drive, and their composition was studied (Table 1). 1-methylnaphthalene and 2-methylnaphthalenes account for up to 80% of the fraction between 220–250 °C, while 1,6-dimethylnaphthalene accounts for up to 48% of the fraction at 260–270 °C.

The sodium and calcium salts of polymethylenenaphthalene carboxylic acid (PMNK), which is the focus of the research, serve as highly effective diluents with a high molecular fraction content. However, the synthesized polycondensate contains free formaldehyde, which negatively affects the ecological characteristics of the finished product.

The technological process of producing polymethylenenaphthalene carboxylic acids (PMNK) consists of the following stages:

– Oxidation of 2-methylnaphthalene with concentrated nitric acid to obtain β-naphthalene carboxylic acid.

– Polycondensation of β-naphthalene carboxylic acid with formaldehyde to obtain polymethylenenaphthalene carboxylic acid.

– Neutralization of the resulting reaction product with sodium hydroxide or calcium hydroxide.

– Filtration of the additive solution to remove sodium/calcium deposits.

Depending on the conditions of the process, substances with different properties are formed. We analyze all stages of the technological process.

At the stage of oxidation of 2-methylnaphthalene with concentrated nitric acid, the production of β-naphthalene carboxylic acid is the main process.

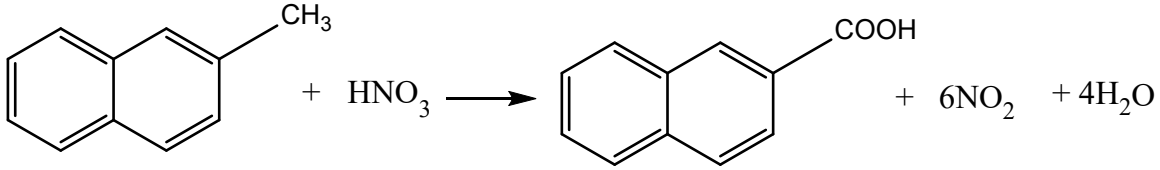

Depending on the temperature of the oxidation process, a mixture of different naphthalic acids is formed. Therefore, the oxidation process is carried out at a temperature higher than 120 °C. When the temperature rises above 150 °C, the level of side processes increases, resulting in an increased amount of various acids. Conversely, decreasing the temperature of the process below 120 °C leads to an increase in the amount of other oxygenated organic compounds that do not oxidize into 2-methylnaphthalene acid.

The polycondensation reaction of naphthalene carboxylic acids with formalin proceeds according to the following scheme:

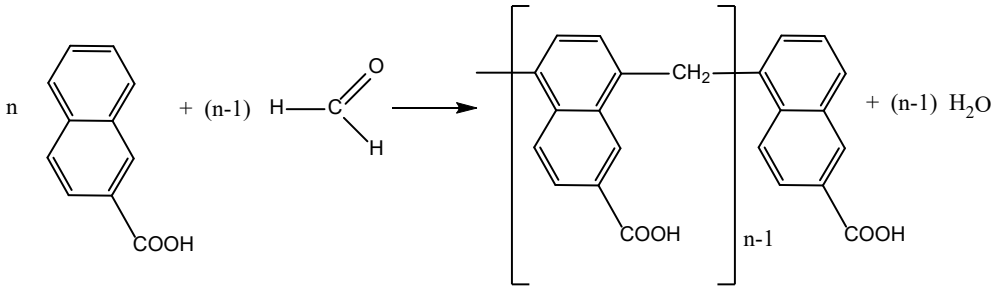

The polycondensation process is carried out at a temperature of 110 °C for several days. The longer the process continues, the higher the content of the polymerized substance in the product, as well as the higher the content of the active substance. The completion of the process is monitored through sampling. When cooled, the resulting polycondensate transforms into a viscous mass. When stretched, it forms thin fibers and dissolves in water.

To reduce the time and energy consumption of the polycondensation process, the reaction was carried out at high temperature and high pressure in a special setup, allowing the reaction to be completed within a few hours. Formalin is introduced into the reaction mixture from multiple points and below the reaction mass to ensure uniform distribution throughout. If formalin is added from a single point, it can increase the viscosity of the reaction mass, potentially leading to issues such as mixer failure and other complications.

During the neutralization stage of the polycondensation process, the sodium salts of polymethylenenaphthalene carboxylic acid are formed by treating the condensed mass with sodium hydroxide. The condensed mass is mixed with a specific amount of water and then diluted and cooled. Next, an alkali solution is added, and the mixture is stirred until the medium becomes neutral.

The reaction equation for the neutralization process is as follows:

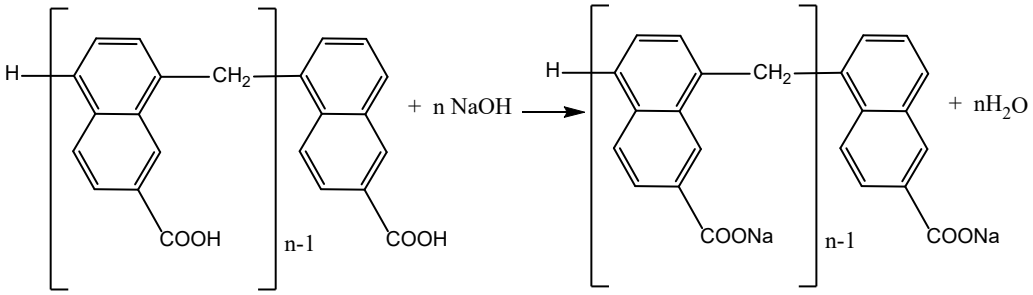

During the synthesis of the additive, the residual formaldehyde mass fraction of 0.001% remains higher than usual, which cannot be used in the composition of construction materials used for the interior decoration of buildings with a lot of people.

To reduce the mass fraction of residual formaldehyde in the production process of the additive, they proposed to use the Cannizzaro reaction. Formaldehyde molecules interact and turn into various harmless organic substances. In such a process, a disproportionation reaction occurs, one molecule of formaldehyde is reduced and the second molecule is oxidized, alkalis play the main role as a catalyst of the process (Bellami L. 1971):

$$2CH_2O + H_2O = CH_3OH + HCOOH$$

Aldehydes without a hydrogen atom in the alpha state undergo disproportionation under the influence of concentrated alkali solutions to form carbonic acid and alcohol.

The mechanism of the Cannizzaro reaction combines a two-stage nucleophilic addition reaction: in the first stage, the hydroxyl anion is attached to the carbonyl group of the formaldehyde molecule, then hydrogen is released from this adduct compound in the form of a hydride-anion and combines with the second molecule of formaldehyde. For example, formaldehyde is converted into methyl alcohol with potassium formate (since there is potassium hydroxide in the environment).

The Cannizzaro reaction was carried out at a high temperature of 100 °C for several hours. After the process was completed, the product was neutralized with a low-concentration sulfuric acid solution. As a result, the mass fraction of formaldehyde in the liquid product of the process did not exceed 0.001%.

To evaluate the transportability of the synthesized additive solution, the relationship between its concentration and density was determined. The results of the experiments are presented graphically in Figure 1. One of the most important characteristics of the diluent-plasticizer, which affects the gypsum mixture, determined by the Suttard method, is the plasticity index (Orifjon Kadyrov, Zilola Karimova, 2023).

Figure 1. *Graph of dependence of additive density on solution concentration*

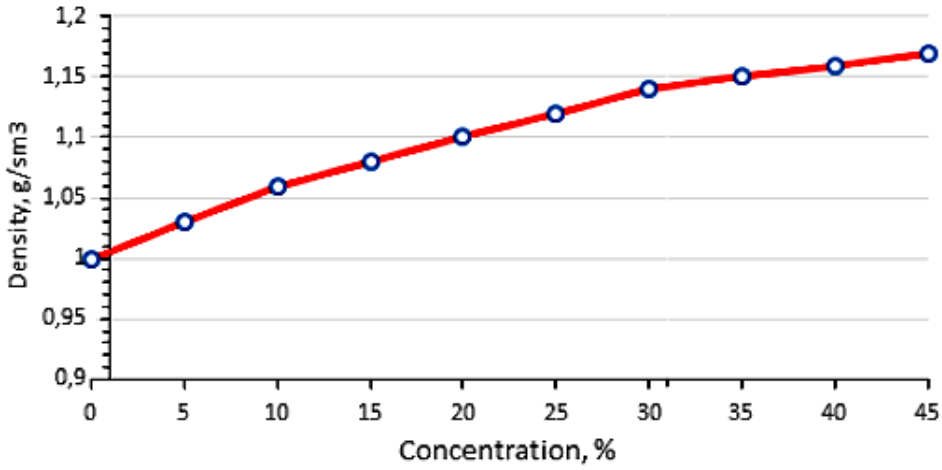

To synthesize polymethylenenaphthalene carboxylic acid (cationic) with a spatial structure, the following successive works were carried out;

– Naphthalene homologs were isolated from pyrolysis oil.

– Obtained naphthalene homologs were oxidized and naphthalene carboxylic acids were synthesized. (I-reaction)

– Naphthalene polycondensates a mixture of carboxylic acids with formalin (1 : 2 molar ratio of carboxylic acids and formaldehyde) under high pressure, and the polycondensate is heated at 95 – 100 °C for 24 hours.

(Reactions II and III)

The reaction equation of the above processes is as follows:

I-reaction

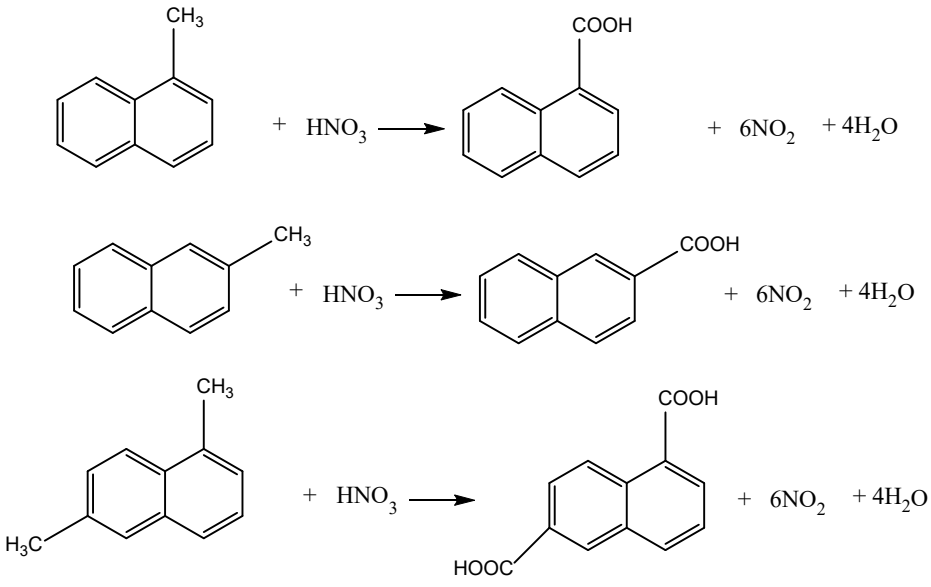

II-reaction

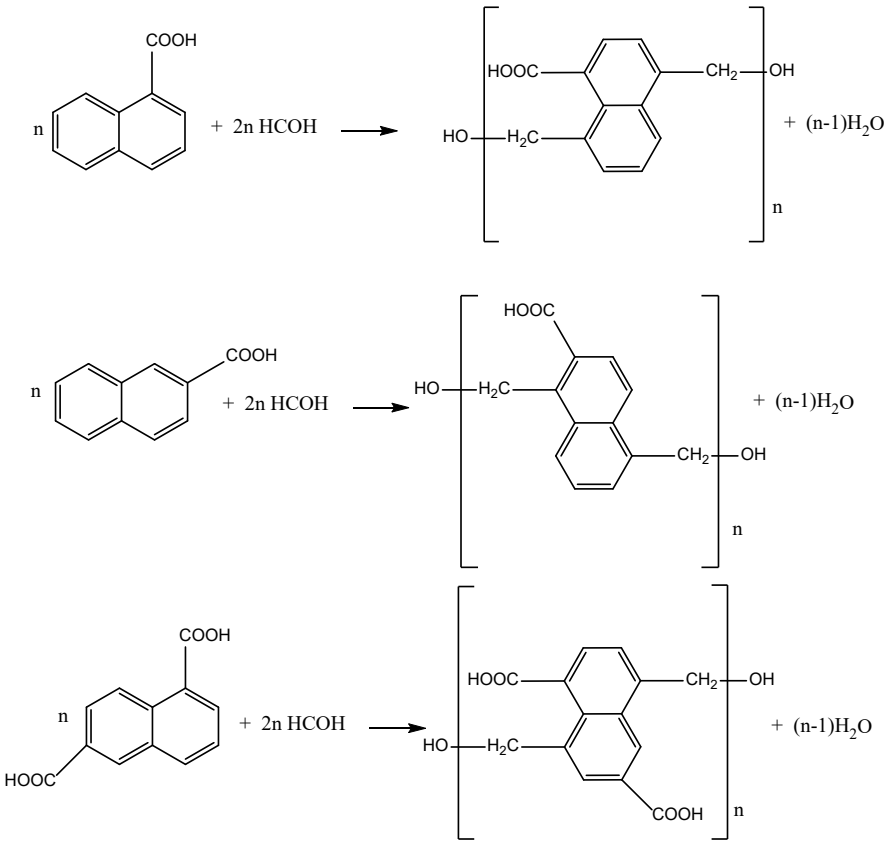

III-reaction

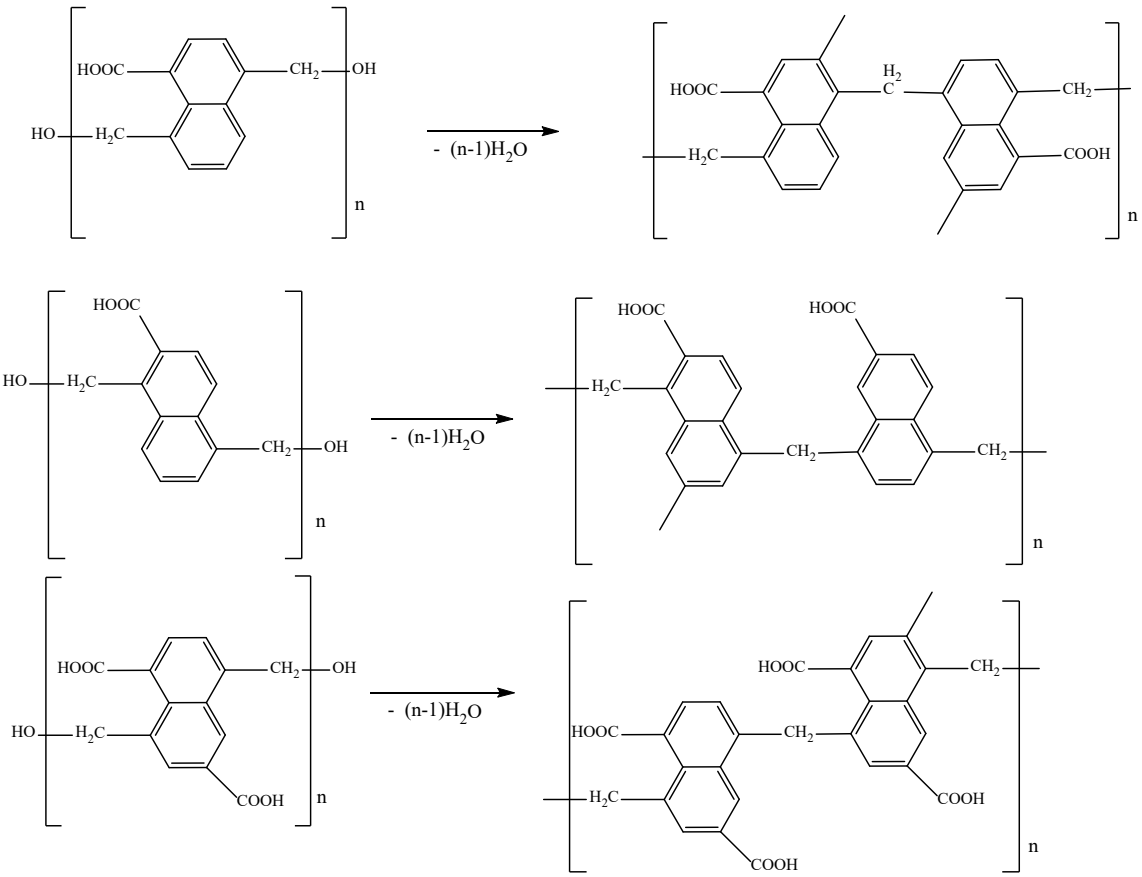

Results and discussion

The IR spectrum of synthesized 1-naphthalene carboxylic acid was obtained and analyzed.

Figure 2. *IR spectrum of 1-naphthalene carboxylic acid*

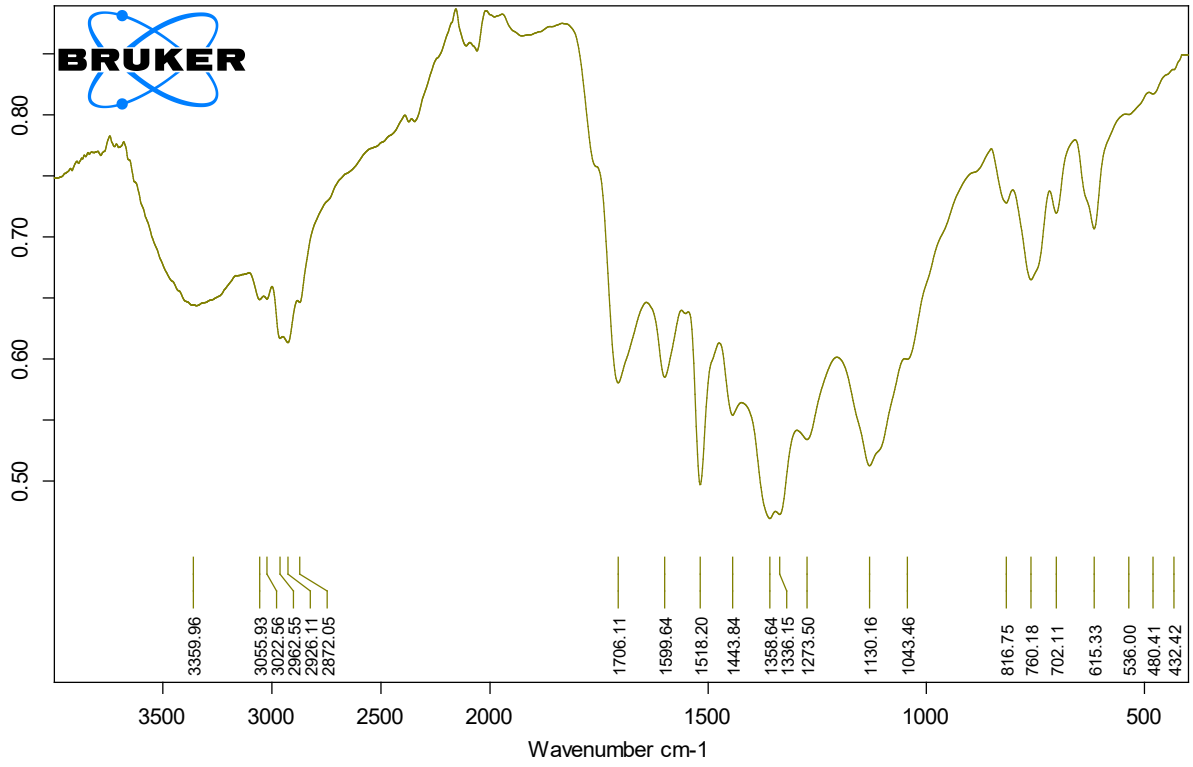

The analysis of the above IR spectrum shows that. We can see the valence vibration of the –OH group at 3359.96 sm^{-1}, the valence vibration of the C-H bond in the aromatic core at 3055.93 sm^{1}, and the valence vibration of the $-CO_2H$ group at 1130.16 sm^{-1}. The element analysis of the synthesized polymethylenenaphthalene carboxylic acid with spatial structure was performed (Figure 3).

Figure 3. *Elemental analysis of polymethylenenaphthalene carboxylic acid with spatial structure*

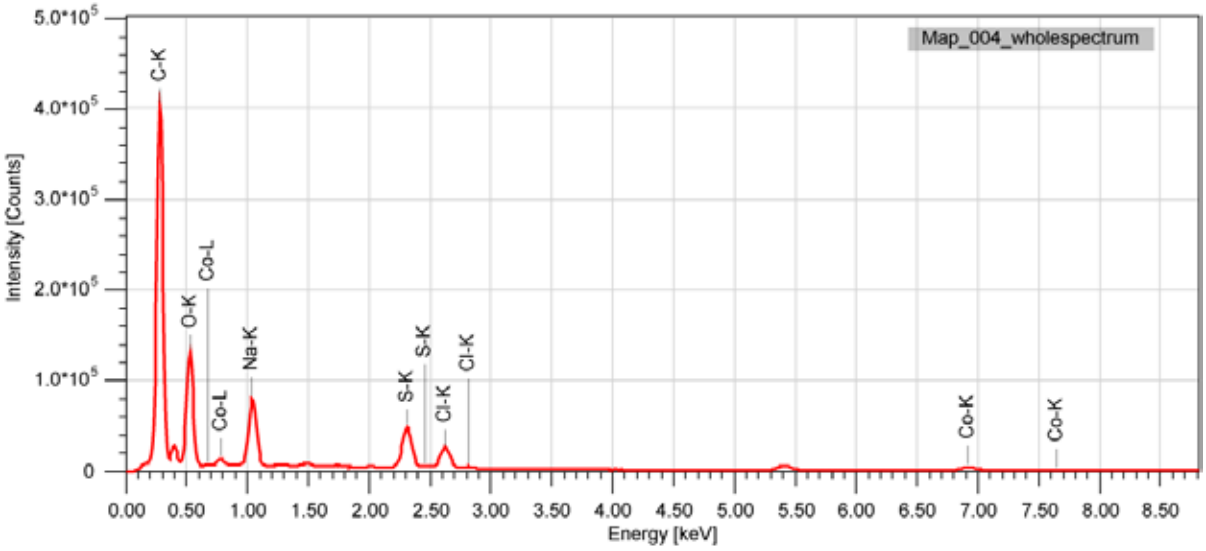

Table 3. *Results of elemental analysis of polymethylenenaphthalene carboxylic acid with spatial structure*

Element	Mass fraction (%)	A fraction of the atomic number (%)
C	62.55	71.32
O	28.3	24.22
Na	4.65	2.77
S	2.25	0.96
Cl	1.3	0.5
Co	0.96	0.22

Figure 4. *TG of carbocationite – thermogravimetric curve; DTA – differential thermal curve*

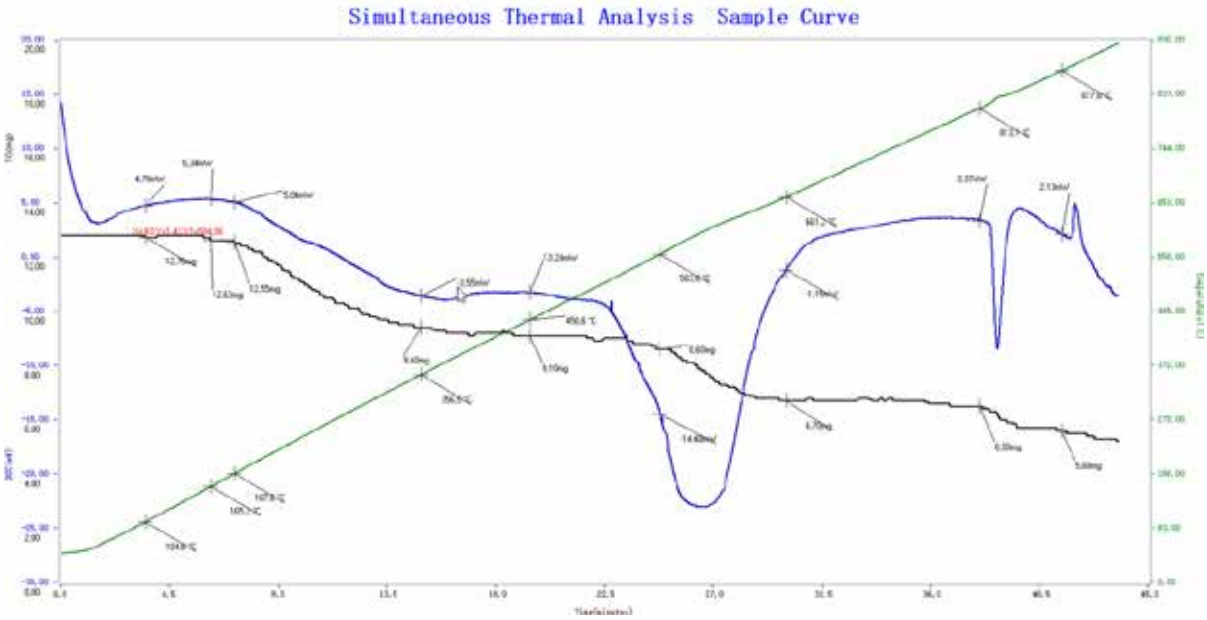

Thermal stability of carbocationite was studied by the thermogravimetric method

The data presented in the figure shows the change in sample composition with weight loss. The first stage, in the temperature range of 104.6–356.5 °C, exhibits a weight loss of 26.27%. The second stage, ranging from 450.6–661.2 °C, shows a weight loss of 21.12%. Additionally, in the temperature range of 813.1–877.8 °C, a substance mass loss of 8.63% was observed. Overall, the resulting carbocationite experienced a total mass loss of 56.07% when heated to 900 °C.

The differential thermal curve of the studied cationites shows two endothermic peaks. These endothermic effects can be attributed to the thermal degradation of the cationite, occurring in the ranges of 450.6–661.2 °C and 813.1–877.8 °C.

In the case of the KU-2 cationite, an endothermic peak with energy absorption is observed at 353–413 K, and its degradation is observed at 423 K [24–26]. This indicates that the thermal stability of the naphthalene-based cationite is higher compared to that of the KU-2 cationite.

The following operational properties of carbocationic were studied:

- specific mass of cationic
- the specific volume of the cation
- wettability of the cation
- static exchange capacity of cationic
- dynamic exchange capacity of cationic

Work was carried out according to the GOST 10896–78 international standard to prepare the received catonites for testing. For comparison, sulfocationite KU-2–8 was obtained (Table 4).

Table 4. *Synthesized carbocationic and KU-2–8(imported) sulfocationite operational properties*

№	A type of cationite / Learning method	Comparative mass (g/dm³) GOST 10898.2–74	Humidity (%) vlagamer XY-100MW	Comparison size (sm³/g) GOST 10898.4–84	Total static capacitance (mg-eq/g) GOST 20255.1––89	Dynamic exchange capacity (mol/m³) GOST 20255.2–89
1	NKK	765	54.7	4.7	4.92	512
2	KU-2–8 (control)	750–800	48–58	2.8	4.6–4.8	500–520

It can be seen from the table that the main performance properties of the synthesized NKK carbocationites are close to the static and dynamic exchangeability of imported sulphocationite KU-2–8.

Summary

Polymethylenenaphthalene carboxylic acids were obtained based on naphthalene obtained from pyrolysis oil, a secondary product of the hydrocarbon pyrolysis process, and it was found that the linear oligomer of this polymer can be used as a superplasticizer in concrete mixtures, and its spatial polymer can be used as a carbocationic.

Chromato-mass spectrum, IR spectrum, SEM analysis, elemental analysis, and TG analysis were used to study and analyze the composition, structure, and properties of the products obtained as a result of the synthesis.

The use of synthesized oligomers with a linear structure as a superplasticizer in concrete mixtures has been studied to increase the plasticity and strength of the intermediate mixture.

The cationic property of the synthesized polymethylenenaphthalene carbonic acid was studied, and it was put into practice as a cationic in the purification of circulating water in factories from various metal cations.

COE (static exchange capacity) and DOE (dynamic exchange capacity) were determined as important operational properties of cation sites. COE = 4.92 mg-eq/g, DOE = = 512 mol/m³. The static and dynamic exchange capacity of the synthesized carbocationites was studied to be close to the property of KU-2–8 sulfocationite.

The thermal stability of carbocationite was studied by the thermogravimetric method. It was found that the thermal stability of the obtained cationite based on naphthalene is higher than that of KU-2 cationite.

References

Prech E., Byul'mann F., Affol'ter K. (2006). Opredelenie stroeniya organicheskih soedinenij.

Turnbull L., Liggat J. J., Mac Donald W. A. (2013). Thermal degradation chemistry of poly (ethylene naphthalate) – A study by thermal volatilisation analysis Polymer Degradation and Stability – Vol. 98.– P. 2244–2258. URL: https://doi.org/10.1016/j.polymdegradstab.2013.08.018

Guoqiang Wang, Guitang Yang, Min. Jiang, Rui. Wang, Yin Liang, Guangyuan Zhou. (2021). Poly (propylene naphthalate-co-propylene 2,5-thiophenedicarboxylate)s derived from bio-based 2,5-thiophenedicarboxylic acid (TDCA): Synthesis and properties Polymer Testing – Vol. 93. – 106955 p. URL: https://doi.org/10.1016/j.polymertesting.2020.106955

Roupakias C. P., Bikiaris D. N., Karayannidis G. P. (2005). Synthesis, thermal characterization, and tensile properties of alipharomatic polyesters derived from 1,3-propanediol and terephthalic, isophthalic, and 2,6-naphthalenedicarboxylic acid J. Polym. Sci. Polym. Chem.,– 43 (17).– P. 3998–4011.

Jeong Y. G., Jo W. H., Lee S. C. (2002). Crystal structure of poly (pentamethylene 2,6-naphthalate) Polymer,– 43 (26).– P. 7315–7323.
Stier U., Schawaller D., Oppermann W. (2001). Rheological properties of poly (trimethylene 2,6-naphthalenedicarboxylate) melts Polymer,– 42 (21).– P. 8753–8757.
Lorenzetti C., Finelli L., Lotti N., Vannini M., Gazzano M., Berti C., Munari A. (2005). Synthesis and characterization of poly (propylene terephthalate/2,6-naphthalate) random copolyesters Polymer,– 46 (12).– P. 4041–4051.
Bellami L. (1971). Novye dannye po IK-spektram slozhnyh molekul.
Nakanisi K. (1963). Infrakrasnye spektry i stroenie organicheskih soedinenij.– M.: Mir, 1965.– 5. Bellami L. IK-spektry slozhnyh molekul
Chung, T. C. (2002). Synthesis of functional polyolefin copolymers with graft and block structures. Prog. Polym. Sci.– 27.– P. 39–85. [Google Scholar] [CrossRef]
Hustad, P. D.; Coates, G. W. (2002). Insertion/isomerization polymerization of 1,5-hexadiene: Synthesis of functional propylene copolymers and block copolymers. J. Am. Chem. Soc.– 124.– P. 11578–11579. [Google Scholar] [CrossRef] [PubMed]
Charlesby, A. (1960). Atomic Radiation and Polymers; Pergamon Press: Oxford, UK, [Google Scholar]
Chapiro, A. (1962). Radiation Chemistry of Polymeric Systems; Interscience: New York, NY, USA, [Google Scholar]
Coqueret, X. (2008). Obtaining High-Performance Polymeric materials by Radiation. In Radiation Chemistry: From Basics to Applications in Material and Life Sciences; Spotheim-Maurizot, M., Mostafavi, M., Douki, T., Belloni, J., Eds.; EDP Sciences: Les Ulis, France,– P. 131–150. [Google Scholar]
Orifjon Kadyrov, Zilola Karimova. (2023). Investigation of the process of obtaining additive for gypsumboard based on polymethylenenaphthaline carboxylic acids Universum: tekhnicheskie nauki: elektron. nauchn. zhurn.– 4(109). URL: https://7universum.com/ru/tech/archive/item/15290

submitted 22.08.2023;
accepted for publication 20.09.2023;
published 8.10.2023

Contact: shuhrat.hasanov.0305@gmail.com

The Austrian Journal of Technical and Natural Sciences, No 9–10
ISSN 2310-5607

PREMIER Publishing
ppublishing.org

DOI:10.29013/AJT-23-9.10-17-20

THERMOGRAVIMETRIC STUDY OF THE SORPTION PROPERTIES OF MODIFIED SILICA GELS

Geldiev Yusuf [1], ***Turaev Khayit*** [1], ***Umbarov Ibragim*** [1]

[1] Department of chemistry, Termez State University

Cite: *Geldiev Y., Turaev Kh., Umbarov I. (2023). Thermogravimetric study of the sorption properties of modified silica gels. Austrian Journal of Technical and Natural Sciences 2023, No 9-10.* https://doi.org/10.29013/AJT-23-9.10-17-20

Abstract

The optimal conditions of the modification process with 2-hydroxyethylcarbamate are defined in the article. Temperature dependence of carbon dioxide sorption on modified silica gels was studied.

Keywords: *silica gel, sorption, carbon dioxide, hydroxyethyl carbamate, thermal stability*

Introduction

The increase in the amount of carbon dioxide in the atmosphere has reached a historical maximum. One of the reasons for this is human activity, as a result of which the amount of gases released into the atmosphere has increased hundreds of times. Deforestation also slows down CO_2 utilization. Scientists have estimated that since the 1850s, half of CO_2 emissions are stored in the atmosphere, but most of it dissolves in ocean waters. Since 2000, the amount of CO_2 in the atmosphere has increased by 12% (Lindsey, 2020; Lüthi D., Le Floch M., Bereiter B., Blunier T., Barnola J. et al., 2008).

Solid sorbents based on amines have attracted the attention of researchers due to their high CO_2 sorption, low energy consumption, high stability, and they do not pollute the environment. Liquid adsorbents have disadvantages, such as high toxicity, foaming, they are not heat-resistant – at high temperatures they undergo destruction and/or evaporation (Geldiev Y. A., Turaev Kh. Kh., Umbarov, 2022; Santana A. M., Freire T. M., Silva L. F., Menezes F. L., Ramos L. L. et al., 2021; Wang F., Yu L. & Huang, 2021).

The main value characterizing the sorption capacity of silica gels that are modified with amino groups is the amount of nitrogen they contain. These sorbents are characterized by maximum sorption kinetics. Since most of the organic amines are on the outer surface, they have been found to fill 70% of the container in 1–10 minutes. It has been shown that the sorption kinetics increases with increasing pore size (Geldiev et al., 2023).

Synhesis method

Synthesis of 2-hydroxyethylcarbamate (HEC). According to the method presented in the literature (Belyaev P. G., Khisamutdinov G. Kh., Sharypova S. G., Konovalova V. P., Kondyukov I. Z., Valeshny S. I., Smirnov S. P., Ilyin, 2008), a mixture of urea

and ethanolamine in a 1:1 molar ratio was heated at 110 °C until gas evolution ceased.

10, 20 and 30% solutions of HEC in absolute ethyl alcohol were prepared. Samples of 5.0 g of silica gel were kept in 10.0 g of HEC solution for 2 hours. After this, it was dried at 80 °C to dry mass. The resulting sorbents, depending on the concentration of HEC in the solutions used to modify the silica gel, were designated as S HEC –10, S HEC-20 and S HEC-30.

Thermal analyzes were performed on a Shimadzu TG-600 device at 40–600 °C. To study the kinetics of sorption and desorption, the sorbents were first cleared of absorbed gases and moisture by heating in a nitrogen environment at 110 °C for 30 min, and then kept at 30 °C, 50 °C and 80 °C in a CO_2 environment until constant weight. By repeating the process, it was possible to study the operating cycles of the sorbents.

The degree of modification of the sorbent. The degree of modification of the sorbent in HES solutions was calculated from the increase in its mass. The results of changes in the mass of the samples are given in (table 1).

Table 1. *Results of modification of silica gel with HES*

Initial mass of silica gel, g	Composition of solution for HEC/Ethanol modification,%	Received sample	Weight of slick gel after modification	Weight increase,%
5.0	10/90	SHEC –10	6.08	21.6
5.0	20/80	SHEC –20	7.12	42.4
5.0	30/70	SHEC –30	7.76	55.2
5.0	40/60	SHEC –40	7.78	55.6

As can be seen from table. 1, as the concentration of HEC in the solution increased, the degree of modification of the sorbent increased significantly

Results and discussion

Study of the sorption capacity of sorbents. The change in the maximum sorption capacity during sorption/desorption cycles of modified sorbents was studied. Maximum sorption capacities were used at 30 °C for sorption and 80 °C for desorption (Fig. 1). During cyclic operation of modified sorbents in 2 temperature ranges, a decrease of 7–10% was observed after 5 sorption-desorption cycles.

Figure 1. *Cyclic change in the mass of modified silica gels during CO_2 sorption-desorption cycles in comparison with unmodified silica gel. a – SHEK-30; b – SHEC-20; c – SHEC-10; g – SIL*

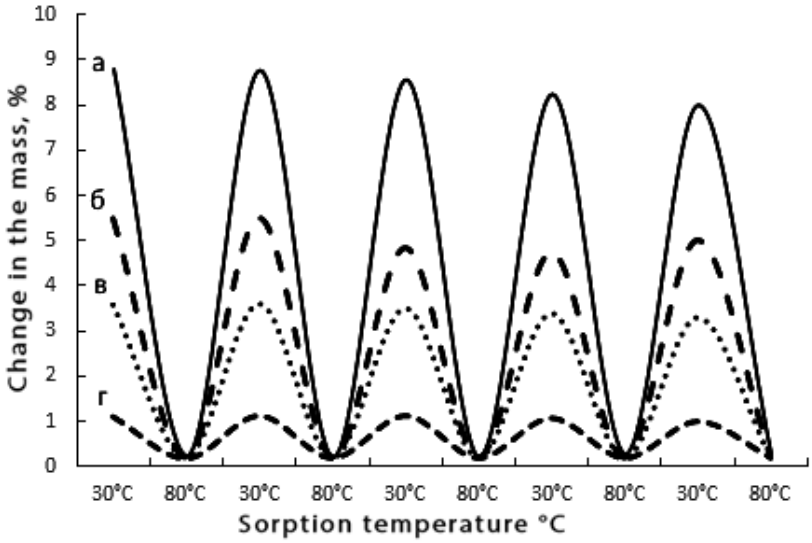

This decrease can be explained by the partial removal of amino groups at high temperature, since the sorption capacity of the unmodified SIL sample remained virtually unchanged. The optimal temperature for the desorption process was ~80 °C. At a higher temperature, desorption occurred faster and more completely, which led to a significant decrease in the number of effective operating cycles. However, if desorption was carried out at 100 °C, the maximum sorption capacity of the SHEC-30 sample after 30 minutes decreased by more than 30%.

The sorption properties of sorbents significantly depend on the temperature of the gas system. At high temperatures, their CO_2 sorption capacity decreases. CO_2 sorption at 80 °C for modified silica gel is ~0.2%, and at temperatures above 100 °C there is practically no sorption (Fig. 2).

Figure 5. *Temperature dependence of the maximum sorption capacity of sorbents: a – SIL; b – SHEC-10; c – SHEC-20; d – SHEC-30*

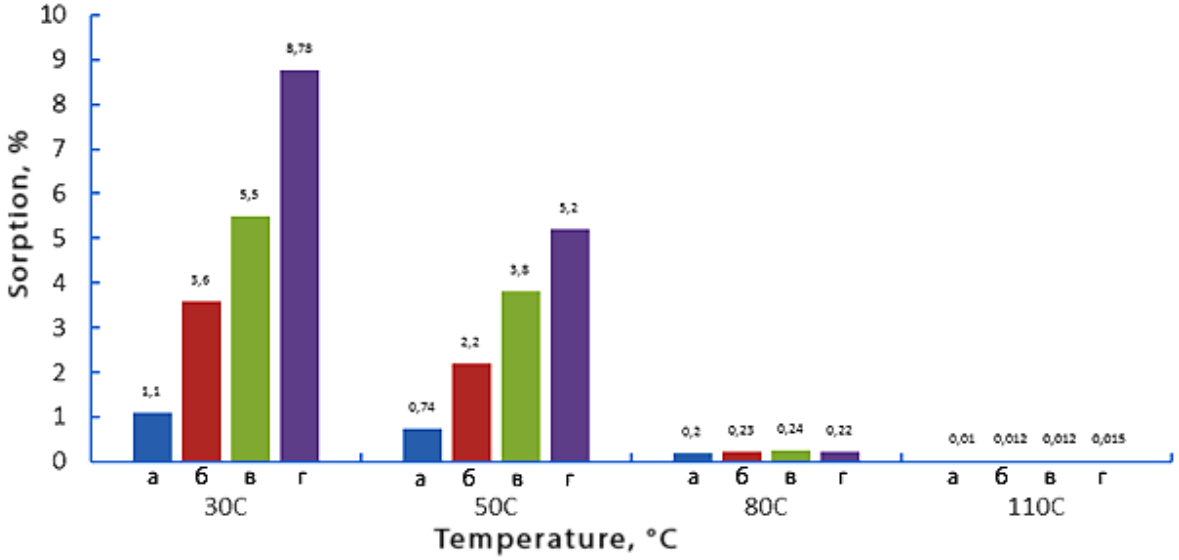

The work determined the optimal conditions for modifying silica gel with aqueous solutions of 2-hydroxyethylcarbamate (HEC). Although the surface area of HEC-modified silica gels decreased as the HEC concentration increased, the carbon dioxide sorption capacity increased.

The optimal conditions for the cyclicity of the sorption-desorption process were determined, when sorption occurs at 30 °C and desorption at 80 °C.

References

Belyaev P. G., Khisamutdinov G. Kh., Sharypova S. G., Konovalova V. P., Kondyukov I. Z., Valeshny S. I., Smirnov S. P., Ilyin, V. P. (2008). Development of a new technology for producing xymedon. *Chemical-Pharmaceutical Journal*,– 42(4).– P. 43–45.

Geldiev, Y. A., Turaev, K. K., Kasimov, S. A., Ruzimuradov, O. N., & Shilova, O. A. (2023). Studying the Sorption of Carbon Dioxide by Modified Silica Gel with 2-Hydroxyethylcarbamate. *Glass Physics and Chemistry*,– 49(2). URL: https://doi.org/10.1134/S1087659622601149

Geldiev Y. A., Turaev Kh. Kh., Umbarov, I. A. (2022). Thermal analysis of modified polysilicic acid with amino alcohols. *Austrian Journal of Technical and Natural Sciences*,– *3–4*.– P. 72–75. URL: https://doi.org/10.29013/AJT-22-3.4-72-75

Lindsey, R. (2020). Climate Change: Atmospheric Carbon Dioxide | NOAA Climate.gov. *Climate.Gov*,– P. 1–5. URL: https://www.climate.gov/news-features/understanding-climate/climate-change-atmospheric-carbon-dioxide

Lüthi D., Le Floch M., Bereiter B., Blunier T., Barnola J., M., Siegenthaler U. R. D., & Jouzel J., Fischer H., Kawamura K., Stocker, T. F. (2008). High-resolution carbon dioxide concentration record 650,000–800,000 years before present. *Nature*,– 453(7193).– P. 379–382. URL: https://doi.org/10.1038/NATURE06949

Santana A. M., Freire T. M., Silva L. F., Menezes F. L., Ramos L. L., C. G. R., Fechine M. U. D., V. L. H. S., Ferreira O. P., F. R. M., Denardin J. C., L. G. S., & Matos, W. O. (2021). Organophosphorus halloysite nanotubes as adsorbent for lead preconcentration in wine and grape juice. *Applied Clay Science*,– 200.– 105912 p. URL: https://doi.org/10.1016/j.clay.2020.105912

Wang F., Yu L., L. Y., & Huang, D. (2021). CO2 Adsorption Capacity of Organic Alkali Sorbent CPEI from Polyethyleneimine. *Adsorption Science and Technology*, 2021.– P. 854–865. URL: https://doi.org/10.1155/2021/6629365

submitted 22.08.2023;
accepted for publication 20.09.2023;
published 8.10.2023

Contact: geldi.88@mail.ru

The Austrian Journal of Technical and Natural Sciences, No 9–10
ISSN 2310-5607

PREMIER Publishing
ppublishing.org

DOI:10.29013/AJT-23-9.10-21-26

SOLUBILITY OF COMPONENTS IN THE $NH_4H_2PO_4$-$NH_2C_2H_4OH$-H_2O SYSTEM

***Saidolim Mardanov*[1], *Shokhida Khamdamova*[2]**

[1] PhD Student, Fergana Polytechnic Institute, Fergana, Uzbekistan

[2] Doctor of Sciences (DSc), Professor, International Institute of Food Technology and Engineering, Fergana, Uzbekistan

Cite: *Mardanov S., Khamdamova Sh. (2023). Solubility of Components in the $NH_4H_2PO_4$-$NH_2C_2H_4OH$-H2O System. Austrian Journal of Technical and Natural Sciences 2023, No 9-10.* https://doi.org/10.29013/AJT-23-9.10-21-26

Abstract

The solubility of components in the $NH_4H_2PO_4$-$NH_2C_2H_4OH$-H_2O system was studied from the temperature of complete freezing (–53.0 °C) to 68.0 °C. A polythermal solubility diagram has been constructed, on which the regions of crystallization of ice, monoammonium phosphate, $NH_4H_2PO_4 \cdot NH_2C_2H_4OH$, $2NH_4H_2PO_4 \cdot 3NH_2C_2H_4OH$ compounds, two-, one-, and anhydrous monoethanolamine are demarcated.

Keywords: *solubility, temperature, polytherm, diagram, crystallization, ice, mono ammonium phosphate, monoethanolamine*

Introduction

Currently, to increase the productivity of agricultural crops, the use of chemical regulators of plant growth and development is expanding simultaneously with increasing doses of mineral fertilizers. World practice has accumulated experience in growing plants with desired properties using individual chemicals with stimulating activity (Nesbit, J. C., 1860).

It has been established that ethanolamine has high biological activity. Its active participation in redox processes, in enhancing the synthesis of organophosphorus compounds, stimulating protein metabolism and enhancing the activity of enzymatic systems has been revealed.

When explaining the growth activity of ethanolamines, it should be taken into account that in the presence of carbon dioxide and oxygen, ethanolamines can form glycerol, glycol, oxalic, formic, naphthenic and acetic acids, which belong to the group of growth substances (Леопольд, А., 1968; Сухова С. И., Симочатова Е. П., Бесков С. Д., 1967; Гусейнов, Д. М., 1966; Нурахметов, Н. Н., & Беремжанов, Б. А., 1978).

Increased interest in the interaction of ethanolamines with fertilizer components, as well as chlorate-containing defoliants, is due to the fact that when used together, the effectiveness of the synthesized drugs increases. Consequently, physicochemical studies of the interaction of ethanolamines with macro-

and microcomponents of fertilizers are of significant theoretical and practical interest.

Methodology

This system at 25 °C was previously studied using isothermal methods (Набиев, М.Н., Исабаев, З., & Саибова, М.Т., 1976). We studied the solubility of the components in the $NH_4H_2PO_4$-$NH_2C_2H_4OH$-H_2O system using the visual-polythermal method (Трунин, А.С., & Петрова, Д.Г., 1978) from the temperature of complete freezing (–53.0 °C) to 68.0 °C. For quantitative chemical analysis of liquid and solid phases, elemental analysis for carbon, nitrogen, and hydrogen was used (Климова, В.А., 1975); the P_2O_5 content was determined using a spectrophotometer using the colourimetric method (Мойжес, И.Б., 1973).

The content of elemental carbon and hydrogen was carried out according to the method (Климова, В.А., 1975).

Solid phases were identified by chemical and various methods of physicochemical analysis. Thermal analysis of the new phases under study was carried out on a derivatograph of the Paulik-Paulik-Erdey system.

X-ray phase analysis was carried out on a Dron-3.0 diffractometer. The values of interplanar distances were found from the reference book (Диллер, Я.Л., 1966; Недома, И., 1975), according to the angle of reflection, and the intensity of diffraction lines was assessed on a 100-point scale.

Results and discussion

We studied the solubility of the $(NH_4)_2HPO_4$-$NH(C_2H_4OH)_2$-H_2O system (Ergashev D.A., Xamdamova Sh. Sh., 2022; Adiljonovich, E.D., & Sherzodovna, K.S., 2021; Adiljanovich, E.D., 2020; Эргашев Д.А., Асқарова М.К., Тухтаев С., 2015; Эргашев Д.А., Асқарова М.К., Тухтаев С., 2015; Ergashev Dilmurod Adiljonovich, Askarova Mamura Kamilovna, Tukhtaev Saidahral, 2016) using ten internal cuts. Of these, sections IV were studied from the side $NH_2C_2H_4OH$-H_2O to the top of $NH_4H_2PO_4$, sections VI–IX from the side $NH_4H_2PO_4$-H_2O to the top of $NH_2C_2H_4OH$.

Figure 1. *Solubility diagram for the system* $NH_4H_2PO_4$-$NH_2C_2H_4OH$-H_2O

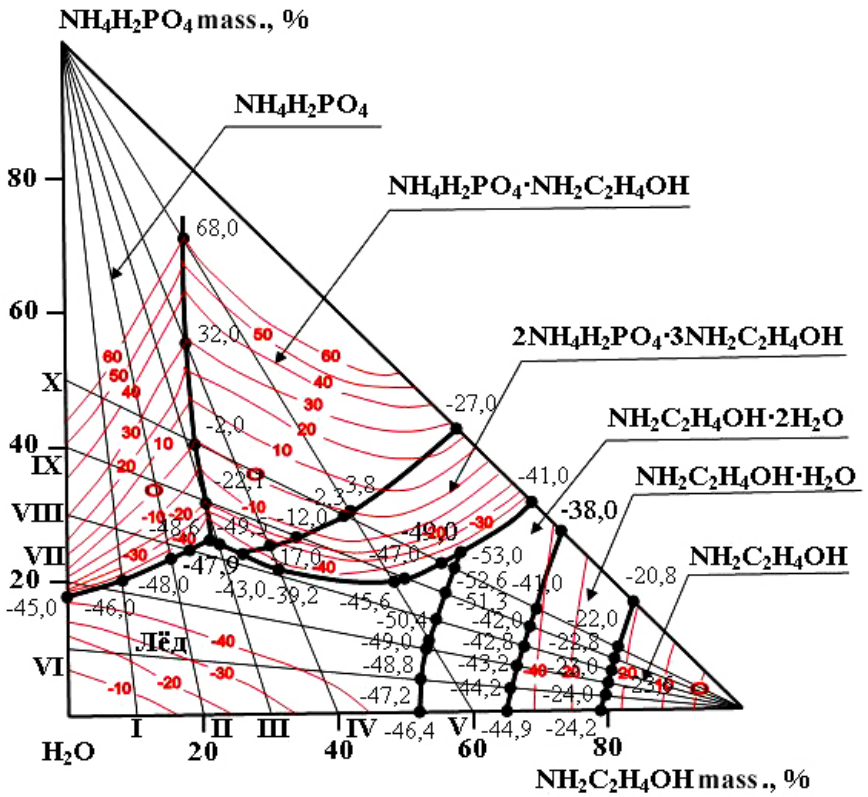

Based on the results of studying binary systems and internal sections, a polythermal solubility diagram of a ternary system was constructed, on which the fields of crystalli-

zation of ice, mono ammonium phosphate, compounds of the compositions $NH_4H_2PO_4 \cdot NH_2C_2H_4OH$, $2NH_4H_2PO_4\ 3NH_2C_2H_4OH$, two aqueous, one aqueous and anhydrous monoethanolamine are delimited (Fig. 1, Table. 1).

These fields converge at four triple nodal points of the system, for which the chemical compositions of equilibrium solutions and the corresponding crystallization temperatures are determined (Table 1).

Table 1. *Double and triple points of the $NH_4H_2PO_4$-$NH_2C_2H_4OH$-H2O system*

Composition of the liquid phase, wt.%			*Crystal temperature,* °C	Solid phase
$NH_4H_2PO_4$	$NH_2C_2H_4OH$	H_2O		
18.0	–	82.0	–45.0	Ice + $NH_4H_2PO_4$
20.0	8.0	72.0	–46.0	Same
23.4	15.5	61.1	–48.0	—
24.6	18.3	57.1	–48.6	—
26.0	23.1	50.9	–49.5	Ice + + $NH_4H_2PO_4$ + $NH_4H_2PO_4$·N-$H_2C_2H_4OH$
71.0	17.8	11.2	68.0	$NH_4H_2PO_4$ + $H_4H_2PO_4$·N -$H_2C_2H_4OH$
55.4	18.0	26.6	32.0	Same
40.2	19.2	40.6	–2.0	—
31.6	20.5	47.9	–22.1	—
25.5	22.6	51.9	–47.9	Ice + $NH_4H_2PO_4$·$NH_2C_2H_4OH$
23.9	25.9	50.2	–43.0	Ice + $NH_4H_2PO_4$·$NH_2C_2H_4OH$ + +$2NH_4H_2PO_4$·$3NH_2C_2H_4OH$
25.3	29.0	45.7	–17.0	$NH_4H_2PO_4 \cdot NH_2C_2H_4OH$ + $2NH_4H_2PO_4$·$3NH_2C_2H_4OH$
26.2	33.8	40.0	–12.0	Same
29.5	41.2	29.3	–2.3	—
30.0	42.1	27.9	3.8	—
42.0	58.0	–	27.0	—
21.7	31.5	46.8	–39.2	Ice + $2NH_4H_2PO_4 \cdot 3NH_2C_2H_4OH$
19.8	48.3	31.9	–45.6	Same
20.0	50.0	30.0	–47.0	—
22.3	55.5	22.2	–49.0	—
23.9	58.5	17.6	–53.0	Ice + $2NH_4H_2PO_4 \cdot 3NH_2C_2H_4OH$ + +$NH_2C_2H_4OH \cdot 2H_2O$
31.0	69.0	–	–47.7	$2NH_4H_2PO_4 \cdot 3NH_2C_2H_4OH$ + + $NH_2C_2H_4OH$·$2H_2O$
21.5	57.5	21.0	–52.6	Ice + $NH_2C_2H_4OH \cdot 2H_2O$
17.8	56.0	26.2	–51.3	Same
13.9	54.6	31.5	–50.4	—
11.0	53.5	35.5	–49.0	—
9.4	53.0	37.6	–48.8	—
5.0	52.3	42.7	–47.2	—
–	52.0	48.0	–46.4	—

Composition of the liquid phase, wt.%			*Crystal temperature, °C*	Solid phase
$NH_4H_2PO_4$	$NH_2C_2H_4OH$	H_2O		
26.2	73.8	–	–38.0	$NH_2C_2H_4OH \cdot 2H_2O$ + + $NH_2C_2H_4OH \cdot H_2O$
15.7	69.5	14.8	–41.0	Same
12.7	68.7	18.6	–42.0	—
9.9	67.8	22.3	–42.8	—
7.0	66.5	26.5	–43.2	—
5.8	65.8	28.4	–44.2	—
–	65.0	35.0	–44.9	—
16.0	84.0	–	–20.8	$NH_2C_2H_4OH \cdot H_2O + NH_2C_2H_4OH$
9.7	81.8	8.5	–22.0	Same
7.9	81.0	11.1	–22.8	—
6.0	80.8	13.2	–23.0	—
4.2	80.3	15.5	–23.6	—
2.2	79.8	18	–24.0	—
–	79	21	–24.2	—

The polythermal diagram plots solubility isotherms every 10 °C. To clarify the nodal triple points, projections of polythermal solubility curves onto the corresponding lateral water sides of the concentration triangle were constructed.

Analysis of the solubility diagram of the studied system shows that the formation of the compound $2NH_4H_2PO_4 \cdot 3NH_2C_2H_4OH$ occurs in the temperature range –53.0 ÷ ÷ 27.0 °C. The minimum concentration of ammonium phosphate causing crystallization of $2NH_4H_2PO_4 \cdot 3NH_2C_2H_4OH$ into the bottom phase is 19.8%, and monoethanolamine is 24.0%. The formation of a compound with the composition $NH_4H_2PO_4 \cdot NH_2C_2H_4OH$ is observed at a higher temperature range –49.5 ÷ 68.0 °C and at higher concentrations of ammonium phosphate 24.1 ÷ 70.8%

From the data presented, it is clear that in the system under study, two chemical compounds are formed based on the initial components, i.e. $NH_4H_2PO_4 \cdot NH_2C_2H_4OH$, $2NH_4H_2PO_4 \cdot 3NH_2C_2H_4OH$, which are isolated from the expected areas and identified by chemical, thermogravimetric and X-ray phase analysis methods.

Chemical analysis of the isolated compounds gave the following results:

for $2NH_4H_2PO_4 \cdot 3NH_2C_2H_4OH$;

found,%: N= 15.01; H= 6.98; C = 16.87; P_2O_5= 35.02;

calculated,%: N= 16.95; H= 7.51; C = 17.43; P_2O_5= 34.38;

for $NH_4H_2PO_4 \cdot NH_2C_2H_4OH$;

found,%: N= 15.13; H= 6.79; C= 13.07; P_2O_5= 40.51;

calculated,%: N= 15.9; N= 7.38; C = =13.64; P_2O_5= 40.33;

A comparison of the data from X-ray diffraction and thermogravimetric analyses of the starting substances and $2NH_4H_2PO_4 \cdot$ $\cdot 3NH_2C_2H_4OH$, $NH_4H_2PO_4 \cdot NH_2C_2H_4OH$ showed that the isolated compounds have their own inherent crystal lattices and are characterized by specific transformations. The values of interplanar distances and intensities are given in Table 2.

According to thermal analysis data, in the range of 20–600 °C, five endothermic effects are observed on the heating curve of the compound $2NH_4H_2PO_4 \cdot 3NH_2C_2H_4OH$, corresponding to the melting and decomposition of the compound. The total mass loss at 600 °C is 68.7%. On the heating curve of the compound $NH_4H_2PO_4 \cdot NH_2C_2H_4OH$, four endothermic and one exothermic effect are observed. That is, the thermal analysis data are identical to the literature data [6].

Table 2. *Values of interplanar distances* $NH_4H_2PO_4$ $2NH_4H_2PO_4 \cdot 3NH_2C_2H_4OH$ и $NH_4H_2PO_4 \cdot NH_2C_2H_4OH$

$NH_4H_2PO_4$		$2NH_4H_2PO_4 \cdot 3NH_2C_2H_4OH$		$NH_4H_2PO_4 \cdot NH_2C_2H_4OH$	
d, Å	J/J1,%	d, Å	J/J1,%	d, Å	J/J1,%
5.32	100	8.35	77	8.99	100
3.75	64	5.00	72	5.40	63
3.07	89	4.51	63	4.71	93
3.06	75	4.00	95	4.18	66
2.66	18	3.65	100	3.86	73
2.65	15	2.82	45	2.91	26
2.37	8	2.59	36	2.63	23
2,009	29	2.31	18	2.40	20
2,004	22	2.27	22		
1.77	5				

In addition, in the studied system, the salting effect of the components on each other is observed. With increasing concentration and temperature, the salting-in effect of monoethanolamine on ammonium phosphate increases. So, with a 10% content of monoethanolamine in solution, the solubility of monoammonium phosphate at temperatures is 0.0; 10.0; 20.0; and 30.0 °C increases by 11.2 accordingly; 14.0; 18.0 and 20.9% compared to its solubility in water. Monoammonium phosphate has a lesser ability to increase the solubility of monoethanolamine than the latter does to the solubility of ammonium phosphate.

Conclusions

The results of the studied system indicate the technological possibility of obtaining compounds with physiologically active properties by joint dissolution of the initial components at their optimal ratios, also identified from the data of agrochemical tests.

References

Nesbit, J. C. (1860). On Agricultural Chemistry. Longman & Company.

Леопольд, А. (1968). Рост и развитие растений.– М.: Мир.– 494 с.

Сухова С. И., Симочатова Е. П., Бесков С. Д. (1967). О физиологической активности мочевины, борной и корбоновых кислот. «Агрохимия»,– № 2.– С. 96–99.

Гусейнов, Д. М. (1966). Изучение и применение нефтяного ростового вещества (НРВ) в сельском хозяйстве культур. Нефтяные удобрения и стимуляторы в сельском хозяйстве.– Баку: Изд-во АН АзССР,– С. 7–11.

Нурахметов, Н. Н., & Беремжанов, Б. А. (1978). О взаимодействии неорганических кислот с амидами. Журн. неорг. химии,– 23(2).– С. 504–514.

Набиев, М. Н., Исабаев, З., & Саибова, М. Т. (1976). Система моноаммонийфосфат-моноэтаноламин-вода при 25 С. Журн. неорганич. химии,– 21(12).– С. 3355–3358.

Трунин, А. С., & Петрова, Д. Г. (1978). Визуально-политермический метод.– Куйбышев: Куйбышевский политехнический институт, 1977.– 94 с. Рук. Деп. В ВИНИТИ,– 6.– С. 584–78.

Климова, В. А. (1975). Основные микрометоды анализа органических соединений. Химия.

Мойжес, И. Б. (1973). Руководство по анализу в производстве фосфора, фосфорной кислоты и удобрений.

Климова, В. А. (1975). Основные микрометоды анализа органических соединений. Химия.– 224 с.

Диллер, Я. Л. (1966). Таблицы межплоскостных расстояний.– Т. 2. – М. Недра,– 362 с.

Недома, И. (1975). Расшифровка рентгенограмм порошков. М.: Металлургия,– 197.– 423 с.

Ergashev D.A., Xamdamova Sh. Sh. (2022). Studying the Interaction of Components in Aqueous Systems with Calcium Chlorate, Ethanolamines, Di- and Triethanolamine. Neuro-Quantology.– 20(5).– P. 1453–1466.

Adiljonovich, E.D., & Sherzodovna, K.S. (2021). Obtaining a New Defolating Composition with Physiological Activity. International Journal of Human Computing Studies,– 3(4).– P. 20–26.

Adiljanovich, E.D. (2020). Interaction of components in aquatic systems with the chlorates and chlorides calcium, magnesium and acetate monoethanolammonium. European Journal of Molecular and Clinical Medicine,– 7(7).– P. 868–874.

Эргашев Д.А., Асқарова М.К., Тухтаев С. (2015). Изотерма растворимости системы $Ca(ClO_3)_2$-$ClCH_2CH_2PO(OH)_2 \cdot 2NH_2CH_2CH_2OH$-$H_2O$ при 25°С. Узбекский химический журнал.– Ташкент, № 1.– С. 26–29.

Эргашев Д.А., Асқарова М.К., Тухтаев С. (2015). Изучение взаимного влияния компонентов в системе хлорат кальция – ацетат моноэтаноламина- вода. Узбекский химический журнал.– Ташкент,– № 3.– С. 30–34.

Ergashev Dilmurod Adiljonovich, Askarova Mamura Kamilovna, Tukhtaev Saidahral. (2016). Physico-chemical studies of novel chlorate containing defoliant. Austrian Journal of Technical and Natural Sciences,– № 5–6.– P. 58–63.

submitted 22.08.2023;
accepted for publication 20.09.2023;
published 8.10.2023

Contact: s.mardonov82@yandex.ru

The Austrian Journal of Technical and Natural Sciences, No 9–10
ISSN 2310-5607

PREMIER Publishing
ppublishing.org

DOI:10.29013/AJT-23-9.10-27-31

THE COMPOSITION AND PROPERTIES OF GLAUCONITE SANDS AND NODULAR PHOSPHORITES OF KARAKALPAKSTAN AND THE PRODUCTION OF FERTILIZERS BASED ON THEM

Bauatdinov S.[1], Bauatdinov T.S.[1], Toreshova N.M.[1]

[1] Karakalpak Scientific Research Institute of Natural Sciences,
Karakalpak Branch of the Academy of Sciences of the Republic of Uzbekistan, Nukus

Cite: *Bauatdinov S., Bauatdinov T.S., Toreshova N.M. (2023). The Composition and Properties of Glauconite Sands and Nodular Phosphorites of Karakalpakstan and the Production of Fertilizers Based on Them. Austrian Journal of Technical and Natural Sciences 2023, No 9-10. https://doi.org/10.29013/AJT-23-9.10-27-31*

Abstract

The article presents the physical and mechanical characteristics and chemical composition of the initial raw materials – glauconite sand and nodular phosphorites of the Krantau, Khojakul, Beshtyu be and Sultan-Uizdag deposits. The methods of determining the chemical composition and commercial quality, as well as conducting physico-chemical studies of raw materials – glauconite sand and nodular phosphorites of Karakalpakstan and finished products using modern research instruments (X-ray, electron microscopic, thermal, optical emission spectrometer with inductively coupled argon plasma – ECO with ISP, HPLC-mass-spectrometry, ESI mass spectrometry studies, elemental analysis).

Keywords: *chemical composition, commercial quality, physico-chemical research of raw materials, phosphate flour, RA fertilizers*

Glauconite – monoprismatic greenish mineral from the group of layered hydrous silicates, with a specific gravity of 1.7–1.9 g/cm ^{3}. Its ion exchange capacity is 0.1–0.4 mol/ kg; porosity 20–25%; hardness 1.3–2.0; Density – 1.8–3.0.

The cation exchange capacity of glauconite concentrate varies from 390 to 550 mg/ eq per 1 gram of sample. According to its structural and geochemical properties, glauconite is a multi-purpose mineral raw material. The following areas of application of glauconite are offered:

1. As microelement-containing fertilizers.

2. As a hard water softener. One ton of glauconite softens 810 m^{3} of water of any hardness. Glauconite can withstand more than 500 regenerations per year.

3. To purify wastewater from heavy metals. According to the Institute of Botany of the Academy of Sciences of the Republic of Uzbekistan, when treating wastewater from the Tashkent Cable Plant, the content of metal salts decreased: Cu from 114.5 to 4.6 mg/l; Sn from 375 to 2 mg/l; Zn from 380 to 40 mg/l. Maximum absorption capacity in relation to heavy metals: Cu – 781.2; Ni – 342.4; Fe – 1317 mg/ eq per 1 kg of mineral. The

ability of glauconite to extract heavy metals from solutions is (in% of the initial content): Pb –99, Hg –64, Co –97, Cd –96, Mn –95, Cr –92, Ni –90, Zn –90, Fe – 99.

4. Glauconite effectively absorbs radionuclides Ce –137 and Zr-90, reducing the total β-activity of water by 28–203 times, and is used for decontamination of waters and soils with increased radioactivity. Moreover, glauconite is an active absorber of various organophosphorus, organofluorine and sulfur-containing pesticides, sharply reducing their content in the soil and aquatic environment.

5. Glauconite increases the accumulation of nutrients in the soil, improves the water-physical regime and soil structure, and activates the activity of soil microflora. As a result, the yield of grains and legumes increases by 10–40%, root crops by 30–35%. Glauconite has a positive effect on the yield of green mass of annual grasses and corn, increases the germination rate (up to 40%) of legumes and cereals, and reduces the incidence of plant diseases.

6. In livestock and poultry farms, glauconite can be used as a feed additive.

The chemical formula of conditioned glauconite can be presented as: $(R_2O + RO) * R_2O_3 * *4\ SiO_2 * H_2O$, where – R_2O – K_2O; Na_2-RO - MgO, CaO, FeO; R_2O_3 – Fe_2O_3, Al_2O_3.

The properties and effectiveness of natural phosphates from various deposits were studied (Beskrovny Yu.V., Veretennikov G.G., Galkina N.V., Ibadullaev E.I., Mirkhodzhaev I.M., 1970) using a Guinier focusing camera monochromator FR–552 carried out a precision determination of the structural characteristics of a phosphate substance without its fractional isolation. In this work, the linear dependence of the agrochemical characteristics of known types of phosphate raw materials from various deposits on the value of the parameter "ao" and "co" of the unit cell was determined. According to the obtained ao values, phosphorites are arranged in increasing order: group 1 includes nodular phosphorites, group 2 granular, group 3 shell phosphorites, and group 4 apatite. The minimum cell parameter values are found in nodular phosphorites, and the maximum values are found in apatites. It is concluded that the smaller the crystal size, the higher the agrochemical efficiency (Bushuev N.N., 2008). Based on this, we can conclude that nodular phosphorites can be directly used as fertilizer in the form of crushed flour, without resorting to many years of testing.

Among the agronomic ores of Karakalpakstan, nodular phosphorites occupy a special place. In nodular phosphorite, the relative content of lemon-soluble P_2O_5 reaches up to 40%, much more than in the Karatau and Kyzylkum ores, especially apatite ores (Veiderma M.A., 1977) This predicts the prospects for its use as a mineral fertilizer in the form of phosphate or as part of standard mineral fertilizers (Seitnazarov A.R., Turdialiev U.M., Namazov Sh.S., Beglov B.M., Dekhkanov Z.K., Kurbaniyazov R.K., 2017).

In table 1 and 2 show the chemical composition of glaconite sands and nodular phosphorites of Karakalpakstan, used as raw materials for the production of organomineral fertilizers. The content of P_2O_5 in the samples is relatively low and ranges from 6.19–22.84%. The highest content of P_2O_5 is observed in the ore of the Khodzhakul and Sultan- Uizdag occurrences. The sample from Beshtyube is the poorest phosphate mineral in phosphorus. The P_2O_5 content in them ranges from 5.8 to 7.98%. Calcite reaches 55–58% of the ore mass. Phosphorites are distinguished by high ratios $R_2O_3 : P_2O_5$ and $Fe_2O_3 : P_2O_5$.

To develop a technology for producing organomineral fertilizers based on agricultural ores of Karakalpakstan, information on physical and mechanical properties is needed. These properties include: humidity, bulk density, angle of repose, fluidity, pH, hygroscopicity and moisture holding capacity. The results of these properties are given in Table 3.

So, at a humidity of 2.0–2.28%, the free bulk density for Krantausky is 0.99 g/cm ^{3}; for Beshtyubinsky – 1.02 g/cm^3; for Khodzhakul glauconite – 1.21 g/cm^3, and with compaction it is 1.28; 1.48; 1.35, respectively. The angle of repose for the Krantau glauconite is 25 degrees; for the Khodzhakul and Beshtyubinsk glauconites, this figure is 22–26 degrees. Their flowability is 18.04–19.17 seconds. Determination of fluidity showed that they are equal to 10 points for all samples. The hygroscopic point for the 1st sample was equal to 37.3%; 2nd – 39.9%; 3rd – 38.7%. Their low value is explained by the ability of glauconite to swell in water and retain it in large quantities in the

interplanar spaces. The maximum moisture capacity of glauconite clays is 6.24–7.52%, and at higher humidity the raw material loses its friability. Glauconites with a pH from 6.92 to 7.95 normalize soil acid- base balance. It should be noted that the dispersed composition and physical and mechanical properties of various samples for different times from the Krantau deposit as an additive.

During the reporting period, organomineral fertilizers were obtained in laboratory conditions by chemical activation of phosphorites and glauconites of Karakalpakstan with ammonium sulfate and nitrate. Phosphorus in the soil is in the form of tricalcium phosphate, which does not dissolve in the soil solution. As a result of using the new fertilizers we have received, phosphorus in the soil turns into a soluble form.

Based on the chemical activation of Khodzhakul phosphate rock and glauconite from the Krantau deposit, phosphorus-containing fertilizers were obtained. Applying these phosphorites directly, as fertilizers, without prior activation is not effective.

The mechanism of the process of activation of phosphorites with solutions of ammonium sulfate and ammonium nitrate proceeds according to the following scheme. Under the influence of solutions of ammonium salts, the main minerals (calcium fluorapatite and calcite) of phosphorite decompose. An exchange reaction occurs between the components of phosphorite and the activating reagent. As a result of the dissociation of ammonium sulfate, an acidic environment is formed in the solution. The resulting acid ions react primarily with calcite. At the next stage, with the entry of ions into fluorocarbonate -apatite, the diffusion process is accelerated and their specific effective surface area increases. In the solution, aqueous and plant-assimilated forms of P_2O_5 phosphate minerals are formed.

The study established that the process of activation of FM with a solution of ammonium nitrate (pH = 4.4 – 4.8) compared to ammonium sulfate proceeds more slowly. When 2 rFM is processed in a 2% solution of ammonium nitrate, the content of the digestible form of P_2O_5 is 31.5%, and 11.6% R_2O_5 is in water-soluble form. With an increase in the concentration of ammonium nitrate solution from 5 to 20%, the content of the digestible form of P_2O_5 increases by an average of 1.35 times. After activation, the reaction medium becomes almost neutral. The weight ratios of phosmuca and glauconite were 10(10 : 1; 10 : : 2; 10 : 3; 10 : 4; 10 : 5).

Phosphate rock and different weight ratios of glauconite were taken10 gr

No.	1	2	3	4	5
	10 + 10 1 : 1	10 + 20 1 : 2	10 + 30 1 : 3	10 + 40 1 : 4	10 + 50 1 : 5

In the first version, the mixture was stirred in a porcelain cup and moistened with water, after which, stirring vigorously, it was poured onto a sieve, where granules were formed. The resulting granules were dried in a thermostat for 2 hours at a temperature of 80–100 °C. The external shape of the product granules is similar to the shape of ammonium nitrate granules. After that, the strength of the resulting granules of size 2 was measured 3 мм and a chemical analysis was carried out for the digestible form of P_2O_5. Experimental data are shown in Table 4.

Figure 1. *Phosphorus content and its relative digestibility in fertilizer made from glauconite and phosmuca Khodzhakul deposit in various mass ratios (ammonium sulfate)*

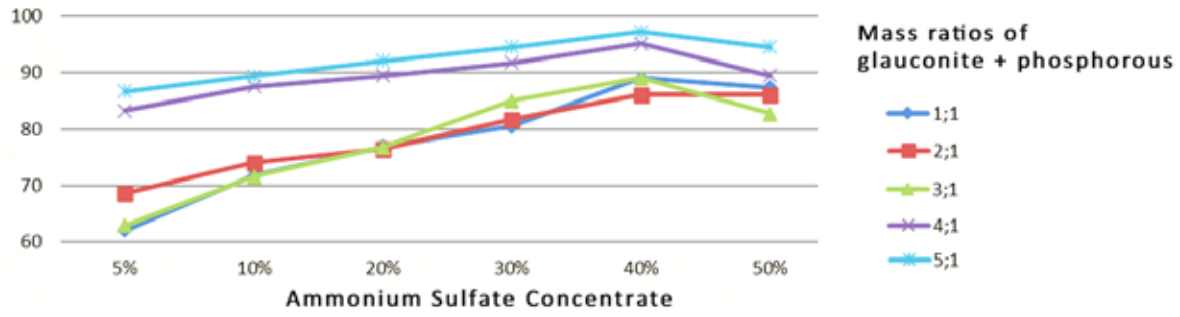

It should be noted that recently microelement-containing fertilizers are practically not used in the cultivated areas of the Republic, although plants need them only in very small quantities, but without them plants cannot develop normally. This is explained by the fact that microelements are part of enzymes, vitamins, hormones and other physiologically active compounds that play an extremely important role in the processes that occur in living organisms.

Phosphorus and glauconite sand as additives, due to the fact that glauconite, a clay mineral of variable composition, has a high content of a complex of macro and microelements. The beneficial effect of glauconite on increasing plant productivity is manifested in various directions. It improves the soil structure, increasing its permeability, which is especially important on heavy soils. Possessing high selectivity towards large cations, glauconite accumulates such essential plant nutrition elements as nitrogen, phosphorus and potassium in the form of bulk cations and sorbs NH 3, and then slowly releases them during plant growth, playing the role of a prolongator. Digestible forms of fertilizers adsorbed by glauconite are preserved from leaching; the loss of ammonia nitrogen due to nitrification and volatilization is reduced.

Table 2. *Phosphorus content and its relative digestibility in phosphate fertilizer Khodzhakul deposit and glauconite in various mass ratios*

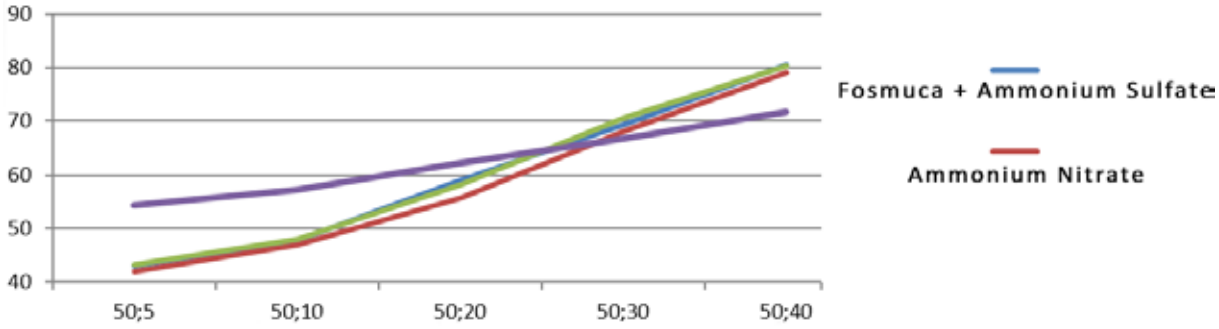

Therefore, we carried out its granulation in laboratory conditions using the rolling method. To do this, the dust-like product was placed in a porcelain cup, the required amount of water was dosed and vigorously stirred with a glass rod. In this case, moist round- shaped particles were formed; the mass of these particles was dried at 80 °C, and solid granules were obtained. They cooled and then dispersed particle 3 ммsize 2 – were analyzed for granule strength.

Experiments were carried out with various mineral salts at different ratios with phosphate flour and glauconite.

The results show that the mechanochemical activation of phosphate flour with potassium dihydrogen phosphate and potassium chloride produces highly concentrated RA fertilizers containing from 16.97–25.78% of the total form of P_2O_5.

The amount of nutritional components in the products ranges from 67.81 to 84.80% for citric acid; the granules of the resulting products have sufficient strength (2.17––5.19 MPa).

With the addition of glauconite, the relative content of the digestible form of P_2O_5 increases relative to the total, ranging from 80.26–96.60% granule strength (from 2.59––3.72 MPa) and meets the requirements of agriculture.

References

Beskrovny Yu. V., Veretennikov G. G., Galkina N. V., Ibadullaev E. I., Mirkhodzhaev I. M. Glacuonite from the Changi deposit and prospects for its use.– Tashkent: Publishing house "FAN", 1970.– 54 p.

Bushuev N. N. Correlation of the structural features of phosphate raw materials and the chemical activity of phosphate flour based on the results of comparative calculations // Physico-chemical properties of solutions and inorganic substances: Coll. scientific_labor.– in exp. 182.– M.: RKhTU im. D. I. Mendeleeva, 2008.– P. 36–47.

Veiderma M. A. Comparative physicochemical and technological characteristics of natural phosphates // Izvestia Est. SSR. Ser. "Chemistry, geology".– No. 1.– T. 26.– 1977.– P. 28–32.

Seitnazarov A. R., Turdialiev U. M., Namazov Sh. S., Beglov B. M., Dekhkanov Z. K., Kurbaniyazov R. K. Phosphorite flour is an acid-free form of phosphate fertilizers // Chemical Journal of Kazakhstan.– Almaty, 2017.– No. 3 (59).– P. 157–173.

Pestov N. E. Physico-chemical properties of granular and powdery chemical products.– M.: USSR Academy of Sciences, 1947.– 239 p.

Guide to practical classes on the technology of inorganic substances / M. E. Pozin, B. A. Kopylev ., E. S. Tumarkina ., G. V. Belchenko – L.: Goskhimizdat, 1963.– 376 p.

Ganikhanova F. F., Beglov V. M. Insoluble residue of phosphorites of Karatau and Uzbekistan. Proceedings. Tash PI, "Chem. and chem. Technology".1969.– Issue. 55.– P. 8–12.

Vinnik M. M., Erbanova L. N., Zaitsev P. M. and others. Methods for analyzing phosphate raw materials, phosphorus and complex fertilizers, feed phosphates.– M.: Chemistry, 1975.– 218 p.

GOST 30181.4–94. M mineral fertilizers. Method for determining the total mass fraction of nitrogen contained in complex fertilizers and nitrate in ammonium and nitrate forms (Deward method).

Galadze L. B. Development of methods for improving the quality of granules of phosphorus-containing fertilizers based on the study of physico-chemical conditions for their production: Diss. Ph.D. tech. Sci.– M.: NIUIF, 1979.– P. 65–66.

submitted 22.08.2023;
accepted for publication 20.09.2023;
published 8.10.2023

Contact: gulnor-sayler@mail.ru

The Austrian Journal of Technical and Natural Sciences, No 9–10
ISSN 2310-5607

PREMIER Publishing
ppublishing.org

Section 2. Materials Science

DOI:10.29013/AJT-23-9.10-32-36

SOLUTIONS TO LIMIT THE ABILITY TO SPREAD FLAMES ON THE SURFACE WHEN THE MATERIAL IS PLACED VERTICALLY OF WOOD MATERIALS IN VIETNAM

Nguyen Nhu Dung [1]

[1] Faculty of Fire Protection, University of Fire Protection

Cite: *Nguyen Nhu Dung. (2023). Solutions to Limit the Ability to Spread Flames on the Surface When the Material is Placed Vertically of Wood Materials in Vietnam. Austrian Journal of Technical and Natural Sciences 2023, No 9-10.* https://doi.org/10.29013/AJT-23-9.10-32-36

Abstract

The study aims to propose solutions to limit the possibility of flame propagation on the vertically placed surface of wood materials used in Vietnam. In order to come up with solutions, it is necessary to understand the factors that affect the ability to spread flame on the surface of the vertically placed wood material. Experimental methods according to ISO 5658–2:2006 are used to determine the degree of influence of each factor on the ability to spread fire, including: Humidity, material thickness and heat source capacity. The study has shown the effect of increased humidity, wood material thickness and heat source capacity on the ability to spread flames on vertically placed wood surfaces.

Keywords: *fire spread, heat source capacity, humidity, material thickness*

Introduction

Wood materials are commonly used in Vietnam due to their high aesthetics, mainly used as tiling materials or decorative partitions. Besides, the disadvantage of natural wood materials is that they are flammable, easy to spread fire on the surface of the material. The change in the characteristics of wood under fire conditions as well as fire protection measures for wood materials have been focused on research. However, studies focus mainly on issues such as the thermal decomposition process of wood under fire conditions, the fire hazard properties of wood materials such as ignition, smoke and toxin capacity, and the ability to spread flames on the surface of wood materials. The current published studies on flame propagation on the surface of wood materials mainly focus on evaluating the degree of fire propagation to classify materials according to fire hazard. Meanwhile, factors affecting the ability to spread fire on the surface of wood materials vertically under use conditions in Vietnam have not been specifically studied. The article aims to provide a method to determine the fire propagation

on the vertical surface of some popular wood materials in Vietnam, including: natural wood and MDF artificial wood. At the same time, the parameters affecting the ability to spread fire on the surface of the vertically placed material of wood materials under fire conditions are determined.

Experimentally evaluate the ability to spread flame on the surface of vertically placed materials of natural wood and MDF artificial wood

Natural and artificial wood materials are commonly used in Vietnam, when using wood materials, they also take advantage of locally available materials. Each year, planted timber provides about 25 million m^3 for the construction industry (Vu Huy Dai, Ta Thi Phuong Hoa, Vu Manh Tuong, Do Van Van, Nguyen Tu Kim, 2016). In addition, due to the gradual depletion of natural wood resources, the demand for wood products is increasing, artificial wood is a product with a rapid development rate. Commonly used artificial wood boards in Vietnam include plywood, particleboard and fiberboard (MDF wood).

The effect of moisture content, material thickness and heat source capacity on the ability to spread flame on the surface of wood material vertically is determined according to the experimental survey method based on the test procedure specified in ISO 5658–2 : : 2006. Test measurements were performed on natural and artificial wood with variations in moisture content, material thickness and heat source capacity.

Each sample group of wood materials for testing is randomly selected from natural wood in Vietnam and MDF artificial wood, including 03 samples with a width of 155 mm and a length of 800 mm, nourishing samples in room conditions to a constant volume. The test to determine the effect of the thickness of wood materials includes 03 sample nests with a thickness of 7 mm respectively; 18 mm and 25 mm. The test to determine the effect of humidity consists of 03 sample nests with humidity of 7%, 12% and 18% respectively. The test to determine the effect of the heat source capacity consists of 03 sample sets with a thickness of 18 mm, humidity of 12% tested with heat source capacity of 20 kW/m^2, 35 kW/m^2 and 50 kW/m^2.

The test procedure for determining the ability to spread fire on the surface of materials vertically complies with the procedure specified in ISO 5658–2 : 2006. The test equipment is composed of three main parts, including: an open flame heating element and thermal radiation, a sensor unit that records heat flux and a synchronous computer with the manufacturer's IMO Soft software installed. Thermal radiation heaters have adjustable radiation intensity up to approx. 62 kW/m^2, surface temperature up to approx. 750 °C.

The ability to spread fire over a material's surface vertically is classified according to the critical surface heat flux intensity (Ministry of Construction (2022). In addition, to evaluate the influence of factors on the ability to spread fire on the surface of the material vertically, the length of the burnt sample and the rate of fire propagation on the surface of the wood material in the vertical direction are also noted.

Results and discussion

The test results show that the correlation between moisture content, material thickness, heat source capacity, and ability to spread fire on the surface of the material is indicated through the critical heat flux intensity. The greater the humidity and thickness of the wood material, the increase in critical heat flux intensity corresponds to the reduced ability of fire propagation on the surface (Figure 1, 2). Conversely, the more the heat source capacity increases, the lower the critical heat flux intensity corresponding to the increased ability to spread fire on the surface (Figure 3).

Research published in Russia shows that the test results on coniferous wood are similar to the types of wood being used in Vietnam. When the moisture content of the wood is changed from 1.6 ÷ 13%, the thermal radiation intensity of the flame decreases from 29.4 ÷ ÷ 21 kW/m^2 and the flame propagation velocity decreases from 2.66 ÷ 0.91 mm/s (equivalent to a decrease of nearly 3 times) (Androsov A. S., Begishev I. R., Saleev E. P., 2007). Increased humidity, reduced heat flux intensity due to increased heat losses for heating evaporate the water contained in the wood material out of the layer the surface of the material, due to which the velocity of thermal decomposition

is reduced. In addition, water vapor in natural convection currents enters the combustion zone, reducing the temperature of the flame, the likelihood of radiation is reduced.

Figure 1. *The effect of moisture on the ability to spread flame over the surface of the material vertically (Nguyen Nhu Dung, Dinh Cong Hung (2023)*

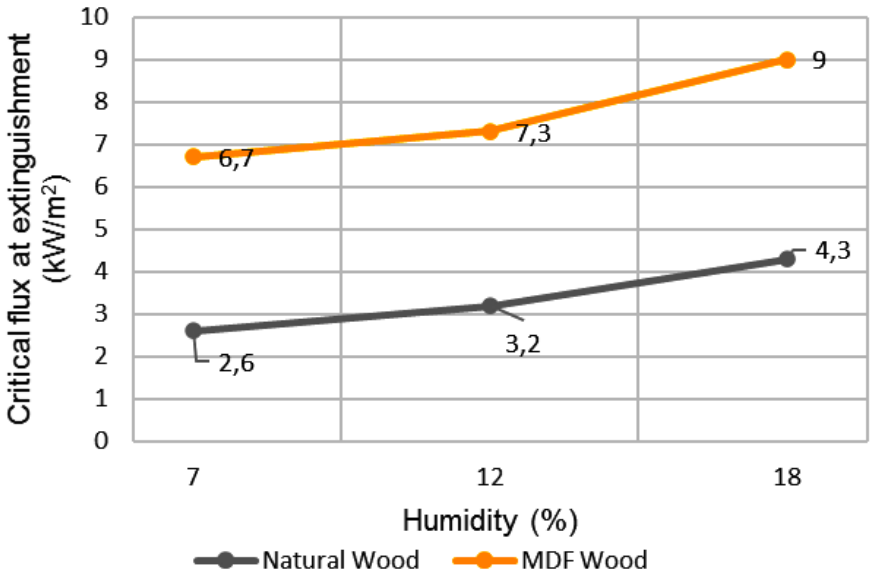

Research shows that with an increase in thickness, the rate of flame propagation decreases. As the thickness of the solid combustible substance sample increases, the flame propagation velocity decreases mainly due to the increased amount of heat and cost to heat in depth (Figure 2).

Figure 2. *The effect of material thickness on the ability to spread flame over the material surface vertically (Nguyen Nhu Dung, Dinh Cong Hung (2023)*

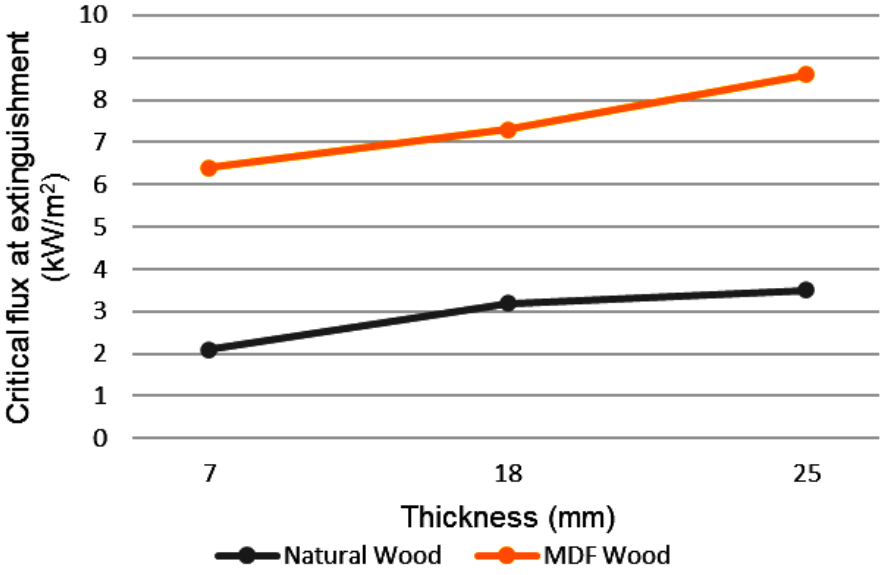

The smaller the heat source capacity, the greater the heat loss, the flame propagation rate slows down gradually, and the flame can be extinguished (Figure 3). The spread of flame on the surface of wood material follows the general law of flame propagation. In particular, the heat supply to create a fire reaction zone plays a major role. The heat to create the combustion reaction zone depends on the heat source capacity and heat loss from this zone to the outside.

Figure 3. *The effect of heat source capacity on the ability to spread flame over the material surface vertically (Nguyen Nhu Dung, Dinh Cong Hung (2023)*

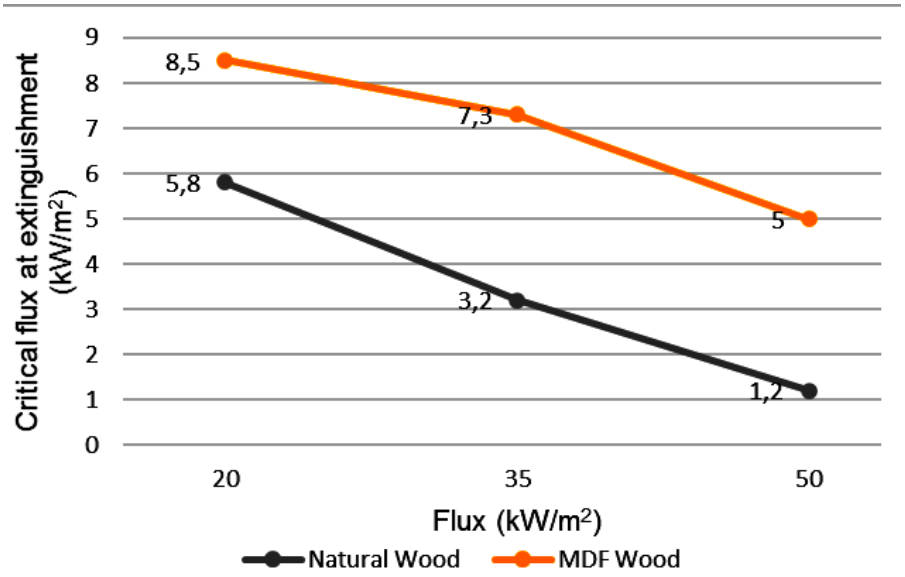

Experimental results show that moisture, material thickness and heat source capacity have a certain effect on the ability to spread flame on the surface of vertically placed materials. From there, some solutions are proposed to limit the possibility of spreading fire on the surface of vertically placed materials as follows:

— For production: To limit the possibility of spreading fire, technical measures should be taken to limit moisture changes over a wide range. Current methods include wood drying and chemical wood preservation. For wood storage, it is necessary to classify and arrange by humidity with a safe distance for fire protection (including fresh wood, dried wood). In addition to wood drying, chemical wood preservation methods can be used to limit the impact of the environment on changes in moisture content of wood materials. For wood with a thickness of less than 5 mm such as sawdust, packaging and cardboard, wood scrap needs to focus on sorting and arranging materials in a neat warehouse with moderate density and the distance between other sorting areas is large enough to prevent fire from spreading when a fire occurs. Use thermal sensors at large material storage areas to detect fire early. In addition, flame propagation decreases when the heat source capacity or ambient temperature in a fire decreases. To reduce the ambient temperature in a fire, cooling measures should be taken to reduce the ambient temperature in the fire. The main cooling measure in Vietnam is to equip automatic fire extinguishing systems. In addition, for warehouses, wood factories need to be equipped with an automatic alarm system to detect fire early when the heat source capacity is small.

— For use: Finished wood materials put into civil use have a moisture content of 8–14%. When environmental conditions change, prolonged heat, dry weather, moisture content in wood materials decreases, increases the risk of fire spread (Androsov A. S., Begishev I. R., Saleev E. P., 2007), measures must be applied to limit the risk of fire and explosion such as strict management of heat and fire sources; use ventilation, air conditioning to limit the change in humidity in wood materials ... When using finished wood materials, it is necessary to pay attention to the thickness to limit the spread of fire on the surface of the material. Materials with a thickness greater than 5mm have the ability to limit the spread of fire on the surface of the material, and the spreading flame tends to extinguish itself gradually as the thickness of the material increases.

Conclusions

The article has proposed measures to limit the spread of fire on the vertically placed surface of natural wood and MDF artificial wood according to influencing factors including: moisture content, material thickness

and heat source capacity. At the same time, the research results found that MDF materials have the ability to limit the spread of fire on the surface better than natural wood materials due to surface treatment with flame retardant materials. To limit the spread of wood materials, artificial wood materials can be used with surface treatment with a thickness of 5mm and moisture content of 12% or more.

References

Ministry of Construction (2022). National technical regulation on fire safety for houses and buildings (QCVN06:2022/BXD).

Nguyen Nhu Dung, Dinh Cong Hung (2023). *Study on parameters affecting the ability to spread fire on the vertical surface of wood materials under fire conditions,* Grassroots Topic Report, University of Fire and Fighting, Hanoi.

Vu Huy Dai, Ta Thi Phuong Hoa, Vu Manh Tuong, Do Van Van, Nguyen Tu Kim (2016). *Wood Science Textbook,* Agricultural Publishing House, Hanoi.

Androsov A. S., Begishev I. R., Saleev E. P. (2007). Teoriya goreniya i vzryva, Akademiya GPS MCHS Rossii.

submitted 22.08.2023;
accepted for publication 20.09.2023;
published 8.10.2023

Contact:

The Austrian Journal of Technical and Natural Sciences, No 9–10
ISSN 2310-5607

PREMIER Publishing
ppublishing.org

Section 3. Mechaning engeeniring

DOI:10.29013/AJT-23-9.10-37-47

LOOP CLOSURE DETECTION IN A ROBOTIC ARM USING A FORWARD DYNAMICS DATASET

John Li [1]***, Nikhil Yadav*** [2]

[1] Crescent school Toronto, Ontario, Canada

[2] Division of Computer Science, Mathematics and Science
St. John's University Queens, NY, USA

Cite: *John Li, Nikhil Yadav. (2023). Loop Closure Detection in a Robotic Arm Using a Forward Dynamics Dataset. Austrian Journal of Technical and Natural Sciences 2023, No 9-10.* https://doi.org/10.29013/AJT-23-9.10-37-47

Abstract

Loop closure detection is significant within the field of robotics due to its role in enhancing accuracy and system efficiency. This study focuses on differentiating between closed-loop and open-loop behaviors in robotic arm motion using a forward dynamics dataset. Closed-loop systems offer heightened accuracy and reliability, finding widespread utility in automotive manufacturing, while open-loop systems, characterized by distinct traits, are extensively employed in entertainment industries. Leveraging a vast dataset encompassing millions of data points covering both closed and open loop movements, this paper employs classical machine and deep learning methodologies to classify such behaviors. Using conventional machine learning models, the discriminatory power is observed to be impressive, with decision trees yielding classification accuracies and F1-scores of up to 90%. Complementing these efforts, a neural network model is employed, achieving a similar accuracy of 91%. This research not only builds upon existing work but also introduces a novel comparative framework that to the best of our knowledge has been unexplored for such a large dataset. By harnessing data generated from a 3-degree-of-freedom robotic arm, the study shows success in discerning the fundamental nature of open-loop or closed-loop configurations. This paper contributes to advancing the understanding of loop closure detection, holding implications for enhancing robotic control and performance across diverse applications.

Keywords: *Deep learning, supervised learning, prediction, classification, Machine learning, Forward Dynamics, Neural Networks, Robotics*

1. Introduction

Loop closure detection, a task central to robotic autonomy, involves the recognition of previously visited states or configurations, enabling a robot to reconcile and comprehend its position in its environment or configuration

space (Bombois et al., 2015). This capability becomes even more crucial when discussing robotic arms, devices that, by their nature, have the potential for high degrees of redundancy. Identifying and avoiding repetitive motions is critical for tasks that demand efficiency, from delicate assembly lines in industries to precise medical surgeries.

At the heart of robotic motions lies forward dynamics, an approach that predicts future states based on current conditions and inputs. Traditional systems utilizing forward dynamics alone offer foundational predictability rooted in the principles of causality and determinism, drawing from the well-established laws of physics to predict a system's trajectory based on its present state and the forces influencing it (Borovic et al., 2005). Forward dynamics involves solving equations of motion and applying Newtonian mechanics to model how forces and accelerations affect a system's movement over time, providing a deterministic link between initial conditions and future behavior. However, these traditional techniques can face challenges when confronted with intricate tasks or unexpected disruptions, prompting the integration of machine and deep learning to complement these approaches. This synergy between forward dynamics and learning techniques empowers robots to manage the complexities of real-world environments and tasks that may elude deterministic models, enabling them to possess both foundational predictability and the capacity to learn and adapt from interactions with their surroundings. As robotic arms operate within dynamic and unpredictable environments, the integration of machine and deep learning techniques provides a promising pathway to enhance adaptability and precision (Agudelo-Espana et al., 2020).

Before diving further, it's imperative to understand the difference between open-loop and closed-loop systems in robotic arms. Open-loop systems, often referred to as feed-forward systems, operate based on a predefined set of instructions without any feedback mechanism. They execute tasks without adjusting to discrepancies or environmental changes (Surati et al., 2021). In contrast, closed-loop systems, or feedback systems, constantly take input from sensors or other feedback mechanisms, adjusting their behavior based on this feedback. This inherent adaptability makes closed-loop systems more responsive to real-world dynamics (Soori et al., 2023). However, the challenge lies in determining whether a robotic arm is functioning in an open or closed-loop manner during its operations. This distinction becomes vital as closed-loop systems often require more computational resources but offer superior precision, while open-loop systems are faster but might not be as accurate in dynamic environments.

With the rise of Model Predictive Control (MPC) in robotic applications, the integration of machine learning models becomes even more compelling. MPC, at its core, is about making decisions based on predicted future states. When merged with deep learning models, as seen in innovations like Model Predictive Interaction Control (MPIC), there's an enhancement in both the accuracy of predictions and the quality of interactions between the robot and its environment (Vaisi, 2022).

Recent research also emphasizes the potential of ML and DL in predicting whether a robotic arm is operating in an open-loop or closed-loop manner. By predicting this state accurately, one can optimize the system's computational efficiency and precision, tailoring its operations based on real-time requirements (Trianni and Lopez-Lbanez, 2015). Such predictions could play a pivotal role in sectors where both speed and precision are vital, allowing robotic arms to switch between modes as required.

Furthermore, the paradigm of machine learning in robotics extends beyond mere predictive accuracy. Loop closure detection can benefit immensely from other learning paradigms such as imitation learning, where robotic arms learn from human demonstrators, and transfer learning, which allows for the transfer of knowledge across different tasks or even different robotic platforms. The integration of these methods ensures that robotic arms do not waste computational resources relearning or re-exploring configurations they've previously encountered, further enhancing efficiency (Gold et al., 2021; Mellatshahi, 2021).

In the broader perspective, the realm of loop closure detection in robotic arms stands at an intersection. On one side, we have the established foundation of forward dynam-

ics and the conventional wisdom of open vs. closed-loop systems, on the other, the rapidly evolving world of machine learning. As research progresses, it's becoming abundantly clear that the union of these domains offers a pathway to robots that are not just autonomous but also incredibly adaptive and intelligent (Liu et al., 2021).

The quest for such an integration is not just academic. As industries and medical fields become increasingly reliant on robotic arms for precision tasks, the demand for machines that can seamlessly integrate into dynamic environments, recognize their historical interactions, and adapt on-the-fly becomes paramount. This fusion of forward dynamics and machine learning, as underscored by recent research, seems poised to deliver on this front, heralding a new era in robotic arm capabilities and applications.

In this paper we look at a comprehensive forward dynamics dataset consisting of up to 9 million rows of data. To the best of our knowledge this is one of the largest such datasets on which such a study exploring the feasibility of ML and DL methods has been conducted.

The rest of the paper is organized as follows: Section 2 explains the research methodology, Section 3 discusses the obtained results from various models, and Section 4 summarizes the research conclusions.

Results

In this section, a comprehensive analysis of accuracy outcomes for the conventional models is presented, followed by a detailed examination of the top-performing Decision Tree model. Each model's performance is meticulously evaluated across diverse dataset sizes, encompassing 1 million, 1.8 million, 2.7 million, 4.5 million, 6.3 million, and 9 million instances. These insights offer a profound understanding of the models' capacities and limitations in various data contexts. This is shown in Figure 5.

The Decision Tree model emerges as a focal point, showcasing a remarkable accuracy escalation as dataset size increases. Commencing at 84% accuracy with a dataset of 1 million instances, it attains an impressive 90% accuracy with 9 million instances. This pronounced surge underscores the model's inherent ability to delineate intricate decision boundaries, effectively capturing complex relationships within data structures. The Decision Tree model adapts seamlessly to encompass a larger number of data instances, refining its predictive potential.

In tandem, the SVM model demonstrates incremental accuracy improvements with expanding dataset sizes. Progressing from 73% to 79%, its pattern of enhancement signifies SVM's proficiency in outlining intricate decision boundaries within higher-dimensional spaces. Yet, the model's scalability is challenged by computational demands posed by larger datasets.

Conversely, the Random Forest model, despite its commendable performance, does not surpass the Decision Tree model. With an accuracy of 85% on a dataset of 9 million instances, its ensemble framework efficiently addresses overfitting concerns. However, nuanced analysis reveals the Decision Tree's singular accomplishment of 90% accuracy – attributed to its remarkable ability to decipher intricate decision boundaries within the dataset.

On the other end of the spectrum, the Logistic Regression model consistently lags behind its counterparts. Starting at 77% accuracy with 1 million instances, it reaches 83% with 9 million instances. This relative underperformance arises from the model's simplicity in capturing linear relationships within data. As dataset complexity expands, the model's linear assumptions may fall short in encapsulating intricate decision boundaries, affecting its predictive efficacy.

A closer examination unveils the Logistic Regression model's vulnerability to complex data interdependencies. Reliant on linear relationships, it might struggle to navigate intricate relationships present in the dataset. Unlike the Decision Tree's ability to discern intricate boundaries, the Logistic Regression model's simplicity may under-represent non-linear patterns, particularly within larger datasets.

For the neural network, the attained accuracies at different dataset sizes are as follows: 87% for 1 million instances, 87% for 1.8 million instances, 89% for 2.7 million instances, 90% for 4.5 million instances, and 91% for both 6.3 million and 9 million instances. This sequence of accuracy values reveals a

consistent upward trajectory in performance as the dataset size increases.

The model's accuracy progression from 87% with 1 million instances to 91% with 9 million instances underscores its capability to effectively leverage larger datasets. This improvement in performance can be attributed to the neural network's inherent adaptability and capacity to capture intricate patterns present in more extensive datasets. The model's architectural flexibility enables it to discern higher-order features and relationships as the dataset expands, leading to enhanced predictive accuracy.

Figure 5. *Accuracies for all dataset sizes and models*

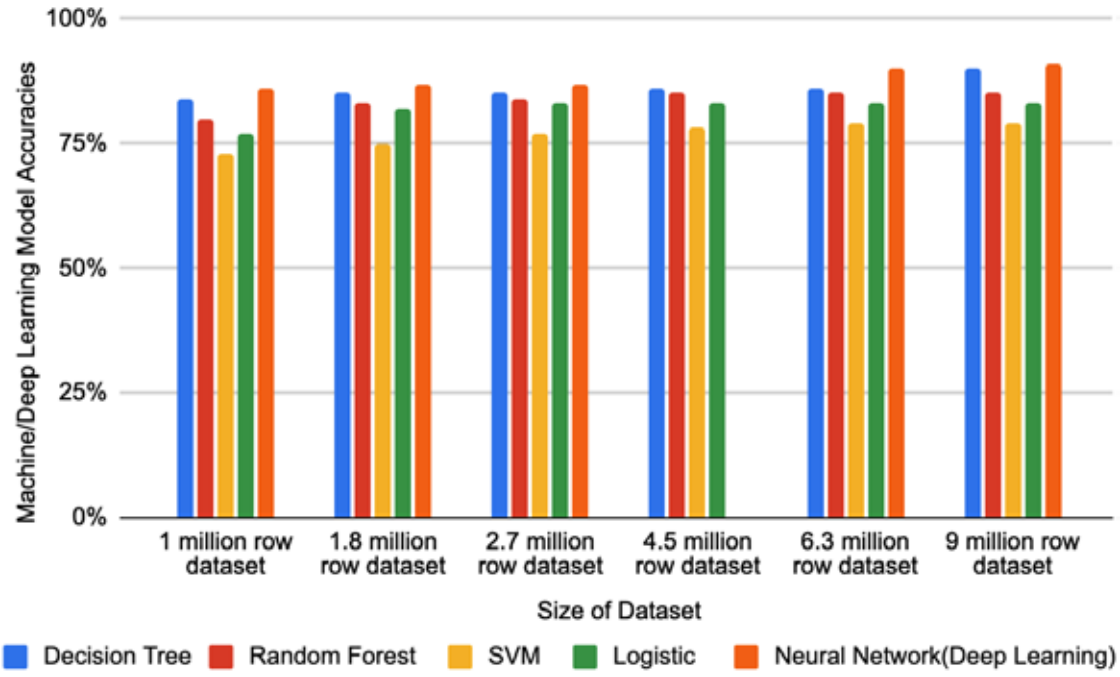

The observed correlation between dataset size and accuracy underscores the neural network's aptitude for data-driven insights. This trend of increasing accuracy with larger datasets substantiates the model's proficiency in uncovering nuanced patterns that are otherwise less discernible with smaller datasets. It reflects the model's adeptness at grasping complex data relationships and effectively leveraging them to make accurate predictions.

Discussion of Results

The comprehensive analysis of both traditional machine learning models and the advanced neural network architecture reveals discernible trends in classification and regression tasks. The Decision Tree model consistently emerges as a strong contender, exhibiting commendable accuracy across diverse dataset sizes. Its attainment of 90% accuracy underscores its significance, driven by its intrinsic capability to discern intricate decision boundaries and adapt to varying data scenarios.

On the contrary, the Support Vector Machine (SVM) model demonstrates relatively modest performance in both classification and regression tasks. The SVM's limitations in handling intricate feature interactions and its sensitivity to hyperparameters contribute to its relatively subdued accuracy. Despite these constraints, recognizing its contextual relevance remains crucial for specialized applications.

The Random Forest model stands out as a robust competitor, maintaining consistent accuracy across different dataset sizes. Its ensemble nature, harnessing multiple decision trees, reinforces predictive reliability. Meanwhile, the Logistic Regression model consistently upholds its credibility, delivering respectable accuracy across datasets of varying extents.

The pinnacle of performance is reached through the meticulously designed neural network architecture, consistently achieving an impressive 91% accuracy. This underscores the model's adaptability in capturing

intricate data patterns. The refined equilibrium achieved between model complexity and generalization, through iterative adjustments to hidden layers, serves as a foundation for consistent accuracy enhancements.

The neural network's supremacy arises from its architectural flexibility. Deep learning models, exemplified here, allow for customization of layer structures to cater to data nuances. The neural network's inherent architecture, tailored for sequential and temporal data, magnifies its predictive capabilities. Incremental training mechanisms further bolster this advantage, enabling adaptive improvements across successive epochs. The neural network's capacity to learn and retain contextual information within the dataset amplifies its proficiency in processing extensive sequences.

Methodology

The overall methodology of the paper is shown in figure 1 and is as follows: data was used from the existing dataset involving a 3 degrees of freedom DOF robotic arm (Diego, 2020); the data was preprocessed into a dataset which was used to train both a set of conventional machine learning models and a neural network. The F-1 scores and accuracies were then calculated for each model. These steps are highlighted in the subsections that follow.

Figure 1. *Flowchart of the research process*

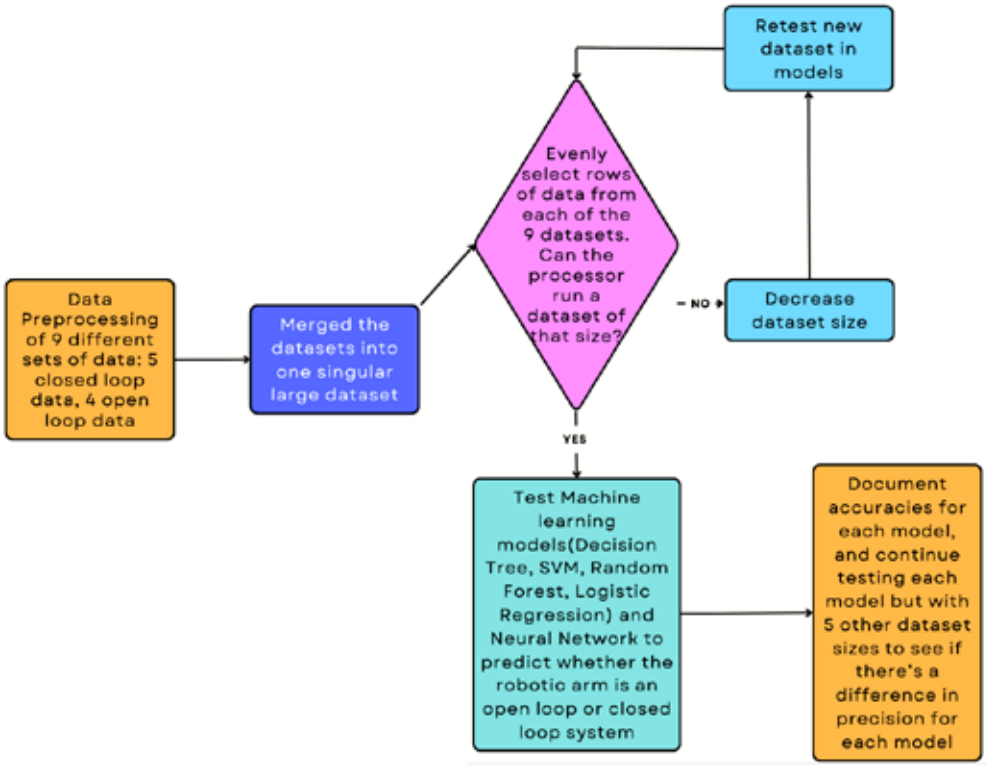

Data Preprocessing

The training data used was through a forward dynamics dataset involving a 3 DOF robotic arm; the initial dataset consists of 54 million rows of data and 3 columns. This robotic arm dataset has been tested in closed loop and open loop environments. The following data were collected for both systems: measured velocity, constrained torque, measured torque, measured angle. By combining both the data from both closed loop and open loop datasets, a merged dataset with a combination of both control systems were formed. In total there were over 54 million rows of data, out of which, the data size was reduced in quanta ranging from 1 million to 9 million data rows for feasibility of processing). This was done by randomly selecting 100000–1000 000 rows of data from each set of data.

The data contains 3 columns of numerical data, the other two columns were added simply for classification purposes during training. As shown below:

Table 1. *Table Illustration*

Sequence Rollouts	Sequence Length	Number of degrees of freedom	Classification of data	Open loop/Closed loop
–0.327145	–0.329200	–0.311136	Constrained Torques	Closed Loop
0.343809	–0.132684	0.183878	Desired Torques	Closed Loop
–0.339387	0.148001	0.344629	Measured Torque	Close loop
1.668972	1.517300	3.097472	Measured Angles	Open Loop
4.654593	0.532875	–1.17895	Measured Velocity	Open Loop

The first three columns allow the models to learn and predict whether the system is open loop or close loop. The data pertaining to "Sequence Rollouts," "Sequence Length", and the "Number of Degrees of Freedom" play a pivotal role in predicting whether a robotic arm operates within an open loop or closed loop system framework. After analyzing the dataset and comparing data from open-loop and closed-loop systems in the robotic arm, several key trends emerged. First, "Sequence Rollouts," representing predefined movements, provided insights into real-time adaptability. The "Sequence Length" played a role in indicating precision and alignment with closed-loop systems, with longer sequences favoring such systems, while shorter ones were associated with open-loop systems. Additionally, the "Number of Degrees of Freedom" influenced control complexity, with higher degrees favoring closed-loop systems, necessitating advanced control methods, while lower degrees were typical of open-loop systems.

These findings highlight the distinctions between open and closed-loop systems in the robotic arm context. The fourth column serves the purpose of classification, delineating the specific measurement category to which each corresponding row relates. These classifications encompass nine distinct types: encompassing measured velocities, measured torques, constrained torques, measured angles, measured velocities sine, measured torques sine, constrained torques sine, desired torques sine, and measured angles sine. Notably, the initial quartet pertains to open-loop data, while the latter quintet pertains to closed-loop data. The fifth column assumes the role of differentiating between the row's status as open-loop or closed-loop data. In summary, the integrated utilization of the first three columns, alongside the detailed classifications within the fourth and fifth columns, empowers the models to proficiently differentiate between open loop and closed loop systems, while also contributing to the enhanced predictive capabilities of the entire framework.

Table 2. *One-Hot Encoding for Column 4*

Column 4								
Measured Velocities	Measured Torques	Constrained Torques	Measured Angles	Measured Velocity Sine	Measured Torques Sine	Constrained Torques Sine	Measured Angles Sine	Desired Torques
1	0	0	0	0	0	0	0	0
0	1	0	0	0	0	0	0	0
0	0	1	0	0	0	0	0	0
0	0	0	1	0	0	0	0	0
0	0	0	0	1	0	0	0	0
0	0	0	0	0	1	0	0	0
0	0	0	0	0	0	1	0	0
0	0	0	0	0	0	0	1	0
0	0	0	0	0	0	0	0	1

The dataset underwent preprocessing by using one-hot encoding, leading to the creation of encoded features that captured relevant attributes. Columns 4 and 5 were one-hot encoded as shown in Tables 1 and 2. The dataset was divided, allocating 30% of the data for training and reserving the remaining 70% for comprehensive testing. Additionally, a subset of the training data was further set aside for validation purposes, enabling thorough assessment during the model training process. Data preprocessing played a pivotal role, ensuring cleanliness and outlier-free datasets. Exploratory data analysis revealed essential patterns and correlations that informed subsequent decisions.

Table 3. *One-Hot Encoding for Column 5*

Column 5	
Open Loop System	Closed Loop System
1	0
0	1

Software & Hardware Tools

Data preprocessing and model training were conducted in Python, employing core libraries including NumPy, Pandas, and scikit-learn for efficient data manipulation, scaling, and classification. The deep learning component utilized TensorFlow and Keras, encompassing diverse layers, optimizers, and callbacks. This integrated approach facilitated robust analysis and model construction.

Conventional ML Models

The four conventional machine learning models serve as a benchmark for the neural network approach. A systematic examination of conventional machine learning models was undertaken to discern the operational paradigm of the system, classifying it as open loop or closed loop based on the available data. Support Vector Machines (SVM), Decision Tree, Random Forest, and Logistic Regression were the models of choice. These models were chosen for their wide recognition and versatility in addressing classification tasks. The SVM model was instantiated with a linear kernel, enabling it to effectively draw decision boundaries between classes. In the case of the Decision Tree, its parameters were configured, notably including maximum depth and criteria for splitting, thus enhancing its discriminatory power. The Random Forest classifier consists of an ensemble of decision trees, each contributing to the overall prediction consensus, with specific emphasis on the number of trees and their maximum depth. Additionally, the Logistic Regression model, prized for its simplicity and interpretability, served as a benchmark for the subsequent analyses.

After training the models, a series of predictions was carried out on both the validation and test datasets. Rigorous assessments of model performance ensued, encompassing metrics such as accuracy and comprehensive classification reports. This multifaceted analytical progression is complemented by an iterative testing approach that encompasses dataset sizes ranging from 1 million to 9 million data points in the following quanta-1 million, 1.8 million, 2.7 million, 4.5 million, 6.3 million, and 9 million. This comprehensive experimentation strategy lays the groundwork for a subsequent in-depth exploration of a deep learning model's effectiveness when compared to the established machine learning models.

Deep Learning: Neural Networks

This research advances beyond conventional machine learning paradigms, culminating in the formulation of a sophisticated deep learning neural network model shown in Table 3. The upcoming discussion will explain how this neural network is constructed and configured, highlighting that it is more effective at making predictions than the methods used before it.

In pursuit of optimizing the neural network's performance, a methodical approach was undertaken. The process commenced with a rigorous exploration of the model's architecture, involving variations in the number of layers, units per layer, and activation functions. This iterative refinement enabled

the model to strike an equilibrium between complexity and predictive efficacy. Activation functions were meticulously evaluated, initially employing Leaky Re LU and subsequently scrutinizing Re LU and Mish for potential accuracy enhancements. Overfitting was meticulously addressed through the introduction of L2 regularization and dropout techniques, with careful adjustments made to regularization strength. The strategic placement of batch normalization within the model aimed at maximizing training stability and convergence.

Table 3. *Neural Network details*

Optimization	Details
Data Loading	Loading data from the merged dataset
Target Label Encoding	Encoded target labels 'Column5' and 'Column4' using LabelEncoder ('le5' and 'le4)
Data Splitting	Split data into training and testing sets (X_train, X_test, y_train, y_test).
Data Standardization	Standardized features using Standard Scaler (scaler).
Neural Network Model	Constructed a Sequential model (model) with multiple layers.
Model Architecture	– Input Layer: 256 neurons, normal initialization, L2 regularization (0.01), Leaky Re LU activation, batch normalization, dropout (40% rate). – Hidden Layers: Depths of 128, 64, 32, and 16 neutrons with Leaky Re LU activation, batch normalization, and dropout (40% rate). – Output Layer: Single neuron, sigmoid activation function.
Model Compilation	Compiled the model with Adam optimizer (learning rate: 0.0005), binary cross-entropy loss, and accuracy metric.
Callbacks	Defined Early Stopping (patience: 15 epochs) and Reduce LROn Plateau (factor: 0.1, patience: 7) callbacks for training optimization.
Training	Trained the model with batch size of 32, 150 epochs, sample weights computed using "balanced" strategy, and callbacks (early_stopping and reduce_lr).
Model evaluation	Evaluated the model's performance on the test dataset using classification_report from sklearn.metrics.

Hyperparameter tuning played a pivotal role, with systematic adjustments to the learning rate, batch size, and epoch count for optimized convergence behavior. Diverse optimization algorithms, including Adam and RMSProp, were exhaustively investigated for their potential to improve model convergence. The integration of early stopping and learning rate reduction strategies was instrumental in averting overfitting and enhancing training efficiency. Feature engineering enriched the model's predictive capability by introducing novel information. An exhaustive hyperparameter tuning process, encompassing grid search and random search methodologies, meticulously fine-tuned the model's configuration.

The iterative refinement process, guided by continuous evaluation on both validation and test datasets, culminated in a well-calibrated neural network architecture. At its core, this architecture adheres to the sequential model structure intrinsic to deep learning frameworks. It harmoniously combines organized layers with efficient data flow, expediting the intricate process of feature learning. The model, calibrated to utilize the Adam optimizer with a learning rate of 0.001, adeptly minimizes binary cross-entropy loss

while meticulously tracking accuracy during 150 training epochs with a batch size of 32. Addressing class imbalance, sample weights were calculated using the 'balanced' strategy. The reinforcement of training was further bolstered by callback mechanisms, including early stopping and learning rate reduction, promoting timely convergence and principled adaptation. Model evaluation rigorously adhered to academic standards, with the 'classification_report' function employed to substantiate the model's prowess across various class delineations through precision, recall, F1-score, and support metrics.

In conclusion, this deep learning neural network is characterized by tested heightened accuracy and resilience.

F1 Scores

The models were each compared using the F1 scores they obtained on the validation data. For binary classification problems, the F1 score is calculated by this equation (Kundu, 2022).

$$\text{F1 Score} = 2 * ((\text{Precision} * \text{Recall})/ /(\text{Precision} + \text{Recall}))$$

Precision is the ratio of the number of true positives to the sum of true positive and false positives. The precision in F1 Score shows how close the measured values are to each other. Recall is the comparison of true positives to the sum of true positive and false negatives like precision but they represent the model's ability to find the relevant cases in a dataset.

This equation serves as a crucial measure of the models' performance, encapsulating the balance between the precision of positive predictions and the recall of relevant instances. A higher F1 score indicates a more favorable trade-off between precision and recall, signifying a model that excels at both accurate identification of positive instances and comprehensive coverage of relevant cases.

In the context of this study's multi-class classification problem, the comparative analysis of the models employed a micro-averaged F1 score. This selection ensured equitable consideration of every data entry within the dataset, an imperative choice given the balanced nature of the classes, which stemmed from the application of percentile-based thresholds. The decision to adopt the micro-averaged F1 score was grounded in the alignment of class distribution and the objective of maintaining balance across classes.

The rationale behind choosing the F1 score as the benchmark for model comparison lies in its capacity to provide an impartial assessment. Through its incorporation, the study gained the ability to objectively evaluate the models, a crucial aspect in the pursuit of discerning the model's efficacy. Moreover, the F1 score offers a unique vantage point by simultaneously acknowledging periods of elevated case counts and striking a harmonious equilibrium between accuracy and recall.

Conclusion

This paper has delved into the intricate realm of loop closure detection within the domain of robotic arm motion. The ability to differentiate between closed-loop and open-loop behaviors holds significant implications for enhancing accuracy and efficiency in robotic systems. This research has harnessed a vast forward dynamics dataset encompassing over 1 million data points, focusing on classifying these behaviors using both classical and deep learning methodologies.

Looking ahead, this study opens the door to numerous avenues for future research. The integration of other learning paradigms, such as imitation learning and transfer learning, could further enhance the adaptability and efficiency of robotic arms. Exploring the potential of reinforcement learning and model predictive control can augment the accuracy and interactions of robotic systems. Moreover, investigations into hardware improvements, including faster processors, could significantly expedite training times and broaden the scope of research.

The significance of this study lies not only in its contributions to loop closure detection but also in its broader implications for robotics. As industries increasingly rely on robotic arms for precision tasks, the ability to seamlessly integrate these systems into dynamic environments becomes paramount. The fusion of traditional forward dynamics with modern machine learning paves the way for adaptable, intelligent, and autonomous robotic arms that can navigate complex scenarios with efficiency and precision.

In summary, this research extends the boundaries of loop closure detection, pre-

senting a comparative framework that bridges classical approaches and cutting-edge deep learning techniques. By shedding light on the fundamental nature of closed-loop and open-loop behaviors in robotic arm motion, this study advances the understanding of robotic control and performance, with implications for diverse applications across industries and fields.

References

Bombois, X., Anderson, B., and Scorletti G. "Open-loop vs. closed-loop identification of box-jenkins systems in a ..." ANU Research Publications. March, 2015. Available at: URL: https://openresearch-repository.anu.edu.au/handle/1885/39591/ URL: https://openresearch-repository.anu.edu.au/handle/1885/39591

Borovic, B., Liu, A., Popa, D., Cai, H., and Lewis, F.L. "Open-loop versus closed-loop control of MEMS devices: Choices And Issues". Journal of Micromechanics and Microengineering. October 2005. Available at: URL: https://www.researchgate.net/publication/228388708_Open-loop_versus_closed-loop_control_of_MEMS_devices_Choices_and_issues/ URL: https://www.researchgate.net/publication/228388708_Open-loop_versus_closed-loop_control_of_MEMS_devices_Choices_and_issues

Agudelo-Espana, D., Zadaianchuk, A., Wenk, P., Garg, A., Akpo, J., Felix Grimminger, J., Naveau, M., Righetti, L., Martius, G., Krause, A., Scholkopf, B., Bauer, S. and Wuthrich, M. "A real-robot dataset for assessing transferability of learned dynamics". 2020. IEEE International Conference on Robotics and Automation (ICRA). 2020. Available at: URL: https://is.mpg.de/uploads_file/attachment/attachment/589/ICRA20_1157_FI.pdf/ URL: https://is.mpg.de/uploads_file/attachment/attachment/589/ICRA20_1157_FI.pdf

Surati, S., Hedaoo, S., Rotti, T. and Ahuja, V. "Pick and place robotic arm: A Review Paper". IRJET. February 2021. Available at: URL: https://www.irjet.net/archives/V8/i2/IRJET-V8I2311.pdf/ URL: https://www.irjet.net/archives/V8/i2/IRJET-V8I2311.pdf

Soori, M., Arezoo, B., and Dastres, R. "Artificial Intelligence, Machine Learning and deep learning in advanced robotics, a review". Cognitive Robotics. April 6, 2023. Available at: URL: https://www.sciencedirect.com/science/article/pii/S2667241323000113/ URL: https://www.sciencedirect.com/science/article/pii/S2667241323000113

Vaisi, B. "A review of optimization models and applications in robotic manufacturing systems: Industry 4.0 and Beyond". Decision Analytics Journal. February 17, 2022. Available at: URL: https://www.sciencedirect.com/science/article/pii/S2772662222000054/ URL: https://www.sciencedirect.com/science/article/pii/S2772662222000054

Trianni, V.and López-Ibáñez, M. "Advantages of task-specific multi-objective optimisation in Evolutionary Robotics". PloS One. August 21, 2015. Available at: URL: https://www.ncbi.nlm.nih.gov/pmc/articles/PMC4546428/ URL: https://www.ncbi.nlm.nih.gov/pmc/articles/PMC4546428/

Gold, T., Volz, A. and Raichen, K. "Model predictive interaction control for industrial robots". IFAC-PapersOnLine. April 14, 2021. Available at: URL: https://www.sciencedirect.com/science/article/pii/S2405896320334583/ URL: https://www.sciencedirect.com/science/article/pii/S2405896320334583

Mellatshahi, S.N. "Learning Control of Robotic Arm Using Deep Q-Neural Network". Scholarship at UWindsor. March 10, 2021. Available at: URL: https://scholar.uwindsor.ca/cgi/viewcontent.cgi?article=9573&context=etd/ URL: https://scholar.uwindsor.ca/cgi/viewcontent.cgi?article=9573&context=etd

Liu, R., Nageotte, F., Zanne, P., Mathelin, M.D. and Dresp-Langley, B. "Deep reinforcement learning for the control of robotic manipulation: A ..." Arxiv. 2021. Available at: URL: https://arxiv.org/pdf/2102.04148/ URL: https://arxiv.org/pdf/2102.04148)

Diego. "RR-learning/transferable_dynamics_dataset: Datasets and code to evaluate transferability of dynamics learning methods" rr-learning. 2020. Available at: URL: https://github.

com/rr-learning/transferable_dynamics_dataset/ URL: https://github.com/rr-learning/transferable_dynamics_dataset
Kundu, R. “F1 score in Machine Learning: Intro & Calculation”.– Vol. 7. December 16, 2022. Available at: URL: https://www.v7labs.com/blog/f1-score-guide/ URL: https://www.v7labs.com/blog/f1-score-guide)

submitted 22.08.2023;
accepted for publication 20.09.2023;
published 8.10.2023

Contact: johnli31@crescentschool.org; yadavn@stjohns.edu

The Austrian Journal of Technical and Natural Sciences, No 9–10
ISSN 2310-5607

PREMIER Publishing
ppublishing.org

Section 4. Phisics

DOI:10.29013/AJT-23-9.10-48-51

A BRIEF REVIEW OF NCT DOSIMETRY

Himmatov I.F.[1], Ulin S.E.[2]

[1] Samarkand State University named after Sharof Rashidov University, Samarkand, Uzbekistan

[2] National Research Nuclear University MEPhI (Moscow Engineering Physics Institute), Moscow, Russian Federation

Cite: *Himmatov I.F., Ulin S.E. (2023). A brief review of NCT dosimetry. Austrian Journal of Technical and Natural Sciences 2023, No 9-10.* https://doi.org/10.29013/AJT-23-9.10-48-51

Abstract

Neutron Capture Therapy (NCT) offers a targeted approach for treating tumors, but its clinical implementation faces challenges in accurate dosimetry. This review focuses on the complexities of measuring the four key absorbed dose components — Photon, Hydrogen, Nitrogen, and Boron doses — in NCT treatments. Emphasis is placed on the importance of measuring the Boron dose, owing to boron-10's high interaction rate with thermal neutrons. While various methods, including gamma spectroscopy, are explored, they present logistical and safety challenges. The High-Pressure Xenon Gamma-ray Spectrometer emerges as a hopeful tool due to its high energy resolution and resilience against neutron flux. This study underscores the need for further research to standardize NCT dosimetry.

Keywords: *Neutron Capture Therapy (NCT); Dosimetry; Boron Dose Measurement; Gamma Spectroscopy; High-Pressure Xenon Gamma-ray Spectrometer; Thermal Neutrons*

Introduction

Shortly after the discovery of neutrons, Chadwick proposed Neutron Capture Therapy (NCT) in 1932. Goldhaber, in 1934, emphasized the significance of the naturally occurring boron-10 isotope's exceptional thermal neutron capture cross-section. NCT exploits the formation of secondary radiation when thermal and epithermal neutrons are absorbed by certain elemental nuclei. When tumor cells selectively accumulate elements like boron-10, lithium-6, cadmium-110, and gadolinium-157 and are subsequently irradiated with neutrons, the resulting radiation can damage these tumor cells with minimal impact on adjacent tissues (Beckman, I.N.).

Neutrons interact minimally with regular tissue; their primary interactions are nuclear captures with stable nuclei like ^{1}H, ^{14}N, and ^{10}B. Although living tissues are rich in ^{1}H (0.33 barns) and ^{14}N (1.7 barns), their capture cross-sections are so small that lethal

radiation damage is infrequent. Conversely, while ^{10}B (3990 barns) is scarcely found in living tissues, its neutron interaction rate is exceptionally high.

Upon neutron absorption, ^{10}B transforms into the excited nucleus of ^{11}B, which rapidly decays (10^{-12} seconds) into an α-particle and the ^{7}Li nucleus. In 6% of cases, their total energy is 2.8 MeV, and in 94% it's 2.3 MeV, since 0.48 MeV is carried away by a γ-quantum. These highly energized particles lose energy swiftly, and since a typical cell size is about 10μm, a significant portion of the energy is deposited directly into the cell housing the captured neutron (Taskaev, S.Y., Kanygin, V.V., 2016).

For NCT's clinical implementation, three key challenges must be addressed: sourcing neutrons suitable for clinical settings, selectively delivering boron to tumor cells, and ensuring accurate dosimetry throughout treatment. This review delves into the last challenge, focusing on NCT dose determination.

NCT absorbed dose measurement

Thermal neutral beams used in NCT yields four principal absorbed dose components in the treated tissue:

1. Photon dose (D_γ)
2. Hydrogen dose (D_h)
3. Nitrogen dose (D_N)
4. Boron dose (D_B)

Several methods have been introduced to measure these doses, including:

1. Ion chamber measurements;
2. Micro dosimetry measurements;
3. Gel dosimetry evaluations.

Despite the presence of multiple measurement methods, there is still no universally accepted standard for NCT dosimetry. Importantly, the first three radiation types — photon, hydrogen, and nitrogen — have a relatively minor impact on living tissue. As a result, the central emphasis in NCT dosimetry is on measuring the boron dose.

Among the available methods, gamma spectroscopy stands out as the only technique capable of directly measuring the absorbed boron dose. This method relies on the detection of a 478 keV gamma-ray, emitted during the rapid decay of a boron nucleus after capturing a neutron. However, implementing gamma spectroscopy in NCT presents several challenges:

1. The equipment for registering gamma quanta must be positioned near the patient during neutron irradiation, posing logistical and safety concerns.

2. The proximity of the neutron beam formation system — which consists of a moderator, a reflector, and an absorber — to the patient restricts the available space for placing the gamma spectroscopy equipment.

3. The detectors pick up not only the desired signals from boron decay but also spurious signals from other gamma quanta and neutrons, complicating the data analysis.

Given these constraints, the practical application of gamma spectroscopy in NCT dosimetry seems limited, underscoring the need for continued research to establish more feasible and accurate dosimetry methods.

Materials and Methods

1. Considering these constraints, utilizing a gamma spectrometer with high energy resolution becomes paramount. The "High Pressure Xenon Gamma-ray Spectrometers" developed by the National Research Nuclear University MEPHI meets these criteria. The spectrometer boasts a 2% energy resolution for a 662 keV γ-ray, notably superior to NaI or CsI-based scintillation gamma detectors. This xenon-based spectrometer can measure γ-rays in an energy spectrum from 0.05 to 3 MeV (Alexander, S., Novikov, Sergey, E., Ulin, Valery, Dmitrenko, V., Chernysheva, Irina V., Grachev, Victor M., Krivova, Kira V., Shustov, Alexander E., Uteshev, Ziyaetdin M., Vlasik, Konstantin F. (2019); Gary, C., Tepper, Robert L., Palmer, Jon R. Losee, (1999); Ulin, S.E., Dmitrenko, V.V., Grachev, V.M. et al., (1995); Ulin, S., Novikov, A.V., Dmitrenko, K., Vlasik, K., Krivova, D., Petrenko, Z., Uteshev, A., Shustov and Petkovich, E. (2016); P'ya, S.N., Vlasik, K.F., Grachev, V.M., Dmitrenko, V.V., Novikov, A.S., Petrenko, D.V., Shustov, A.E., Uteshev, Z.M., Ulin, S.E. and Chernysheva, I.V. (2014).

The Xenon Gamma Spectrometer (XGS) is designed as a cylindrical pulsed ionization chamber equipped with a screen grid. This chamber is filled with a compressed gas mixture of xenon (Xe) and hydrogen (H_2), pressurized to approximately 40 atm. The inclu-

sion of hydrogen aims to enhance the electron drift velocity. Essentially, the XGS operates as a pulsed ionization chamber filled with high-purity, high-pressure xenon. Notably, the spectrometer is stable under radiation exposure and retains its functional properties even when subjected to a stream of neutrons. A schematic illustrating a cylindrical modification of this device, which incorporates a Frisch grid, is presented in Figure 1.

Figure 1. *The principal schematic of the xenon gamma-ray spectrometer:1 — Cylindrical pulse ionization chamber; 2 — Frisch grid; 3 — hermetic casing; 4 — anode; 5 — ceramic feed-through; 6, 8 –custom charge-sensitive amplifier; 7 — custom high-voltage supply*

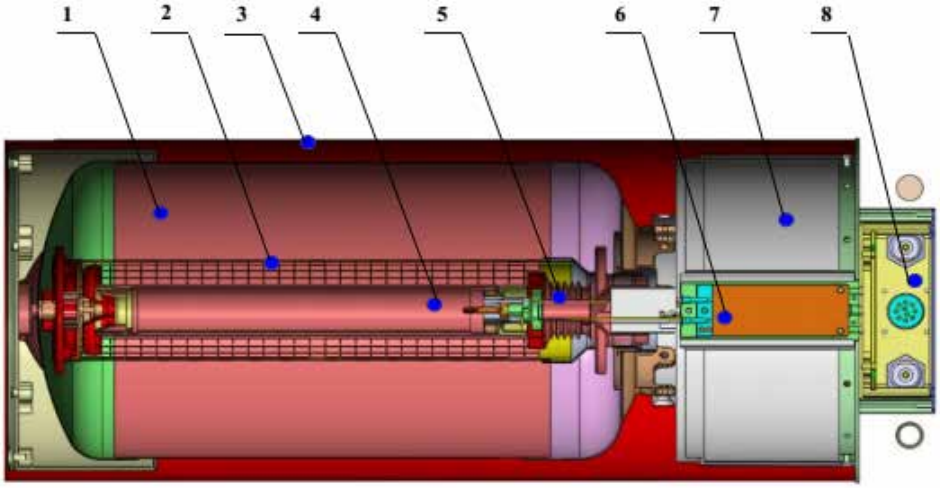

The High-Pressure Xenon Gamma-ray Spectrometer presents a distinct advantage over traditional scintillation gamma-ray spectrometers due to its resilience against neutron flux.

Spectra from High Pressure Xenon Detector (ø120 mm, L=500 mm, M= 1.8kg) before and after activation by Pu-Be neutron source (T=66 hours, fluence= 1.5*10 ^{10} neutrons)

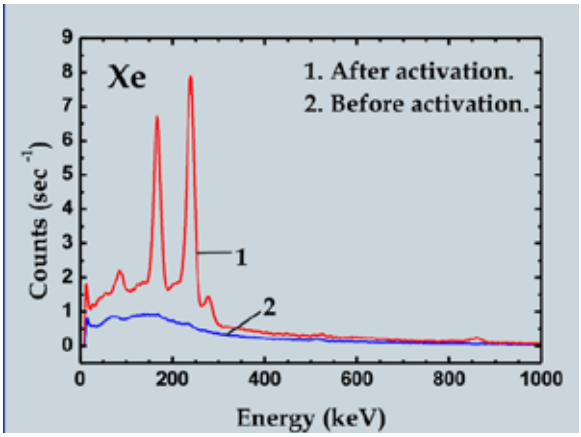

Spectra from NaI detector (ø 80 mm, L = 50 mm, M = 0.9 kg) before and after activation by Pu-Be neutron source (T = 66 hours, fluence = 1.5*10 ^{10} neutrons)

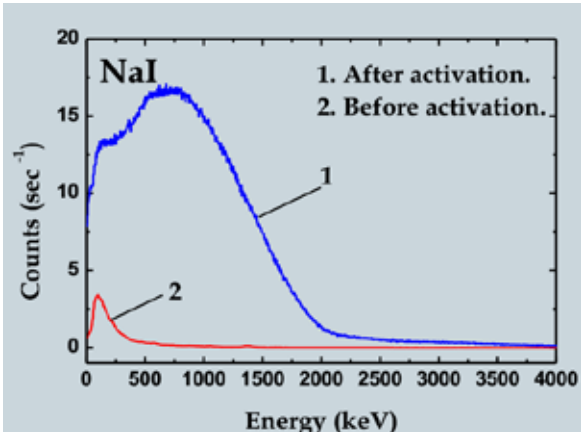

Conclusion

The xenon gamma spectrometer has great energy resolution, can be made to any size, and is resistant to neutron flux. This characteristics make it viable for in-situ measurements during NCT sessions.

References

Beckman I. N. Course of lectures. Lecture 7 “Nuclear medicine”.
Taskaev, S. Y., Kanygin, V. V. (2016). Boron-neutron capture therapy. Novosibirsk. SB RAS Publishing House.
Alexander, S., Novikov, Sergey, E., Ulin, Valery, Dmitrenko, V., Chernysheva, Irina V., Grachev, Victor M., Krivova, Kira V., Shustov, Alexander E., Uteshev, Ziyaetdin M., Vlasik, Konstantin F. (2019). “Xenon gamma-ray spectrometers: development and applications”. Proc. SPIE11114, Hard XRay, Gamma-Ray, and Neutron Detector Physics XXI, 111140H
Gary, C., Tepper, Robert L., Palmer, Jon R. Losee, (1999). “High-pressure xenon gamma-ray spectrometers: recent developments and applications”. Proc. SPIE3768, Hard X-Ray, Gamma-Ray, and Neutron Detector Physics.
Ulin, S. E., Dmitrenko, V. V., Grachev, V. M. et al. (1995). “A Cylindrical Ionization Chamber with a Shielding Mesh Filled with Xenon under a Pressure of 50 atm”. Instruments and Experimental Techniques — 38.— P. 326–330.
Ulin, S., Novikov, A. V., Dmitrenko, K., Vlasik, K., Krivova, D., Petrenko, Z., Uteshev, A., Shustov and Petkovich, E. (2016). Xenon gamma-ray spectrometer for radioactive waste controlling complex. Journal of Physics: Conference Series 675042023. Doi:10.1088/1742–6596/675/4/042023
P’ya, S. N., Vlasik, K. F., Grachev, V. M., Dmitrenko, V. V., Novikov, A. S., Petrenko, D. V., Shustov, A. E., Uteshev, Z. M., Ulin, S. E. and Chernysheva, I. V. (2014). Simulation of the Xenon Gamma Spectrometer for Analyzing Radioactive Materials — Vol. 41.— No. 9.

submitted 22.08.2023;
accepted for publication 20.09.2023;
published 8.10.2023

Contact: islombekhimmatov24@gmail.com

The Austrian Journal of Technical and Natural Sciences, No 9–10
ISSN 2310-5607

PREMIER Publishing
ppublishing.org

DOI:10.29013/AJT-23-9.10-52-56

ENERGY STATES OF CURRENT CARRIERS IN MULTILAYER SEMICONDUCTOR STRUCTURES. WENTZEL-KRAMERS-BRILLOUIN APPROXIMATION

Voxob Rustamovich Rasulov[1], Rustam Yavkachovich Rasulov[1], Islombek Arabboyevich Muminov[1], Mahliyo Adhamovna Mamatova[1], Umida Mamirjonovna Isomaddinova[2]

[1] Department Physics, Fergana State University, Uzbekistan

[2] Department Physics, Kokand State Pedagogical Institute, Uzbekistan

Cite: *Voxob Rustamovich Rasulov, Rustam Yavkachovich Rasulov, Islombek Arabboyevich Muminov, Mahliyo Adhamovna Mamatova, Umida Mamirjonovna Isomaddinova. (2023). Energy States of Current Carriers in Multilayer Semiconductor Structures. Wentzel-Kramers-Brillouin Approximation. Austrian Journal of Technical and Natural Sciences 2023, No 9-10.* https://doi.org/10.29013/AJT-23-9.10-52-56

Abstract. States of electrons in multilayer semiconductor structures are theoretically investigated in the semiclassical approximation, where one-electron wave functions of the stationary Schrödinger equation are calculated in the presence of various types of potential, which is a slowly varying function of the coordinate.

It is determined that the energy spectrum of electrons in the potential in the quadratic, cubic and biquadratic approximation takes discrete values and the steepness of the energy spectrum depends on the parameters of the expansion of the potential in coordinates.

Keywords: *energy spectrum, multilayer structure, Schrödinger equation, size quantization, semiclassical approximation*

Introduction

The progress of modern microelectronics is largely determined by the study of the properties of systems with inhomogeneously distributed parameters, the development of methods for the effective theoretical analysis of such systems, the development and provision of objective methods for controlling technological processes that make it possible to create semiconductor layers with desired properties (Shchuka A.A., 2007; Usanov, D.A. 2013). In this regard, below we consider the general questions of the propagation of electron waves in a medium whose properties change only along a certain direction. The approach is based on the use of the one-electron stationary Schrödinger equation to describe the processes of elastic scattering and tunneling of noninteracting spinless particles under the condition that their total energy is conserved.

The study of the electronic properties of both symmetric and asymmetric with respect to the geometric dimensions of the layers of

a semiconductor structure is relevant in connection with the use of these structures in micro- or nanoelectronics and in other areas of solid state physics (Dragunov, 2006; Ivchenko, 2005; Rasulov, 2018; Petrov, 1994; Rasulov, 2020; Golub, 1995; Rasulov, 2020).

At present, molecular beam epitaxy and other methods of modern technology make it possible to obtain semiconductor layers with an arbitrary profile of composition change (structure with a quantum well) to improve the characteristics of devices based on them (Usanov, D. A., 2013). In this case, the problem of electronic states is reduced to the problem of the behavior of a particle in potential wells of an arbitrary shape. In particular, to create a new generation of resonant tunneling diodes and heterolasers with separated electronic and optical confinement, structures with rectangular size-quantized wells are used, in the center of which there is an additional energy dip.

The study of the electronic states in the structures mentioned above leads to the calculation of the one-electron wave functions of the stationary Schrödinger equation in the semiclassical approximation in the presence of the potential *U(x)*, which we will consider as a slowly varying function of the x coordinate.

Basic relationships

Then the one-dimensional Schrödinger equation can be written as

$$-\frac{\hbar^2}{2m}\frac{d^2\psi}{dx^2}+U(x)\psi=E\psi, \qquad (1)$$

where, making the substitution $\psi(x)=$ $=\exp\left(iS(x)/\hbar\right)$, we obtain the equation for the function $S(x)$

$$\frac{1}{2m}\left(\frac{dS(x)}{dx}\right)^2-\frac{i\hbar}{2m}\left(\frac{d^2S(x)}{dx^2}\right)=E-U(x). \qquad (2)$$

Assuming that the system under consideration is close to the classical one in its properties, we will look for a solution in the form of a rows indegrees of the Planck constant, i.e.

$$S(x)=S_0(x)+\frac{\hbar}{i}S_1(x)+\left(\frac{\hbar}{i}\right)^2S_2(x)+\ldots \qquad (3)$$

Then the general solution of equation (1) has the form

$$\psi(x)=\frac{C_1}{\sqrt{p(x)}}\exp\left(\frac{i}{\hbar}\int p(x)dx\right)+ \\ +\frac{C_2}{\sqrt{p(x)}}\exp\left(-\frac{i}{\hbar}\int p(x)dx\right), \qquad (4)$$

where $p(x)=\left[2m\left(E-U(x)\right)\right]^{1/2}$, m and E are the effective mass and energy of current carriers.

In classically inaccessible energy regions, i.e. at, the momentum of the current carriers becomes imaginary. Then in these regions (4) takes the form

$$\psi(x)=\frac{C_1}{\sqrt{|p(x)|}}\exp\left(\frac{1}{\hbar}\int|p(x)|dx\right)+ \\ +\frac{C_2}{\sqrt{|p(x)|}}\exp\left(-\frac{1}{\hbar}\int|p(x)|dx\right) \qquad (5)$$

Note that the accuracy of the semiclassical approximation does not allow taking into account both terms simultaneously, and therefore, in some cases, we will not take into account the exponentially small term in (4) and (5).

Linear and quadratic approximation

Let us consider an isolated classical turning point at $x=a$, far from which the semiclassical approximation is applicable for calculating the transparency coefficient of a potential barrier. Therefore, the solutions of the Schrödenger equation in the allowed and forbidden areas can be found by formulas (4) – (5).

The wave function near the turning point can be found by solving the Schrödinger equation, where the potential energy *U(x)* near the turning point $(x=a)$ can be represented as

$$U(x)\simeq U(x=a)+ \\ +\left.\frac{dU}{dx}\right|_{x=a}(x-a)+\frac{1}{2}\left.\frac{\partial^2U}{\partial x^2}\right|_{x=a}(x-a)^2 \qquad (6\,a)$$

or

$$U(x)\simeq U(\varsigma=0)+U'_{\varsigma=0}\varsigma+U''_{\varsigma=0}\varsigma^2. \qquad (6\,b)$$

Then the Schrödinger equation can be written as

$$\frac{d^2\psi}{d\varsigma^2}+\frac{1}{E_a}\left(E-U_0-U'_{\varsigma=0}\varsigma-U''_{\varsigma=0}\varsigma^2\right)\psi=0, \text{ or}$$

$$\frac{d^2\psi}{d\varsigma^2}+\left(k_0-k_0\varsigma-k_2\varsigma^2\right)\psi=0, \qquad (7)$$

whose general solution is an arbitrary linear combination of hypergeometric functions, i.e.

$$\psi(\varsigma)=C_1\cdot{}_1F_1\left[\left(\frac{1}{4}-\frac{k_1^2}{16k_2^{3/2}}-\frac{k_0}{4k_2^{1/2}}\right),\frac{1}{2},\frac{\left(2k_2\varsigma+k_1\right)^2}{4k_2^{3/2}}\right]\exp\left[-\frac{\varsigma\left(2k_2\varsigma+k_1\right)}{2\sqrt{k_2}}\right]+$$

$$+C_2\cdot{}_1F_1\left[\left(\frac{3}{4}-\frac{k_1^2}{16k_2^{3/2}}-\frac{k_0}{4k_2^{1/2}}\right),\frac{3}{2},\frac{\left(2k_2\varsigma+k_1\right)^2}{4k_2^{3/2}}\right]\left(2k_2\varsigma+k_1\right)\exp\left[-\frac{\varsigma\left(2k_2\varsigma+k_1\right)}{2\sqrt{k_2}}\right], \qquad (8)$$

where $\varsigma=\frac{x-a}{a}$, $E_a=\frac{\hbar^2}{2ma^2}$,

$$k_1=\frac{1}{E_a}U'_{\varsigma=0}=\frac{1}{E_a}\frac{\partial U(\varsigma)}{\partial\varsigma}\bigg|_{\varsigma=0},$$

$$k_2=\frac{1}{E_a}U''_{x=a}=\frac{1}{E_a}\frac{\partial^2U(\varsigma)}{\partial\varsigma^2}\bigg|_{\varsigma=0},$$

$$k_0^2=\frac{2m}{\hbar^2a^2}\left(E-U(x=0)\right).$$

In the general case,

$${}_1F_1\left[\left(\frac{1}{4}-\frac{k_1^2}{16k_2^{3/2}}-\frac{k_0}{4k_2^{1/2}}\right),\frac{1}{2},\frac{\left(2k_2\varsigma+k_1\right)^2}{4k_2^{3/2}}\right]\propto$$

$$\propto\exp\left[\frac{\left(2k_2\varsigma+k_1\right)^2}{4k_2^{3/2}}\right],$$ which corresponds to an exponentially growing wave function. Therefore, to choose a wave function that satisfies the conditions of finiteness of the wave functions at infinity, i.e. satisfying this quantum mechanical approach, there are two alternative cases:

1. $C_1\neq0$, $C_2=0$ and $\frac{1}{4}-\frac{k_1^2}{16k_2^{3/2}}-\frac{k_0}{4k_2^{1/2}}=$ $=-4n$. In this case, the wave function takes the form

$$\psi_{2n}(\varsigma)={}_1F_1\left[-n,\frac{1}{2},\frac{\left(2k_2\varsigma+k_1\right)^2}{4k_2^{3/2}}\right]^{-\frac{\varsigma\left(2k_2\varsigma+k_1\right)}{2\sqrt{k_2}}}, \qquad (9)$$

and the energy spectrum of current carriers is quantized and is defined as

$$k_0=(1+16n)k_2^{1/2}-\frac{k_1^2}{4k_2^{1/2}}. \qquad (10)$$

From (10) we obtain an expression for the size-quantized energy spectrum in the form

$$E=U(x=0)+\frac{\hbar^2}{2m}k_2\left[(1+16n)-\frac{k_1^2}{4k_2}\right]^2$$

or

$$E_1-U(x=0)=$$

$$=U''_{\varsigma=0}\left[(1+16n)-\frac{1}{4E_a}\frac{\left(U'_{\varsigma=0}\right)^2}{U''_{\varsigma=0}}\right]^2. \qquad (11)$$

2. $C_2\neq0$, $C_1=0$ and $\frac{3}{4}-\frac{k_1^2}{16k_2^{3/2}}-\frac{k_0}{4k_2^{1/2}}=$ $\frac{3}{4}-\frac{k_1^2}{16k_2^{3/2}}-\frac{k_0}{4k_2^{1/2}}=-2(2n+1)$. In this case, the wave function takes the form

$$\psi_{2n+1}(\varsigma)=k_1F_1\left[-n,\frac{3}{2},\frac{\left(2k_2\varsigma+k_1\right)^2}{4k_2^{3/2}}\right]\times$$

$$\times\left(2k_2\varsigma+k_1\right)^{-\frac{\varsigma\left(2k_2\varsigma+k_1\right)}{2\sqrt{k_2}}}, \qquad (12)$$

and the energy spectrum of current carriers is quantized and is determined by the relation:

$$E_2-U(x=0)=$$

$$=U''_{\varsigma=0}\left[(11+16n)-\frac{1}{4E_a}\frac{\left(U'_{\varsigma=0}\right)^2}{U''_{\varsigma=0}}\right]^2. \qquad (13)$$

For a quantitative analysis of the size-quantized energy spectrum, we assume that $U''_{\varsigma=0}=\xi_U\cdot U'_{\varsigma=0}$. Then we have an expression for the size-quantized energy spectrum in a form convenient for quantitative calculation

$$\frac{E_2-U(x=0)}{\xi_U\cdot U''_{\varsigma=0}}=\left[(1+16n)-\frac{1}{4}x\right]^2, \qquad (14)$$

where $x=\frac{U'_{\varsigma=0}}{E_a\xi_U}$, $\xi_U=U''_{\varsigma=0}/U'_{\varsigma=0}$

Similarly, it is easy to obtain the following expression

$$\frac{E_2-U(x=0)}{\xi_U\cdot U'_{\varsigma=0}}=\left[\left(11+16n\right)-\frac{1}{4}x\right]^2 \quad .(15)$$

It can be seen from formulas (11) and (13) that to fulfill the condition of finiteness of the wave functions at infinity, there are two types of energy spectrum, and both depend nonlinearly on the size quantization number, i.e. the dimensionally quantized energy spectrum is not equidistant.

Figure 1 *a* and *b* shows the dependences of the size-quantized energy spectra, characterized by the values of $\frac{E_1(n)-U(x=0)}{\xi_U\cdot U'_{\varsigma=0}}$ and $\frac{E_2(n)-U(x=0)}{\xi_U\cdot U'_{\varsigma=0}}$, on the parameter $x=\frac{U'_{\varsigma=0}}{E_a\xi_U}$.

It can be seen from these figures that as $x=\frac{U'_{\varsigma=0}}{E_a\xi_U}$ increases, the values of $\frac{E_1(n)-U(x=0)}{\xi_U\cdot U'_{\varsigma=0}}$ and $\frac{E_2(n)-U(x=0)}{\xi_U\cdot U'_{\varsigma=0}}$ decrease from $n=2,3,....$ These energy values from $n=1$ with the growth of $x=\frac{U'_{\varsigma=0}}{E_a\xi_U}$ first decreases and is reached to a minimum, and then increases.

We note here that in quantitative calculations it is convenient to use the connection of the above hypergeometric functions with Hermite polynomials:

$$H_{2n}\left(\zeta^2\right)=(-1)^n\frac{(2n)!}{n!}\cdot{}_1F_1\left(-n,\frac{1}{2},\zeta^2\right),$$

$$H_{2n+1}\left(\zeta^2\right)=(-1)^n\frac{(2n+1)!}{n!}2\cdot$$

$$\cdot\zeta\cdot{}_1F_1\left(-n,\frac{3}{2},\zeta^2\right).$$

Figure 1. *Dependences of the energy quantities*

a) b)

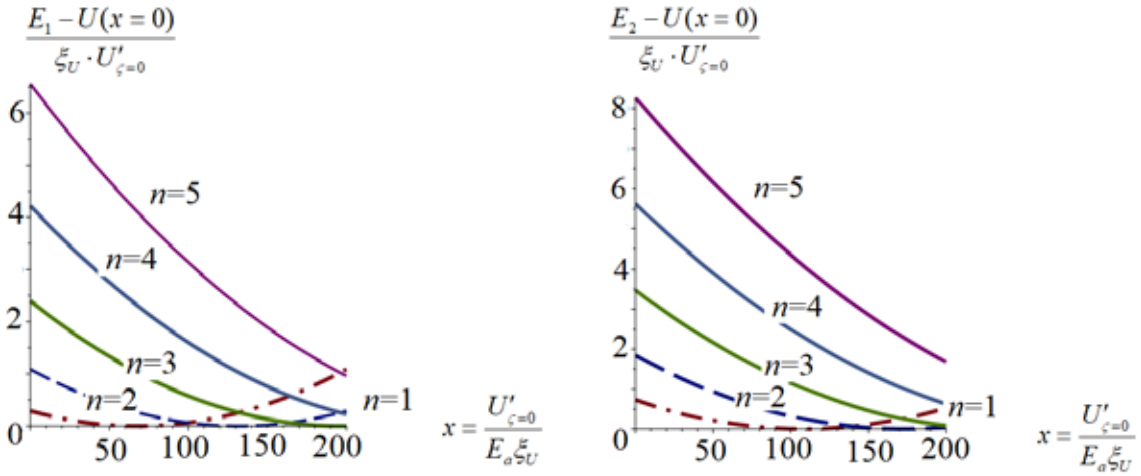

$\frac{E_1(n)-U(x=0)}{\xi_U\cdot U'_{\varsigma=0}}$ and $\frac{E_2(n)-U(x=0)}{\xi_U\cdot U'_{\varsigma=0}}$

on $x=\frac{U'_{\varsigma=0}}{E_a\xi_U}$ for different values of the size quantization number, where $\xi_U=U''_{\varsigma=0}/U'_{\varsigma=0}$

Conclusion

Next, consider the following cubic and biquadratic terms in (6), i.e.

$$U(x)=\frac{1}{2}m\omega^2x^2+\varepsilon_3\left(x/l\right)^3+\varepsilon_4\left(x/l\right)^4, \quad (16)$$

where $l=\sqrt{\hbar/(m\omega)}$. ε_3 and ε_4 are the expansion coefficients of $U(x)$ in a series of x/l. The solution of the Schrödinger equation can be done in a similar way. In this case, it passes into the Schrödenger equation for a harmonic oscillator at $\varepsilon_3=0$ and $\varepsilon_4=0$. Then it can be solved using perturbation theory (Landau, 1981). In this case, the energy of particles in

potential (16) in the zeroth approximation is equal to the energy of a harmonic oscillator:

$$E_n^0 = \hbar\omega\left(n+1/2\right), \quad (17)$$

and the wave function in the zero approximation has the form

$$u_n^0(x) = \left(2^n n! l\sqrt{\pi}\right)^{-1/2} e^{-1/2\xi^2} H_n(\xi), \quad (18)$$

$\xi = x/l$.

Then the calculation of the energy spectrum of electrons according to the perturbation theory gives the following result

$$E(k_\alpha, n) = E(k_\alpha) + \\ + \frac{1}{8}\hbar\omega\left\{\left(n+1/2\right) - 30\kappa^2\left(n^2+n+11/30\right) + \right. \\ + 6g\kappa\left(2n^2+2n+1\right) - \\ \left. - g^2\kappa^2\left(34n^3+51n^2+59n+21\right)\right\}, \quad (19)$$

where $\kappa = \varepsilon_1/(\hbar\omega)$, m is the effective electron mass, the Ox axis is chosen as the size quantization axis, $g = \varepsilon_2/\varepsilon_1$, in the spherical approximation in the $E(k_\alpha) = \hbar^2\left(k_y^2+k_z^2\right)/\left/\left(2\cdot m\right)\right.$energy spectrum. Calculations show that the energy spectrum of electrons in potential (16) takes discrete values and the steepness of the energy spectrum is more noticeable, the greater $g = \varepsilon_2/\varepsilon_1$, and it also decreases with increasing $\varepsilon_1/(\hbar\omega)$ for arbitrary values of n.

References

Dragunov, V. P., Neizvestnyi, I. G., & Gridchin, V. A. (2006). Fundamentals of nanoelectronics. Logos,– Moscow.– 496 p.

Golub, L. E., Ivchenko, E. L., Rasulov, R. Ya. (1995). Absorption of light by holes in quantum wells. *Fizika i tekhniuka poluprovodnikov*.– Vol. 29.– P. 1093–1099. (In Russian).

Ivchenko, E. L. (2005). Optical spectroscopy of semiconductor nanostructures // E. L. Ivchenko.– Harrow (UK): Alpha Science,– 350 p.

Landau, L. D. and Lifshitz, E. M. (1981). Quantum Mechanics (3rd ed.). Elsevier Science.– 689 p. URL: https://www.perlego.com/book/1834474/quantum mechanics-pdf/ (Original work published 1981).

Petrov, A. G., Shik, A. A. (1994). Absorption of light by holes in quantum wells. *Fizika i tekhniuka poluprovodnikov*.– Vol. 28.– P. 2185–2191. (In Russian).

Rasulov, R. Y., Rasulov, V. R., Mamadalieva, N. Z., & Sultanov, R. R. (2020). Subbarrier and Overbarrier Electron Transfer through Multilayer Semiconductor Structures. *Russian Physics Journal*.– 63(4).– P. 537–546.

Rasulov, R. Ya., Rasulov, V. R., Eshboltaev, I., Mamadalieva, N. S. (2018). Absorption of linearly polarized radiation in a dimensionally quantized well. *Uzbek Physics Journal*: – Vol. 20.– No. 3.– P. 361–365. (In Russian).

Rasulov, V. R., Rasulov, P. Y., Eshboltaev, I. M., & Sultonov, R. R. (2020). Dimensionally Quantization in n-GaP. *Semiconductors*.– Vol. 54(4).– P. 429–432. URL: https://doi.org/10.1134/S1063782620040132

Shchuka, A. A. (2007). Nanoelectronics.– M., Fizmatkniga.– 465 p. (in Russian).

Usanov, D. A. (2013). Physical foundations of nanoelectronics. Saratov: Saratov State University.– 162 p.

submitted 22.08.2023;
accepted for publication 20.09.2023;
published 8.10.2023

Contact:

The Austrian Journal of Technical and Natural Sciences, No 9–10
ISSN 2310-5607

PREMIER Publishing
ppublishing.org

Section 5. Technical Science in general

DOI:10.29013/AJT-23-9.10-57-60

DEVELOPMENT AND RESEARCH OF AN INVERTER BASED ON INJECTION – VOLTAIC ELEMENTS

Alimova Nodira Batirdjanovna [1]

[1] DSc in Technics, Professor, Department of Mechatronics and robotics, Tashkent State Technical University, Uzbekistan

Cite: *Alimova N.B. (2023). Development and Research of an Inverter Based on Injection - Voltaic Elements. Austrian Journal of Technical and Natural Sciences 2023, No 9-10.* https://doi.org/10.29013/AJT-23-9.10-57-60

Abstract

The article explores the possibility of using the injection-voltaic mode of operation of a bipolar transistor to create electronic switching cells (electronic keys) – the basis of digital electronic elements operating at a supply voltage of the order of the contact potential difference.

Keywords: *photo-voltaic effect, injection-voltaic effect, bipolar transistor, microelectronics, integrated circuit, inverter*

Introduction

Microelectronics is one of the fastest growing areas of science and technology. The technical characteristics of microelectronic products – integrated circuits (ICs) – are constantly being improved and the functionality expanded. Improvements in microcircuits are achieved through advances in technology, circuit design, and system organization of integrated circuits.

ICs are the elemental base of radio engineering devices. Research and practical implementation of technological ideas to reduce its dimensions, weight, energy consumption, material consumption, and cost, increase the volume of functions performed, etc. continue at a tremendous pace.

The design process for ultra-large ICs can be divided into electrical and physical design. Electrical design includes functional design, logic design, circuit design, and semiconductor design. Physical design includes the topology of ultra-large ICs, i.e. placement of semiconductor devices, routing, etc.

However, the basis for both electrical and physical design of ultra-large ICs is semiconductor device design. Since the design of semiconductor devices is carried out in conjunction with the development of corresponding technological processes, this means that the design of semiconductor devices is the basis of ultra-large ICs machine design.

Since the main element of the IC are bipolar transistors, on their basis it is possible

to create a number of traditional functional devices that are widely used in practice.

Solution

In recent years, studies have been carried out on the photovoltaic effect of solar radiation electrical conversion devices (Alimova, N. B., 2008). Some aspects of the operation of diodes, transistors and other devices as nonlinear elements were also studied. However, the area of research where both of these aspects are taken into account in the interrelation is practically unexplored in their mutual influence, although one should expect the manifestation of physical phenomena that determine new properties of semiconductor devices developed on the basis of this approach.

The injection-voltaic effect in bipolar transistors and thyristor structures was theoretically predicted and experimentally discovered. The injection-voltaic effect is observed in transistor and thyristor structures with p-n junctions upon injection of current carriers from one forward-biased p-n junction to another and consists in generating voltage in it (Fig. 1. a). The magnitude of the injection-voltaic voltage and current depends on the value of the load resistance Rload. By varying the values of the load resistance Rload from zero to infinity, it is possible to obtain the load characteristic of the structure in the injection-voltaic mode (Fig. 1. b).

At $R_{load} = 0$ voltage $U_{load} = 0$ and $I_{load} =$ Iing. As R_{load} increases to certain values, the p-n junction current will remain practically constant (Fig. 1.b, curve 1), and the forward voltage at the collector junction will increase. At a sufficiently large value of R_{load} ($R_{load}=\infty$), the injection current of the collector junction will be equal to zero (Fig. 1.b). At this value $U_{load} = U_{iv.emf}$ and it approximately corresponds to the value of U_{st}. In this case, the voltage between the emitter and collector is zero. And the transistor can be considered as a closed electronic switch with a dynamic resistance of the order of zero.

Figure 1. *Injection-voltaic effect in transistor structures (a) and its current-voltage characteristic (CVC) (b)*

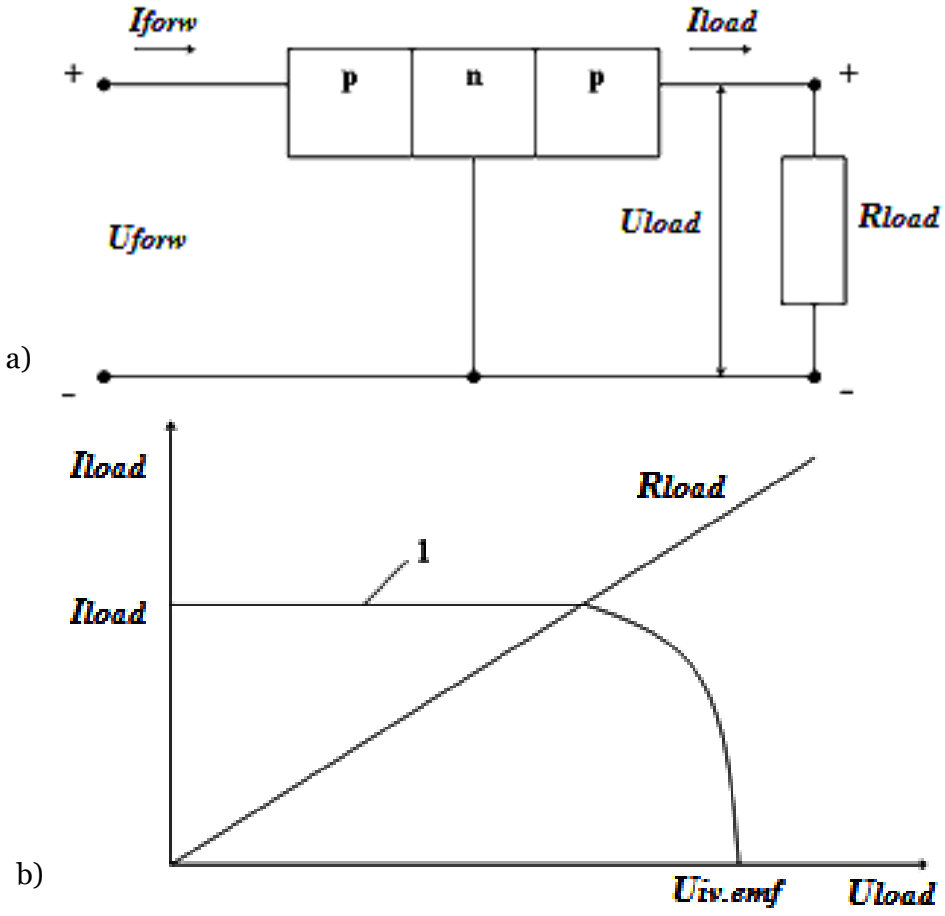

These properties can be used in the synthesis of inverters based on bipolar transistors operating at a supply voltage value of the order of the contact potential difference (Aripov, K.K., Alimova, N.B., Bustanov, Kh. Kh., Ob'edkov, E.V. and Toshmatov, Sh.T., 2009; Alimova, N.B., 2009; Aripov, Kh.K., Alimova, N.B., 2013; Alimova, N.B., 2019). An inverter based on complementary bipolar transistors (CBT) can be used in discrete and integrated circuit technology, information and telecommunication systems.

Inverters based on bipolar transistors are known. The main disadvantages of inverters are low speed, bulkiness, high power consumption during switching and high supply voltage. In addition, the inverter contains a high-resistance resistor, which is difficult to implement technologically in an IC. The complexity of implementing high-resistance resistors forces a separate resistor to be placed next to the IC, disrupts the temperature conditions of the IC, and reduces the degree of integration of the IC.

You can reduce the power consumption during switching and reduce the supply voltage.The proposed connection of two different types of multicollector transistors makes it possible to reduce the current consumption and the supply voltage due to the simultaneous use of cutoff and saturation modes in bipolar transistors.

If a signal corresponding to logical "1" is supplied to the input of the inverter CBT, equal in value to the voltage of the power supple (+V), then the emitter-base voltage of the n-p-n multi-collector transistor is equal to the value of V, and the emitter-base voltage of the p-n-p transistor is zero. In this case, the n-p-n transistor operates in saturation mode, and the p-n-p transistor operates in cut-off mode. In cut-off mode, the resistance between the collector-emitter electrodes is very high (practically determined by the leakage current of the collector junction), and the collector-emitter voltage of the n-p-n transistor is close to zero.

Figure 2. *Electrical circuit of the CBT inverter (a), transfer amplitude characteristic of the CBT inverter (b)*

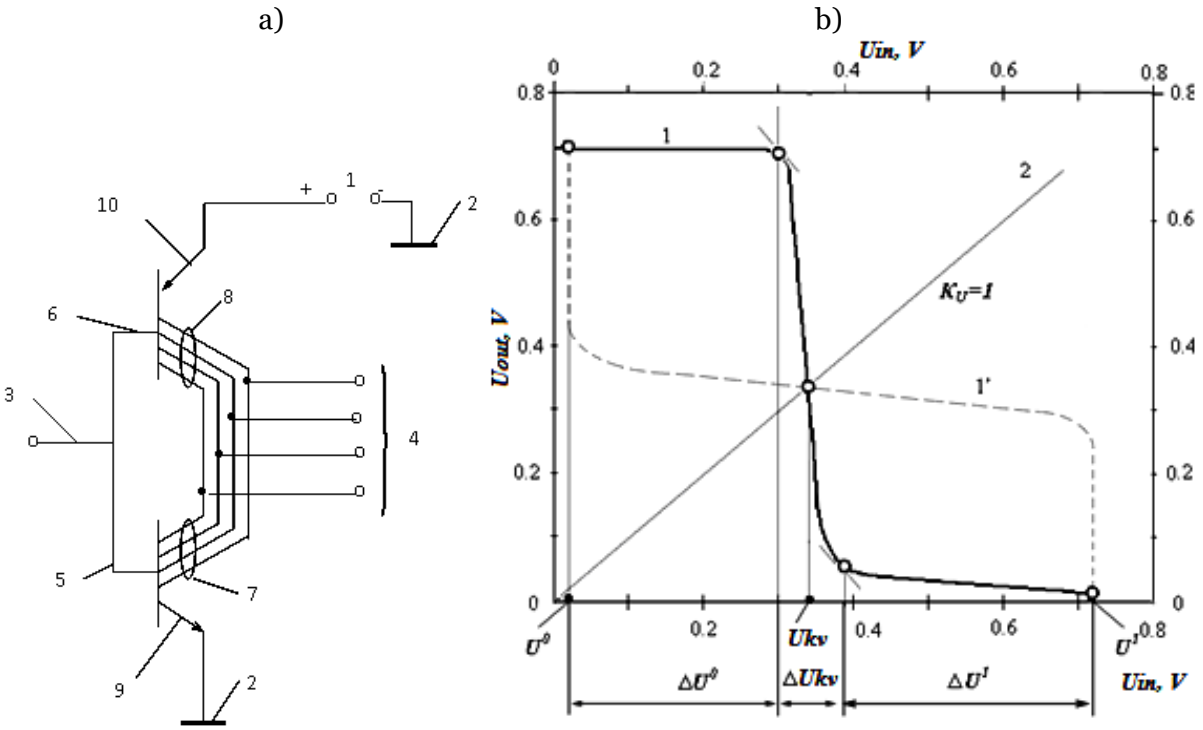

In (Fig. 2, a) the electrical circuit of the CBT inverter is shown. Multicollector n-p-n and p-n-p transistors are designated VT1 and VT2, respectively. The numbers indicate: 1-power supply V; 2-common bus; 3-inverter input; 4-inverter output; 5,6-base, 7,8-collector, 9,10-emitter electrodes of transistors.

In (Fig. 2, b) shows the transfer characteristic of the inverter on the CBT. The CBT inverter has a transfer characteristic

symmetrical with respect to *V*, quantization voltage $U_{kv} = V/2$, practically the same noise immunity for logical states, and a sharp transition front from one stable state to another stable state.

The CBT inverter is a basic cell for synthesizing AND-NOT, NOR-NOT logic elements with an arbitrary set of inputs and outputs, and other digital devices. In addition, the inverter can be widely used in telemetry systems, automation, industrial and automotive electronics.

Conclusion

The injection-voltaic effect in multilayer semiconductor structures was discovered and studied.

A new basic cell of digital ICs has been proposed in terms of circuit design – an inverter based on complementary bipolar transistors (CBTs), operating at supply voltages (*V*) limited by the natural limit of the *V* on the order of the contact potential difference in the p-n junction. Thus, $V \sim 1.2\ V$ for BT made from GaAs, $V \sim 0.8\ V$ for BT made from Si, and V ~ 0.4 V for BT made from Ge. The proposed inverter based on the KBT using the injection-voltaic effect has been studied from the theoretical and experimental sides. The inverter was made on the basis of bipolar transistors of the KT315 and KT361 types. It has been established that the inverter has a symmetrical transfer characteristic with the parameters: $U_{=}^{1} = 0.710$ V, $U_{=}^{0} = 0.02$ V, $U_{kv} = 0.34$ V, $\triangle U_{=}^{1} = 0.32$ B, $\triangle U_{=}^{0} = 0.28$ V for V = 0.71 V.

The CBT inverter based on bipolar transistors can be used in digital ICs and large ICs, as well as in digital technology as the basic elements of “NOT”, “OR-NOT”, “AND-NOT” circuits, etc.

References

Alimova, N. B. (2008). Elements base based on Injection – Voltaic Effect // TUIT Bulletin.– Tashkent,– № 4.– P. 82–84. (05.00.00; 31). [in Russian].

Alimova, N. B. (2008). New Injection – Voltaic Effect Elementary Basis // The 9th International Conference on Electronics, Information and Communication.– Tashkent, 2008.– P. 520–523.

Aripov, K. K., Alimova, N. B., Bustanov, Kh. Kh., Ob'edkov, E. V. and Toshmatov, Sh. T. (2009). Adapted Electronic Switching Cell with Power Supple from Solar Cell // Applied Solar Energy Allerton Press, Inc. 2010.– Vol. 45.– № 2.– P. 9–13. (05.00.00; № 1).

Alimova, N. B. (2009). Study of the Injection – Voltaic Effect in multilayer p-b structures // TUIT Bulletin.– Tashkent,– № 4.– P. 84–85. (05.00.00; 31). [in Russian].

Aripov, Kh. K., Alimova, N. B. (2013). Low-voltage base elements of the digital schemes // Info communications: Networks-Techlogies-Solutions.– Tashkent,– № 3(27).– P. 12–16. (05.00.00; № 2). [in Russian].

Alimova, N. B. (2019). Principles and methods for constructing radio technical elements, assemblies and devices based on photo- and injection-voltaic effects. The Doctoral dissertation of Technical Sciences (DSc).– 176 p. [in Uzbek].

submitted 22.08.2023;
accepted for publication 20.09.2023;
published 8.10.2023

Contact: nali71@yandex.ru

The Austrian Journal of Technical and Natural Sciences, No 9–10
ISSN 2310-5607

PREMIER Publishing
ppublishing.org

DOI:10.29013/AJT-23-9.10-61-66

X-RAY PHASE ANALYSIS OF COMPLEX MINERAL FERTILIZERS BASED ON GLAUCONITE SAND AND WITH SOME MINERAL FERTILIZERS

Allaniyazov Davran Orazimbetovich [1], ***Erkaev Aktam Ulashevich*** [2]

[1] Karakalpak Research Institute of Natural Sciences of the Karakalpak Branch of the Academy of Sciences RUz, Nukus

[2] Department of Chemical Technology of Inorganic Substances Tashkent Institute of Chemical Technology

Cite: *Allaniyazov D.O., Erkaev A.U. (2023). X-Ray Phase Analysis of Complex Mineral Fertilizers Based on Glauconite Sand and With Some Mineral Fertilizers. Austrian Journal of Technical and Natural Sciences 2023, No 9-10.* https://doi.org/10.29013/AJT-23-9.10-61-66

Abstract

The work studied the physicochemical characteristics of the raw materials used – glauconite sand and jelvak phosphorites of Karakalpakstan. The process of preparing complex glauconite-containing fertilizers based on glauconite, Karakalpakstan and fertilizing salts was investigated. The possibility of obtaining complex glauconite-containing fertilizers based on glauconite, nitrogen and potassium fertilizers is shown. Diffractograms of binary mixtures of glauconite sands with ammonium nitrate, ammonium sulfate, potassium chloride, carbamide, ammophos and phosphorite flour are also given.

Keywords: *Karakalpakstan, Krantau, glauconite, glauconite sands, X-ray phase analysis, mineral fertilizers*

Introduction

The main task of modern agriculture is to obtain high-quality yields while increasing soil fertility, which is impossible without the use of fertilizers. Mineral fertilizers are one of the sources of additional nutrition of plants (Artyushin, A.M., Derzhavin L.M., 1984).

However, in modern conditions, the salinity and degradation of the soils of the sown areas of the republic are manifested on an increasing scale. This applies to the northern regions of the republic, especially the Republic of Karakalpakstan, where approximately 80% of irrigated arable land is subject to various degrees of salinity and degradation (Environmental problems of Uzbekistan, 2011).

Based on the above, along with the need to develop effective soil brining measures, a promising direction is the creation of trace elements containing fertilizers with complex-forming, ion-exchange and sorption properties that would help plants grow on saline soils. Complex fertilizers produced on the basis of glauconite of the Republic of Karakalpakstan in the presence of fertilizing salts possess such properties

(Allaniyazov, D.O., 2019; Allaniyazov, D.O., Erkaev, A.U. 2021; Allaniyazov, D.O., Erkayev, A.U., Tajibayev, T.A., Ochilov, S.U., 2023).

Objects and methods of research:

The object of research in this work are glauconite sands Krantau, Phosphorite flour of the Khudjakul deposit of Karakalpakstan and standard mineral fertilizers produced in Uzbekistan, ammonium nitrate, ammonium sulfate, potassium chloride, urea, ammophos and phosphate flour.

Research material and methodology:

Based on the above, in the laboratory conditions we decided to test the possibility of obtaining complex glauconite fertilizers using mineral salts based on their granulation. First, granular mineral fertilizers were ground in a porcelain mortar to a powdery state. Obtained powders are mixed till homogeneous mass with enriched glauconite sands at various mass ratios of glauconite: potassium chloride, ammonium nitrate, ammonium sulfate, carbamide and moistened to 7–16.6% of total mass and supplied to granulator. At the same time, microelement-containing granules were formed, in appearance similar to granules of standard fertilizers produced at factories.

Identification of the samples was carried out on the basis of diffractograms taken on a computer-controlled XRD-6100 apparatus (Shimadzu, Japan). Radiation-CuKa (β filter, Ni, 1.54178 tube current and voltage mode 30 mA, kV) and constant detector rotation speed 4 deg/min, in 0.02 deg increments, (ω/20 coupling) were used, and the scanning angle varied from 4 to 80 °, the scanning angle during diffractometric studies varied from 2 to 80 °. Qualitative and quantitative identification of the phases of the presented samples was carried out using the MATCH! ® Phase identification from Powder Diffraction program (Crystal Impact, GbR, Bonn, Germany, 2015) (MATCH!® Phase identification from Powder Diffraction 2015; Döbelin, N., Kleeberg, R. 2015).

Research results:

The production of complex mineral fertilizers based on glauconite and widely used mineral fertilizers was continued. Figure 1–10 shows diffractograms of binary mixtures of glauconite sands with ammonium nitrate, ammonium sulfate, potassium chloride, carbamide, ammophos and phosphorite flour. When taking diffraction patterns, the same conditions were observed, and the sample weights were approximately equal. Glauconite sands produced on an industrial scale need to be enriched because they need to have a percentage of glauconite of at least 50% in order to be used as mineral fertilizers. In the samples studied, this percentage is no more than 30% (Drits, V.A., Zviagina, B.B., McCarty, D.K., Salyn, A.L., 2019).

Figure 1. *Diffractograms of glauconite: saltpeter mixtures in different ratios: 1) saltpeter; 2) 5:45; 3) 15:35; 4) 45:5*

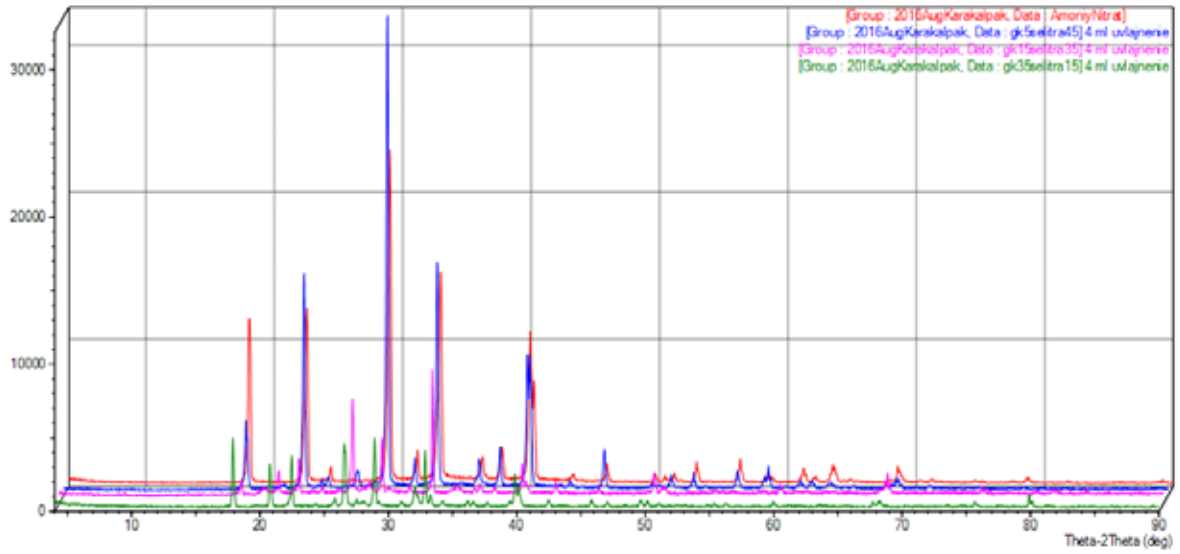

Figure 2. *Diffractograms of mixtures of glauconite: ammonium sulfate in different ratios: 1) ammonium sulfate; 2) 5:45; 3) 15:35; 4) 45:5*

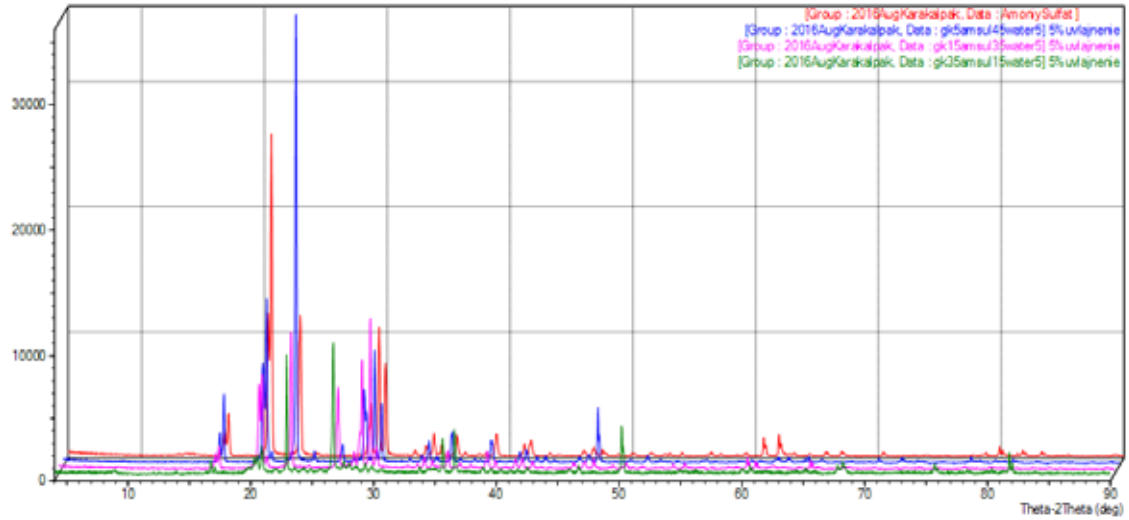

Figure 3. *Diffractograms of glauconite mixtures: potassium chloride in different ratios: 1) potassium chloride; 2) 5:45; 3) 15:35; 4) 45:5*

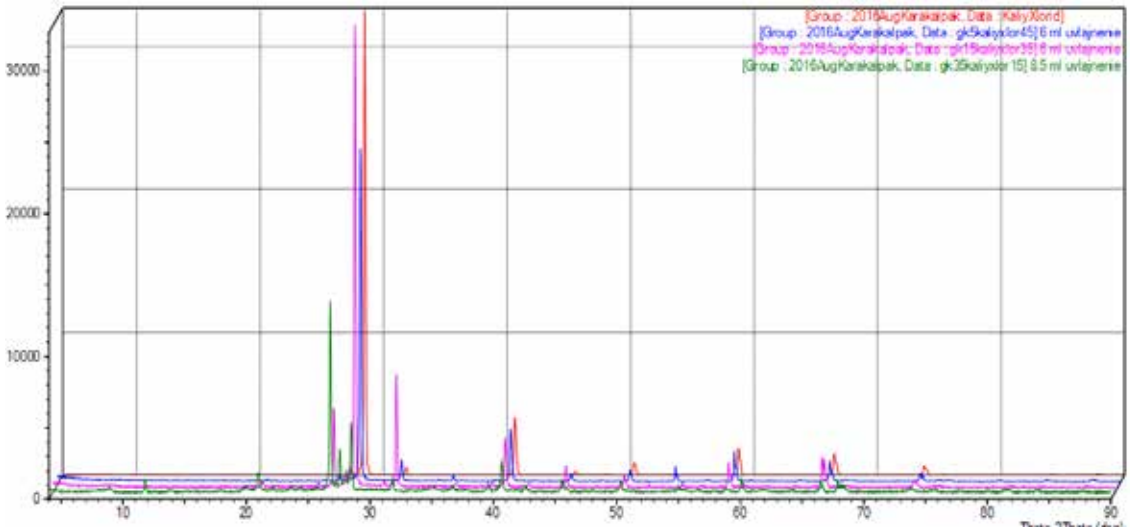

Figure 4. *Diffractograms of glauconite: carbamide mixtures in different ratios of: 1) carbamide; 2) 5:45; 3) 15:35; 4) 45:5*

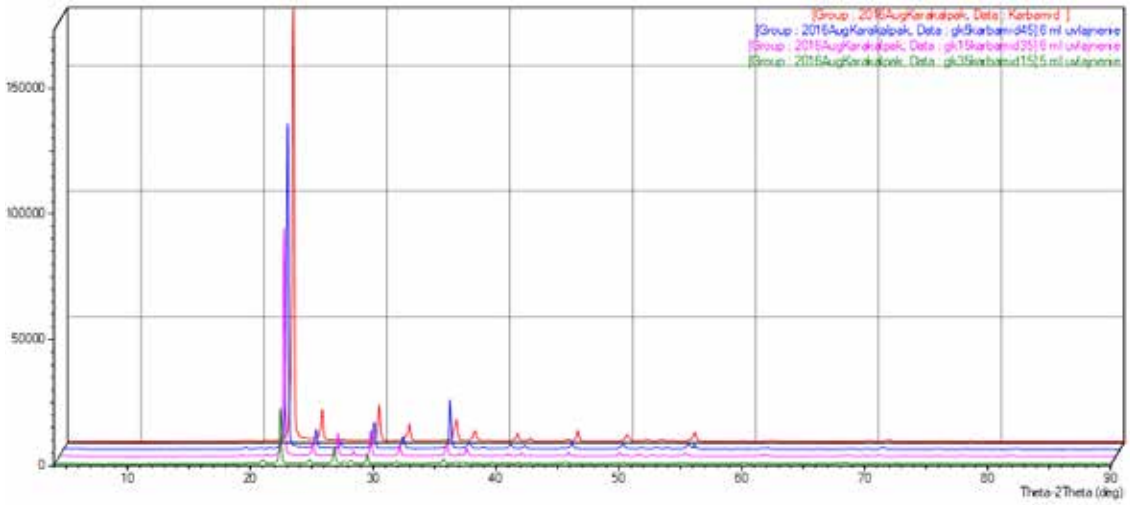

Figure 5. *Diffractograms of glauconite mixtures: ammophos in different ratios: 1) ammophos; 2) 5:45; 3) 15:35; 4) 45:5*

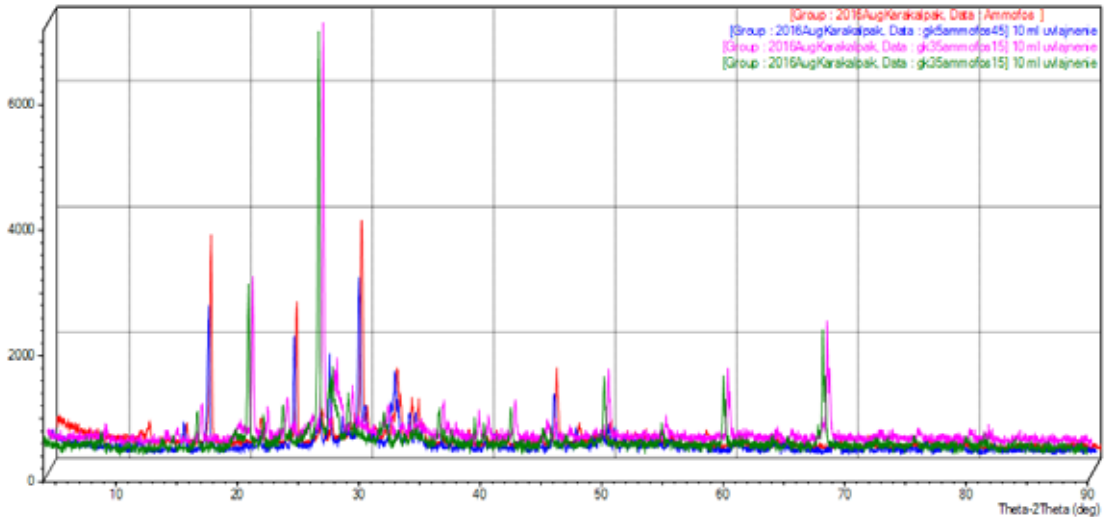

Figure 6. *Diffractograms of glauconite mixtures: phosphorite flour in different ratios: 1) phosphorite flour; 2) 5:45; 3) 15:35; 4) 45:5*

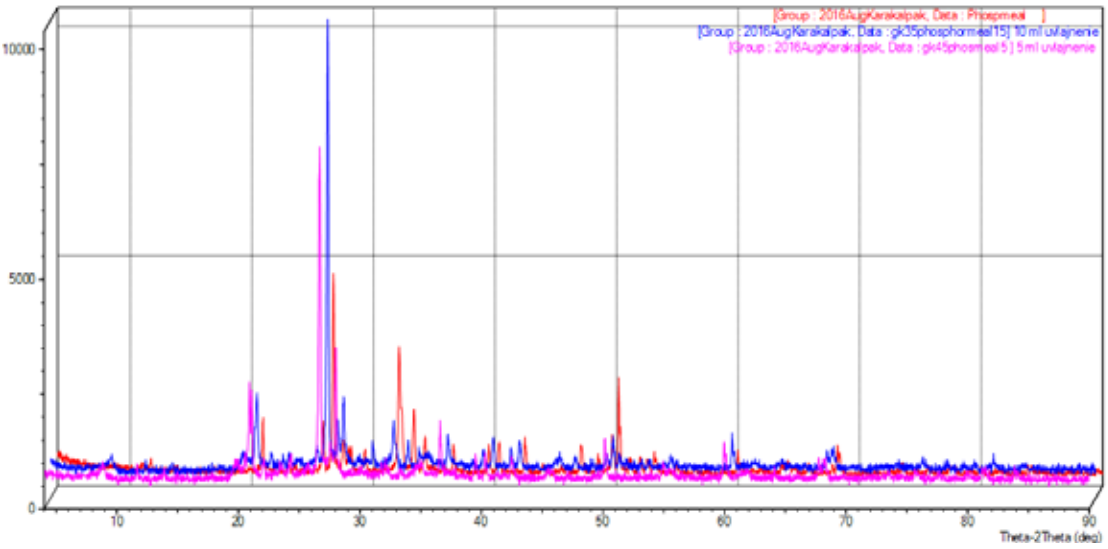

Figure 7. *Diffractograms of triple mixtures of glauconite: carbamide: phosphorite flour in different ratios: 1) phosphorite flour; 2) 15:35:50,31; 3) 15:35:21,50*

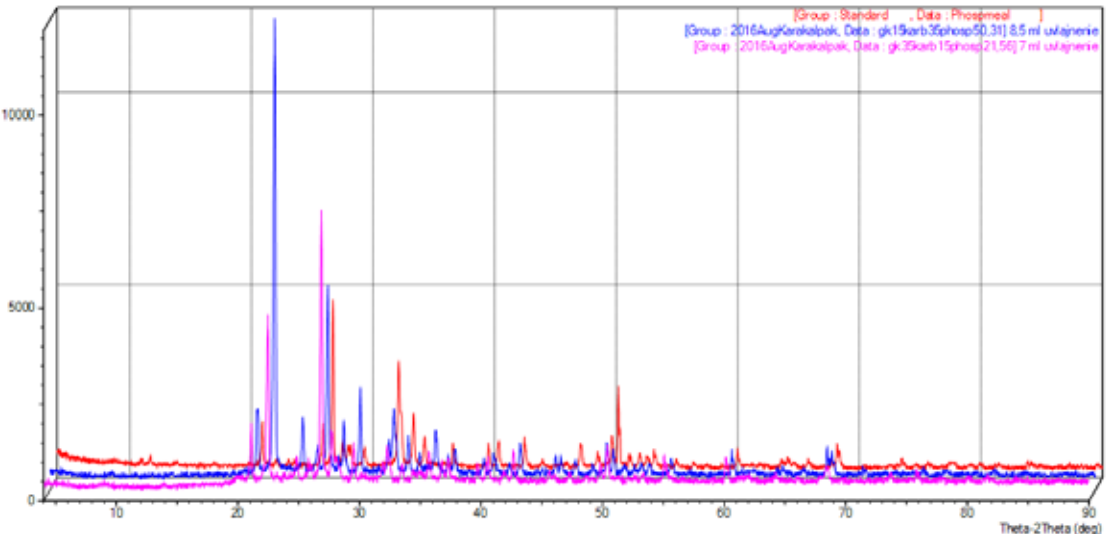

Figure 8. *Diffractograms of triple mixtures of glauconite: potassium chloride: phosphorite flour in different ratios: 1) 15:35:65; 2) 15:35:32*

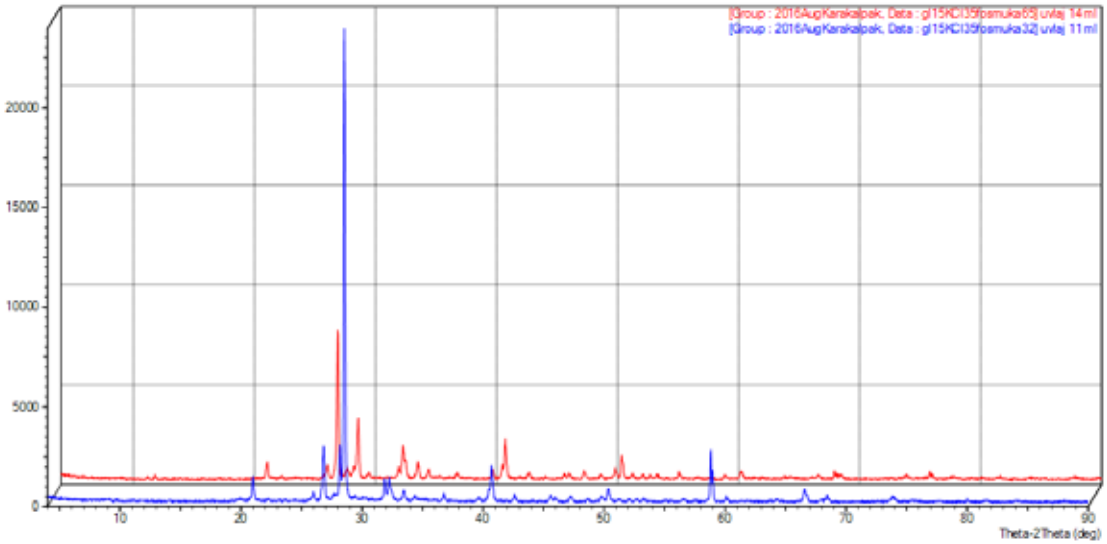

Figure 9. *Diffractograms of triple mixtures of glauconite: ammonium sulfate: phosphorite flour in different ratios: 1) 15:35: 11.5; 2) 15:35:23.*

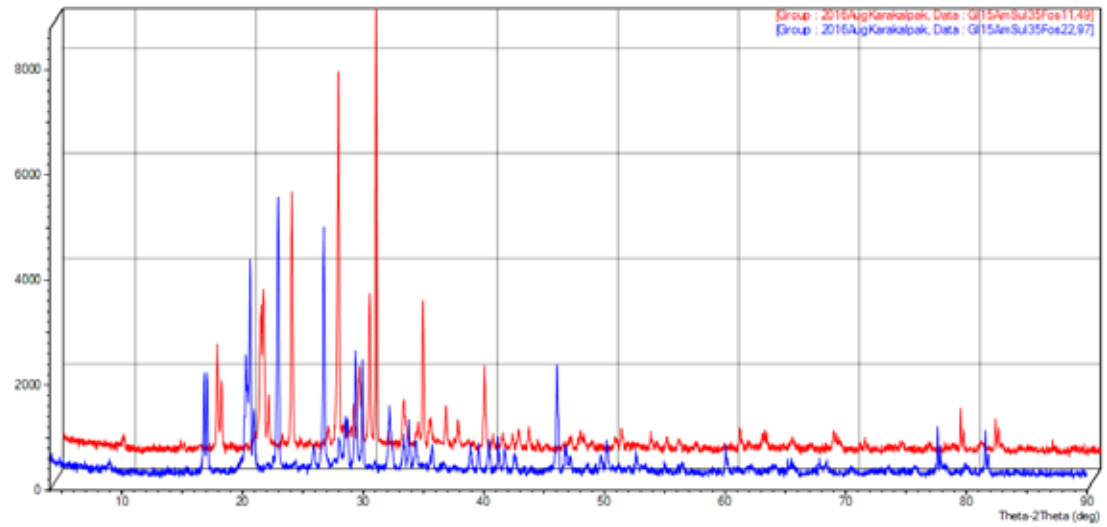

Figure 10. *Diffractograms of triple mixtures of glauconite: ammonium sulfate: phosphorite flour in different ratios: 1) 35:15:5; 2) 35:15:6;.3) 35:15:10; 2) 35:15:12.*

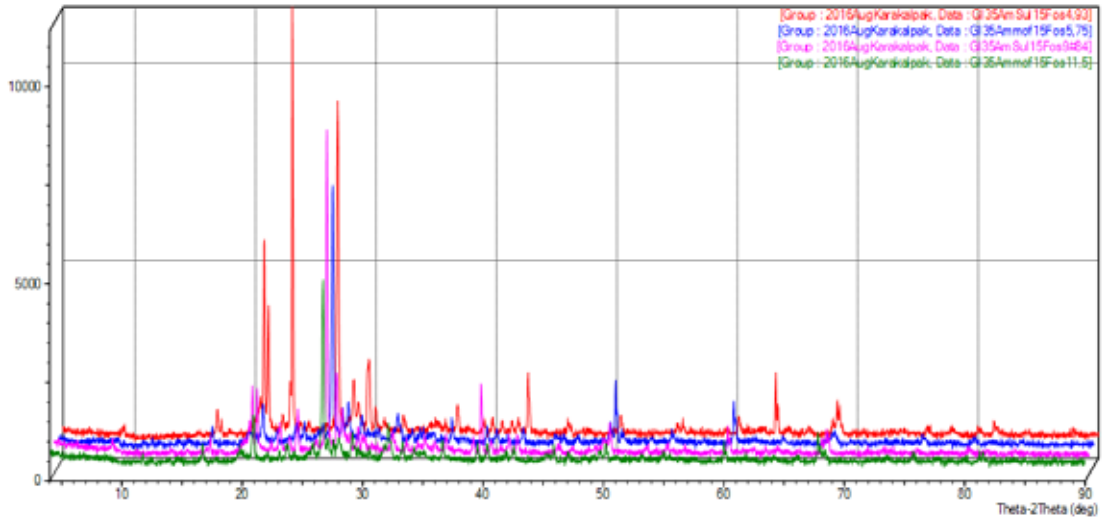

The difficulty of determining the quantitative content of glauconite in glauconite sands by the X-ray phase method, as the most operational, is that the glauconite contained in them has poor crystallinity and a large content of organic residues. It can be seen in (fig. 1) that with small amounts of glauconite sand, its peaks are weak, where the ratio of glauconite sand: ammonium nitrate, the contribution of glauconite sand peaks grows.

In glauconite sand samples: ammonium sulfate (Fig. 2), there is no direct dependence of ammonium sulfate content on the heights of the corresponding peaks in diffractograms. This trend is also observed in other samples of binary mixtures with glauconite (Fig. 3–6). Apparently, when the contribution of saltpeter, ammonium sulfate, potassium chloride, carbamide, ammophos and phosphorite flour decreases, they interact with moisture or with glauconite, and as a result, there is no direct dependence of the composition on the values of diffraction peaks. A similar pattern is observed with mixtures in which three components are present: glauconite, phosphorite flour and carbamide or potassium chloride (Fig. 7–10).

Conclusions:

Thus, during the work, it was revealed: It was found that in the prepared complex fertilizers, potassium chloride reacts with ammonium salts (ammophos, ammonium nitrate, ammonium sulfate) to form ammonium chloride and potassium salt. In turn, ammonium salts can mutually form double and triple salts. Urea remains neutral in the composition of these fertilizers. When making complex fertilizers, these interactions should be taken into account.

It has been determined that in complex fertilizers the introduced components may be crystalline or amorphous due to interaction with water, glauconite and other sand components.

References

Artyushin, A. M., Derzhavin L. M. A brief guide to fertilizers.– 2 ed.– Moscow: Kolos, 1984.–208 p.
Environmental problems of Uzbekistan. Collection of articles,– Tashkent, 2011.
Allaniyazov, D. O. Development of scientific foundations of processes for production and technology of complex fertilizers from glauconites and phosphorites of Karakalpakstan Diss. Ph D.– Tashkent. IONH AN RUz, 2019.– 123 p.
Allaniyazov, D. O., Erkaev, A. U. Enrichment of Karakalpakstan glauconite by dry method. International Scientific Journal "National Association of Scientists" (NAU). ISSN 2413–5291, 2021.– Vol. 2.– No. (36_63).– P. 4–8.
Allaniyazov, D. O., Erkayev, A. U., Tajibayev, T. A., Ochilov, S. U. Processing of local agro ores of Karakalpakstan for high-efficiency fertilizer. Journal of Survey in Fisheries Sciences – 10(3S). 2023.– P. 1225–1232.
MATCH!® Phase identification from Powder Diffraction (Crystal Impact, GbR, Bonn, Germany, 2015).
Döbelin, N., Kleeberg, R. "Profex; a graphical user interface for the Rietveld refinement program BGMN". Journal of Applied Crystallography. 2015.– № 48.– P. 1573–1580.
Drits, V. A., Zviagina, B. B., Mc Carty, D. K., Salyn, A. L. American Mineralogist, 2010.– 95,– 348 p.

submitted 22.08.2023;
accepted for publication 20.09.2023;
published 8.10.2023

Contact: dauran_1985@mail.ru

The Austrian Journal of Technical and Natural Sciences, No 9–10
ISSN 2310-5607

PREMIER Publishing
ppublishing.org

DOI:10.29013/AJT-23-9.10-67-70

STUDY OF OIL SLUDGE OF OIL REFINERY AND THEIR PROCESSING

Kobilov Nodirbek Sobirovich [1], Khamidov Bosit Nabievich [1], Shukurov Abror Sharipovich [1], Kodirov Sarvar Azamatovich [1], Sharifov Gulom [1], Shukhratov Jahongir [1]

[1] Institute of General and Inorganic Chemistry of the Academy of Sciences of the Republic of Uzbekistan, Tashkent, Uzbekistan

Cite: *Kobilov N.S., Khamidov B.N., Shukurov A.S., Kodirov S.A., Sharifov G., Shukhratov J. (2023). Study of Oil Sludge of Oil Refinery and Their Processing. Austrian Journal of Technical and Natural Sciences 2023, No 9-10.* https://doi.org/10.29013/AJT-23-9.10-67-70

Abstract

The article presents the main physical and chemical properties oil refinery production wastes, current state of them and oil sludge, types and compositions. Therefore, oil sludge formations and their compositions have been investigated. Methods of analyses and testing of oil sludge have been studied. So, physical and chemical properties of oil sludge and importance of their disposal have been shown.

Keywords: *oil, sludge, processing, composition, hydrocarbon, property, reservoir*

Introduction

Oil and gas refinery industry play main role in economy of Uzbekistan. One of them is the Bukhara Oil Refinery LLC, in 2020 produced 843,900 tons of motor gasoline, the amount of which became the highest rate in the plant's 23-year history, reports referring to the press service of Uzbekneftegaz JSC. Second is Ferghana Oil Refinery LLC is one of the largest enterprises in the Central Asian region for the processing of hydrocarbons and the production of oil products. To become a highly efficient and competitive company that takes a leading role in the oil and gas sector of the Republic of Uzbekistan is one of the most important goals of the enterprise. At the end of 2020, despite the almost complete lack of supply of the planned amount of gas condensate (light hydrocarbon raw materials), the enterprise was able to efficiently load production facilities and produce oil products necessary for the national economy and economy of the republic. Thanks to the well-coordinated work of the company's team, the refining of crude oil in absolute terms increased to the level of 900 thousand tons of oil compared to 878 thousand of crude oil in 2019. At the same time, even in the conditions of processing heavier crude oil, the refining depth indicator in 2020 remained at the level of last year's values of 87%, and the total level of fuel consumed and irrecoverable losses decreased by 2.5% compared to last year's figure (Uz Daily, 2020).

As a result of such processes, resinous compounds are formed, as well as water-oil

emulsions and mineral dispersions. Since any sludge is formed as a result of interaction with a specific environment and for a certain period of time, there are no sludges that are identical in composition and physicochemical characteristics in nature. The production activity of oil refining and oil and gas producing enterprises inevitably has a technogenic impact on natural environment objects, therefore the issues of environmental protection and rational use of natural resources are of great importance. Oil sludge is one of the most dangerous pollutants of almost all components of the natural environment, surface and ground waters, soil and vegetation cover, atmospheric air (Aliyev G. S., 2023).

Materials and methods

In the production and exploration of petroleum, wastes are generated which includes drilling fluid, petroleum wastewater, petroleum effluent treatment plant sludge and bottom tank sludge. A petroleum refinery with a production capability of 105.000 drums per day make approximately 50 tons of oily sludge per year (Sun Yuxiao, 2021). The remains found at the base of tank and other storage facilities are generally refered to as sludge. For crude oil storage vessels, this kind of sludge found at its base comprises of hydrocarbons, asphaltenes, paraffin, water, and inorganic solids such as sand, iron sulfides and iron oxides. Hydrocarbon is the principal component of petroleum sludge, which is formed when crude oil's properties are changed as a result of changes in external conditions. The formation of petroleum sludge are commonly caused by cooling below the cloud point, evaporation of light ends, mixing with incompatible materials, and the introduction of water to form emulsions. According to Resources Conservation and Recovery Act (RCRA) sludge is separated as a hazardous waste, alongside other hazardous wastes (Li G., 2013). The elemental composition of petroleum sludge is Nitrogen, Phosphorous, Potassium, Iron, Copper, Calcium, Magnesium, Cadmium, Phosphate, Chromium, Zinc, Sodium, and Lead (Gao G., 2021). With a variety of oil wastes (in a generalized form), oil sludge can be divided into four groups according to the conditions for their formation:

– Natural. Natural oil sludge is a substance that appears after oil settles to the bottom of any reservoirs and mixes it with mule and water.

– Ground. Ground oil sludge appears after the spill of oil on the ground.

– Reservoir. During storage, oil enters into a chemical reaction with the surface of the tank, thereby creating oil sludge, which is called tank sludge.

Methods for determining the total content of mechanical impurities are based on the ability of all organic components of oil to dissolve in organic solvents. The undissolved residue retained by the filter during filtration of an oil or oil product solution characterizes the content of mechanical impurities in them.

Several methods of processing oil sludge have been used with the aim of reducing toxicity, minimizing the volume of oil sludge and extracting petroleum products. Flotation, pyrolysis, combustion, biodegradation, freezing/thawing, ultrasonic treatment, electrical processing, microwave radiation and solvent extraction are among them.

Results and discussion

At consideration of the problem of residual oil waste, it is necessary to study sources of their formation, methods of utilization and processing.

Oil sludge from oil reservoirs is formed during the separation of oil and settling to the bottom of the oil sediment reservoir. Oil sludge tanks has a pasty state of aggregation. Composition and characteristics of oil deposits depend on the properties of oil.

In Uzbekistan Oil and gas refinery plant oil sludge from fuel oil tanks is formed during the storage of fuel oil. By method of production, straight-run and destructive fuel oils are distinguished origin. Oil sludge generated during storage of straight-run fuel oil has a pasty state of aggregation. Oil sludge from treatment facilities is formed in the process of water purification from oil, oil products and mechanical impurities. These oil sludge have pasty state of aggregation and black color. Oil and oil products in contaminated water are in the form of oil floating on the surface films, emulsified oil products, settled on the bottom of heavy fractions. In the process of water purification, the oil product, together

with oil sludge, enters the metal tanks, where separation occurs at a temperature of 60––70 °C mixtures under the influence of gravity on the oil product, water and oil sludge.

According to the results of studies of many varieties of oil sludge tank type, it was found that the ratio of oil products, water in them and mechanical impurities (particles of sand, clay, rust, etc.) fluctuates over a very wide range. Hydrocarbons make up 50–90%, water 10–52% and solid impurities 28–65%. As a result, such a significant change composition of oil sludge, also determine the range of changes in their physical chemical characteristics that are very broad.

The group hydrocarbon composition of oil sludge plays an important role in their oxidation with oxygen and affects the quality of the final product for obtaining a composition having the binding property of a petroleum binder. In fig from 5 to 8 were shown the group hydrocarbon composition of oil sludge.

In order to clean oil sludge from water and bring it to a homogeneous state, their elemental and aggressive-mechanical composition was determined (Table 1).

Table 1.

Type of oil sludge	Elemental composition				Mercaptan content.%	Mech. impurities.%
	C	H	O	N		
Ground	78.0	6.9	3.5	2.7	5.5	5.0–8.0
Natural	82.0	7.2	2.0	1.2	4.0	3.5–4.0
Reservoir	85.6	8.4	1.0	0.4	0.3–0.5	0.5–0.7
Field	88.9	8.6	0.4	0.2	0.1–0.2	0.3–0.4

Densities of oil sludge range from 930––1300 kg/m^3, and pour point from –3 °C to +80 °C. The flash point lies in the range from 35 to 120 °C. When water gets into the volume of oil products stable water-oil emulsions are formed, stabilization of which are due to contained in petroleum products natural stabilizers from a number of asphaltenes, resins and paraffins. Upper oil sludge layer is a watered oil product containing up to 5% fine impurities and belonging to the class emulsions “water in oil”. The composition of this layer includes 70–80% oil, 6–25% asphaltenes, 7–20% resins, 1–4% paraffins. The water content does not exceed 5–8%. Quite often, the organic part of the freshly formed top layer oil sludge is similar in composition and properties to those stored in tanks original oil product. This situation usually occurs in consumables tanks of gas stations. Proposed technologies for processing crude oil and oil wasteusing non-standard physical, chemical, and physical influences on them. In this case, the raw material is pretreated using acoustic energy, ultrasound, high-frequency(HF) and ultrahigh frequency (UHF) electromagnetic fields, ionizing radiation, exposure to plasma-chemical and electric were used.

Conclusion

In general, on the basis of investigations and experiment results the oil sludge volume and their compositions is important to develop and obtain new materials based on them for variety industry especially for energy supply sector. As the dependency on petroleum products is increasing, which in turn unavoidably lead to increase in the generation of petroleum sludge, it will be indispensable to increase the measures by which the generators to be obliged to treat the sludge without violating the environment and health safety.

References

Uz Daily. Ferghana Oil Refinery sums up the results of the outgoing 2020. URL: http://www.uzdaily.uz

Aliyev, G. S. Analysis of Physico-Chemical Methods for Investigation of Oil Sludge. Journal of Survey in Fisheries Sciences 2023; 10(2S); 826–830.

Johnson O., Affam A. Petroleum sludge treatment and disposal: A review. Environmental Engineering Research.– 24 (2), 2019. Doi: https://doi.org/10.4491/eer.2018.134
Sun Yuxiao., Yi Liu. Physical pretreatment of petroleum refinery wastewater instead of chemicals addition for collaborative removal of oil and suspended solids. Journal of Cleaner Production., Elsevier.– Vol. 278. 2021.– P 12–38.
Gao, G., Yu, T., Liu, T., Sun, X., Chong, F., Zhangx, Qu, C. Research progress on hydrothermal oxidationtechnology to treat oily sludge. IOP Conf. Series: Earthand Environmental Science.– 804, 2021. Doi:10.1088/1755–1315/804/4/04200
Li, J., Song, X., Hu, G. Ultrasonic desorptionof petroleum hydrocarbons from crude oil contaminatedsoils. J. Environ. Sci. Health A.– 8, 2013.– 11 p.

submitted 22.08.2023;
accepted for publication 20.09.2023;
published 8.10.2023

Contact: king08@mail.ru, nodirbekdoc2020@gmail.com

Contents

Section 5. Technical Science in general